

Cosmology with the Lyman-Alpha Forest

Adam Lidz

Submitted in partial fulfillment of the
requirements for the degree
of Doctor of Philosophy
in the Graduate School of Arts and Sciences

COLUMBIA UNIVERSITY

2004

INFORMATION TO USERS

The quality of this reproduction is dependent upon the quality of the copy submitted. Broken or indistinct print, colored or poor quality illustrations and photographs, print bleed-through, substandard margins, and improper alignment can adversely affect reproduction.

In the unlikely event that the author did not send a complete manuscript and there are missing pages, these will be noted. Also, if unauthorized copyright material had to be removed, a note will indicate the deletion.



UMI Microform 3138352

Copyright 2004 by ProQuest Information and Learning Company.
All rights reserved. This microform edition is protected against
unauthorized copying under Title 17, United States Code.

ProQuest Information and Learning Company
300 North Zeeb Road
P.O. Box 1346
Ann Arbor, MI 48106-1346

© 2004

Adam Lidz

All Rights Reserved

ABSTRACT

Cosmology with the Lyman-Alpha Forest

Adam Lidz

In this thesis we use the gravitational instability model of the Ly α forest to obtain constraints on cosmology. First, we constrain the neutral fraction of hydrogen at $z \sim 6$, using measurements of the mean absorption in the Ly α and Ly β forests from a $z = 6.28$ quasar discovered by the SDSS. The strongest constraint, derived from the mean Ly β transmission, is that the neutral fraction at mean density must be larger than 4.7×10^{-4} , subject to uncertainties in the normalization of the matter power spectrum. This is a factor of ~ 10 higher than the neutral fraction at $z = 4.5 - 5.7$, suggesting that dramatic changes take place around $z \sim 6$, although the constraint is still consistent with a fairly ionized IGM at $z \sim 6$. Next, we consider the cosmological utility of the Ly β forest region of a quasar spectrum. Here there is both Ly β absorption from gas at high redshift, and Ly α absorption from gas at lower redshift. Due to the wide physical separation of these absorbers, the statistics of this absorption factorizes into two separate pieces: one due to Ly α absorption, the other due to Ly β absorption. We discuss how the Ly β piece provides a better probe of the high redshift IGM and the temperature-density relation than Ly α absorption, and offers a test of the gravitational instability model of the forest. Finally, we compare the line of sight power spectrum of absorption in the Ly α forest and the cross power spectrum between the absorption in neighboring lines of sight in order to constrain dark energy. We measure the cross spectrum from a new sample of five close quasar pairs and compare with a multi-parameter grid of simulated models of the IGM. We find only weak constraints on dark energy, although an Einstein-de-Sitter cosmology is disfavored at a 2σ confidence level. We consider the power of future observations, paying particular attention to the effects of spectral resolution and shot-noise. We find that there is a sizeable gain from observing very close, $\Delta\theta \sim 30''$, separation pairs, provided that these pairs are observed with high spectral resolution.

Contents

1	Introduction	1
2	Probing Reionization with the Lyα Forest	7
2.1	Introduction	7
2.2	The Gravitational Instability Model for the IGM	10
2.3	Constraints on the Neutral Fraction	15
2.3.1	Constraints from the Ly α Mean Transmission	15
2.3.2	Constraints from the Ly β Mean Transmission	17
2.3.3	Constraints from the Gunn-Peterson Trough Itself – the Fluctuation Method	21
2.4	The Variance of the Mean Transmission	24
2.5	Discussion	29
3	The Utility of the Lyβ Forest	33
3.1	Introduction	33
3.2	Lyman- β : Probing the Equation of State of The IGM	36
3.3	Constraining the Ly β Power Spectrum	41
3.4	Discussion	47
4	Dark Energy from the Lyα Forest	51
4.1	Introduction	51
4.2	The AP Test	53

4.3	Simulation measurements of the flux power spectra	60
4.3.1	Simulation Method	61
4.3.2	Examples	64
4.4	The Flux Power Spectrum and its Redshift Distortion	67
4.5	Cross Power Spectrum Measurements	76
4.6	Observational Strategies for Future Samples	88
4.7	Conclusions	99
	Appendix A	101
	Conclusions	106
	Bibliography	113

List of Tables

List of Figures

2.1	The top panel shows the neutral fraction of hydrogen at mean density as a function of redshift implied by the measurements of the mean transmission in the Ly α forest. The point with the error bar pointing towards a completely neutral IGM comes from matching the mean transmission in Ly β . The error bars include the 1σ uncertainty in power spectrum normalization and the 1σ error in the observed mean transmission. The dotted line is offered as a guide to the eye. It shows $X_{\text{HI}} = 3.5 \times 10^{-5}(1+z/6)^3$. The bottom panel shows the corresponding evolution in the ionizing background.	16
2.2	The upper panel shows the size of the jump in neutral fraction, $X_{\text{HI}}(z=6.05)/X_{\text{HI}}(z=5.7)$, as a function of power spectrum amplitude. The amplitude is described by the value of $\Delta^2(k) \equiv 4\pi k^3 P(k)/(2\pi)^3$ at $z=2.72$ and velocity scale $k = 0.03(\text{km/s})^{-1}$. $X_{\text{HI}}(z=6.05)$ corresponds to the lower limit arising from the 1σ error in the mean transmission. The error bars come from the 1σ uncertainty in the mean transmission at $z=5.7$. The lower panel shows the neutral fraction itself at $z=6.05$. The dotted line is $X_{\text{HI}} = 5.8 \times 10^{-4}(\Delta^2(k)/0.86)^{1.1}$, demonstrating how the neutral fraction scales with amplitude.	20

- 2.3 The upper panel a shows the probability $P_\alpha \equiv \int_{ where F_i is the Ly α transmission at each pixel i of width 4 Å. Here, $N = 60$, the noise per pixel is $\sqrt{\langle n^2 \rangle} = 0.02$ and $F_m = 3\sqrt{\langle n^2 \rangle}$. The lower panel b shows an analogous probability P_β except that F_i now contains both Ly α and Ly β absorption. Here, $N = 48$, $\sqrt{\langle n^2 \rangle} = 0.02$ and 0.005 for dotted and dashed line respectively. The arrows indicate the corresponding 1 σ upper limit on J_{HI} for these different probability distributions. 25$
- 2.4 The lower panel shows the one-pixel (4 Å) probability distribution function of the true noiseless transmission $e^{-\tau}$ (i.e. $P(e^{-\tau})de^{-\tau}$ gives the probability) for 3 different values of J_{HI} : 0.004 (solid), 0.012 (dotted) and 0.028 (dashed). The upper panel shows the probability distribution function of the noisy observed transmission F for the same three values of J_{HI} . The negative values for F occur because of sky subtraction. 26
- 2.5 A prediction of the variance of the mean transmission, σ_T , (see Section 2.4) at $z \sim 6$, for several values of the ionizing background, J_{HI} . The estimate ignores contributions from photon noise. The triangles are for a model with power spectrum normalization $\Delta^2(k = 0.03 \text{ s/km}, z = 2.72) = 0.94$, the squares $\Delta^2(k = 0.03 \text{ s/km}, z = 2.72) = 0.74$, and the pentagons $\Delta^2(k = 0.03 \text{ s/km}, z = 2.72) = 0.58$ 30

3.1	A schematic diagram to show the relevant regions discussed in this chapter. The region in which only Ly α photons can be absorbed: $((1 + z_q)\lambda_{\beta}^0, (1 + z_q)\lambda_{\alpha}^0)$, where z_q is the quasar redshift, is the famous Ly α forest. The focus of this chapter is on the Lyman $\alpha + \beta$ region, $((1 + z_q)\lambda_{\gamma}^0, (1 + z_q)\lambda_{\beta}^0)$. The spectrum is of the quasar Q2139-4434, at $z_q = 3.23$, kindly provided by Arlin Crotts. Note that the rest-frame Ly α , β , γ wavelengths are: $\lambda_{\alpha}^0 = 1215.67$ Å, $\lambda_{\beta}^0 = 1025.72$ Å and $\lambda_{\gamma}^0 = 972.54$ Å. The Lyman α emission line at $\lambda = 5144$ Å is not fully shown.	34
3.2	An illustration of how Ly α and Ly β absorption probes different over-densities. <i>Left panel:</i> the differential Ly α transmission power spectra for a set of artificial temperature-density relations defined by eq. (3.5) for Δ_c ranging from 0 to 3.6 in steps of 0.4 (bottom to top, as seen around $k = 0.1$ s/km). What is shown in each case is not the absolute power spectrum, but rather the logarithmic difference from a baseline power spectrum defined by that of $\Delta_c = 0$ (this is why the line corresponding to $\Delta_c = 0$ is exactly zero). <i>Right panel:</i> the differential Ly β transmission power spectra for Δ_c ranging from 0 to 6.0 in steps of 0.4. The redshift in both panels is $z = 3.0$	39
3.3	The transmission power spectra for Ly α (upper set of 3 curves) and Ly β (lower set of 3 curves) for three models that have different equations of state. The models are chosen so that the Ly α power spectra are very similar. This is at $z = 3.74$	42
3.4	Fractional differences (squared) between the two models A and B (with the slope of the equation of state $\alpha = 0.0$ and $\alpha = 0.4$ respectively; see Fig. 3.2.) in the total and Ly α power spectra.	45

4.1	The top panel shows the squashing factor, $g_{\text{squash}}(z)$, defined in §4.2, as a function of redshift for various flat, Lambda cosmologies. The middle panel shows the same factor for open universes. The bottom panel shows the squashing factor for flat quintessence models with $\Omega_m = 0.3$. The equation of state of the quintessence field is assumed to be constant as a function of redshift. In each panel, the squashing factor is defined relative to the EDS case; it is the squashing an observer converting angles and redshifts to distances assuming an EDS cosmology would measure in a given “true” cosmology.	56
4.2	The cross spectrum for a range of flat cosmologies at $\langle z \rangle = 2.82, 2.89$, assuming a model of the IGM that provides a reasonable fit to the observed auto spectrum at each redshift. The top panel shows the cross spectrum for a separation of $\Delta\theta = 33''$ and the bottom panel shows the cross spectrum for a separation of $\Delta\theta = 62''$. These redshifts and separations correspond to those in the data set considered in §4.5.	66
4.3	Contours of constant flux power in the $k_\perp - k_\parallel$ plane. The contours range from $\ln(P/(\text{km/s})^3) = 6.5$ to $\ln(P/(\text{km/s})^3) = 12.5$. The flux power is measured from an SCDM simulation with 512^3 particles in a 20.0 Mpc/h box. The flux generation parameters are $(a, n, k_f, T_0, \langle f \rangle, \alpha) = (0.19, 0.7, 35.0 \text{ h Mpc}^{-1}, 300 \text{ (km/s)}^2, 0.684, 0.1)$	70

- 4.7 The top panel shows the cross spectrum measured from the pair Q2139-4504A/B. We also show models from our grid that are close to the best fit flat universe models with $\Omega_\Lambda = 0.9$ (top curve) and $\Omega_\Lambda = 0.0$ (bottom curve). The other IGM parameters are the same for both models, $(a, n, k_f, T_0, \langle f \rangle, \alpha) = (0.19, 0.8, 35, 200, 0.684, 0.4)$. The middle panel shows the same for the pair Q2139-4433/34. In this case, the IGM parameters are $(a, n, k_f, T_0, \langle f \rangle, \alpha) = (0.14, 0.9, 35, 250, 0.666, 0.0)$. The dashed line indicates the cut we make on the data due to the limited spectral resolution; only points to the left of the dashed line are included in our fit. The bottom panel shows the cross spectrum of a widely separated pair, which is consistent with zero. The diamonds indicate points with a positive cross spectrum and the squares indicate the absolute value of points with a negative cross spectrum.

4.8 The panels show measurements of the cross spectrum from the KP triplet pairs, as well as models from the simulation grid with $\Omega_\Lambda = 0.9$ and $\Omega_\Lambda = 0.0$ to provide some comparison between the data and model fits. The models have $(a, n, k_f, T_0, \langle f \rangle, \alpha) = (0.24, 0.9, 35, 250, 0.800, 0.6)$. The diamonds indicate points with a positive cross spectrum and the squares indicate the absolute value of points with a negative cross spectrum. In examining this figure, one should keep in mind that the measurements of the cross spectrum at a given scale are correlated across the different pairs, as discussed in the text.

- 4.9 The constraint on Ω_Λ from the quasar pairs. The dotted line shows $\Delta\chi^2 = \chi^2 - \chi_{\min}^2$ from the pair Q2139-4504A/B. The short-dashed line shows the constraint from the pair Q2139-4433 and the long-dashed line shows the constraint from the KP triplet. The dot-dashed line is the combined constraint. The solid line shows the constraint obtained ignoring Q2139-4504A/B, since the cross spectrum of this pair is somewhat poorly fit by the models in our simulation grid. 87
- 4.10 The top panel shows Croft's measured auto spectrum, interpolated to $\langle z \rangle = 2.82$ (points with error bars), a fit to this with the fitting formula of §4.6 (dashed line), and a measurement from simulations (solid line). The middle panel shows a fit to the cross spectrum at separation $\Delta\theta = 33''$ (dashed line), and the simulation measurement at the same separation (solid line). The top solid curve in the panel and its dashed fit are for a $\Omega_m = 0.3$, $\Omega_\lambda = 0.7$ (Lambda) cosmology, and the bottom curves for a $\Omega_m = 1.0$ flat (EDS) cosmology. The bottom panel is similar to the middle panel, but here we consider pairs separated by $\Delta\theta = 60''$ 92
- 4.11 The expected signal to noise level (S/N) at which one can distinguish between an $\Omega_m = 0.3$, $\Omega_\Lambda = 0.7$ cosmology and a $\Omega_m = 1.0$ cosmology from a single quasar pair as a function of resolution (FWHM). The effect of shot noise is included, with shot noise at the level of $b \sim 1.0$ km/s. We assume perfect knowledge of all of the other parameters involved in modeling the IGM. 93

4.15 A boxsize test, showing the flux auto and cross spectra for a 128^3 particle, 20.0 Mpc/h boxsize simulation and those measured from a 256^3 particle, 40.0 Mpc/h simulation of the same model. The assumed IGM model is $(a, n, k_f, T_0, \alpha, \langle f \rangle) = (0.19, 0.7, 35.0 \text{ h Mpc}^{-1}, 250 \text{ (km/s)}^2, 0.2, 0.684)$. The cross spectrum is computed assuming $\Omega_m = 1.0$, and shown at separations of $\Delta\theta = 33''$ and $\Delta\theta = 60''$. The auto spectrum shown here comes from the average of 6,000 lines of sight taken along each of the simulation box axes. The cross spectra come from the average of 3,000 pairs of lines of sight along each of the simulation box axes. The dotted lines shows the result of averaging measurements of the auto and cross spectrum over 5 independent simulation realizations of the same model using the small volume simulations. 105

Acknowledgments

I would like to thank Lam Hui for his support and guidance during the completion of this thesis. His ability to find interesting research topics, to get straight to the heart of a problem, and to ask the right questions, has been extremely valuable and a strong source of inspiration.

I benefited greatly from numerous inspirational teachers at many different levels. From high school, I would like to acknowledge an inspirational math teacher, Milan Ruzicka. From my undergraduate days, I would like to acknowledge encouragement, inspiration, and guidance from John Bohn and particularly my undergraduate research supervisor, the late Ugo Fano.

During my time at Columbia, I enjoyed conversations with many other students, particularly Liubo Borissov, Marc Carnahan, Mark Djikstra, Chad Finley, Ben Greenbaum, Sidd Joshi, Ali Kinkhabwala, Aristotle Socrates, and Jun Zhang.

I want to thank current and former members of the Fermilab Theoretical Astrophysics group for hospitality and providing a stimulating intellectual environment during my ~ 1.5 years visiting there. In particular, I am grateful to Kev Abazajian, John Beacom, Nicole Bell, Gianfranco Bertone, Scott Dodelson, Liz Duty, Josh Frieman, Rocky Kolb, Albert Stebbins, Idit Zehavi, and Pengjie Zhang.

I am grateful to the Los Alamos T-8 division for organizing several visits. I thank Salman Habib and Katrin Heitmann for their encouragement, collaboration, for lending computing facilities, and for taking me out on the town.

I want to thank collaborators for joint work on papers contained within, or in progress: Kev Abazajian, Arlin Crotts, Mark Djikstra, Scott Dodelson, Salman Habib, Katrin Heitmann, Lam Hui, Roman Scoccimarro, and Matias Zaldarriaga.

I also benefited from conversations with numerous scientists from other institutions during the completion of this thesis. In particular, I acknowledge useful conver-

sations with Kristin Burgess, Scott Burles and Nick Gnedin.

Finally I want to thank my parents and my siblings for their support. I also want to thank my fiancee, Sonja Pacho, for grammatical checks, and for her support and patience, especially during my time at Fermilab.

Chapter 1

Introduction

At redshifts of $z \gtrsim 2$, most of the baryonic matter in the universe resides in the low-density intergalactic medium (IGM), a diffuse reservoir of gas in between galaxies. Currently, our best observational tracer of the low-density IGM at moderate redshift comes from foreground neutral hydrogen gas, seen in absorption towards a background quasar. Photons emitted from the background quasar redshift as they propagate to us, and those emitted with sufficiently high energy may be absorbed by intervening neutral hydrogen when they redshift into 1215.67 Å in the frame of the intervening gas. This is the wavelength of light necessary to excite a Ly α transition in atomic hydrogen, whereby an atomic electron jumps from the ground state to the first excited state. The Ly α transition is a rest-frame ultraviolet transition, but light reaching the rest-frame Ly α wavelength at $z \gtrsim 2$ redshifts into the optical regime by the time it reaches us. As a result, optical quasar spectra, over a range of wavelengths, show a pattern of fluctuating absorption and transmission known as the Ly α forest.

A key to progress in our understanding of cosmology is to identify observable tracers of structure formation that can be measured precisely, and modeled accurately from first principles. Recent developments driven by high resolution, high signal to noise, spectral data from the Keck telescope, semi-analytic modeling, and hydrodynamic simulations may have elevated the study of the Ly α forest to this status, providing a valuable probe of cosmology (Cen et al. 1994, Zhang et al. 1995, Hern-

quist et al. 1996, Miralda-Escudé et al. 1996, Muecket et al. 1996, Bi & Davidsen 1997, Bond & Wadsley 1997, Hui, Gnedin & Zhang 1997, Croft et al. 1998, Theuns et al. 1999, Bryan et al. 1999, Nusser & Haehnelt 1999). In the emerging theoretical picture, the structure in the Ly α forest is intimately connected with the gravitational instability theory of structure formation, whereby an initial spectrum of small density perturbations grows under the influence of gravity. The physics of the absorbing gas is simple; the gas is in photoionization equilibrium with a spatially-homogeneous radiation field. On large scales the hydrogen gas distribution directly traces the dark matter distribution, while on small scales it is Jeans pressure-smoothed. The thermodynamic properties of the gas are also straightforward with the dominant processes being photoionization heating, adiabatic heating/cooling, and recombination cooling, while shock heating is unimportant. The competition between these processes then leads to a gas temperature which is a power law in the gas density for relevant densities and redshifts (Miralda-Escudé & Rees 1994, Hui & Gnedin 1997). From photoionization equilibrium, it then follows that the optical depth to Ly α absorption is also a power law in the gas density.¹

This simple physical picture, connecting the probability for Ly α absorption with gas density, implies that we can capture the relevant physics using a numerical simulation. The numerical simulation determines the matter distribution predicted by gravitational instability theory, detailing the evolution of small density fluctuations in the early universe into the filamentary, ‘cosmic web’ structure that we believe gives rise to the Ly α forest. Our approach is to construct three-dimensional simulations of the growth of structure for any desired cosmological model, and extract mock Ly α spectra from the simulation by passing lines-of-sight through the simulation box. The statistics of these mock quasar spectra can then be compared with the statistics of real quasar spectra for a variety of models, obtaining cosmological constraints by ruling out models whose mock spectra disagree with real spectra. So far, this simple

¹This statement ignores the effects of peculiar velocities and thermal broadening, which can be incorporated using a numerical simulation.

model of the Ly α forest appears to agree well with observations, reproducing the observed flux power spectrum and flux probability distribution function of Ly α forest spectra from the Keck telescope (Croft et al. 1998, 1999, 2002, McDonald et al. 2000, Zaldarriaga et al. 2001a, 2003).

Armed with this theoretical model to interpret observations, we gain insight into a range of cosmological topics. In particular, the statistics of the absorbing gas contain valuable information concerning the reionization, thermal and chemical enrichment histories of the IGM, the effects of feedback on structure formation, the small-scale linear matter power spectrum, and the contribution of dark energy to the energy density of the universe. In this thesis we touch on several of these topics, concentrating on obtaining new constraints on the reionization history of the universe and the contribution of dark energy to the energy density of the universe.

In the second chapter of this thesis, we determine the evolution of the neutral fraction of hydrogen in the IGM near $z \sim 6$ (Lidz et al. 2002, see also, e.g., Fan et al. 2002, Cen & McDonald 2002), using measurements of the mean absorption in the Ly α forest from the spectra of quasars discovered with the Sloan Digital Sky Survey (SDSS) (Fan et al. 2001a, Becker et al. 2001). In 1965, Gunn & Peterson pointed out that most of the gas in the IGM must be ionized. If, on the contrary, the IGM was mostly neutral, one would expect to find an absorption trough – long stretches of quasar spectrum with no transmitted flux – rather than the fluctuating absorption observed in a typical moderate redshift quasar spectrum. This suggests that early galaxies and/or quasars formed, photo-ionized the IGM, and left behind only trace amounts of *neutral* hydrogen. When and how this transition from a mostly neutral medium to a highly ionized medium occurred is of central importance to cosmology. This transition likely marks the formation of the first astrophysical objects, a landmark in the evolution of the universe from its simplest early stages to its present day complexity. Particularly exciting in this regard are recent spectroscopic observations of a $z = 6.28$ quasar, revealing exactly the absorption trough anticipated by Gunn & Peterson (1965). While tantalizing, the mere existence of the absorption trough does

not itself imply that the IGM was significantly neutral at redshifts higher than $z \sim 6$. In particular, the high cross section for Ly α absorption, and the large gas density at $z \sim 6$, imply that even a fairly ionized IGM can produce an absorption trough at this redshift. To quantify this, one needs a model for the clustering in the IGM. We use a numerical simulation to describe this clustering and quantify how neutral the IGM must be near $z \sim 6$ in order to match the observed absorption in the Ly α forest. Additionally, we quantify the implied *evolution* of the neutral hydrogenic fraction from $z \sim 4.5 - 6$. It is useful to characterize the evolution of the neutral fraction since many models of reionization predict a sharp decrease in the neutral fraction as the ionized regions surrounding the first ionizing sources overlap (see e.g., Gnedin 2000). We will argue that, while observations are still consistent with a fairly ionized IGM at $z \sim 6$, they suggest a rapid increase in the neutral hydrogenic fraction with increasing redshift, with the ‘jump’ in neutral fraction occurring near $z \sim 6$. This may indicate that $z \sim 6$ marks the end of the reionization process. In the conclusion of this thesis, we comment on the compatibility of this result with recent results from the Wilkinson Microwave Anisotropy Probe (WMAP) (Kogut et al. 2003), and mention other recent work.

In the third chapter, we examine the cosmological utility of the Ly β forest (Dijkstra, Lidz, & Hui 2004). The bulk of Ly α forest analyses have been confined to wavelengths where there is only Ly α absorption, and occasional absorption from metal lines. Quasar spectra with sufficient wavelength coverage, however, contain a wavelength range that might be called the ‘Ly β forest’ where there is both Ly β absorption arising from gas at high redshift and Ly α absorption from gas at lower redshift. Since the gas responsible for Ly α absorption at a given wavelength is widely separated in physical space from that responsible for Ly β absorption at the same wavelength, their absorption is essentially uncorrelated. The statistical properties of the absorption in the Ly β forest then factorizes into two separate pieces – one piece representing Ly β absorption at high redshift and the other piece representing Ly α absorption at lower redshift. The Ly β contribution, neatly separated from the Ly α contribution, offers

complementary information to the usual Ly α forest analyses. The complementarity arises since the cross section for Ly β absorption is a factor of ~ 6 smaller than that for Ly α absorption. In the second chapter, we use this fact to show that the Gunn-Peterson trough observed in the Ly β forest of the SDSS $z = 6.28$ quasar implies a tighter constraint on the neutral fraction of hydrogen than the observed trough in the Ly α forest. In the third chapter, we stress that due to its smaller cross section, Ly β absorption is sensitive to gas at higher over-densities than Ly α absorption. We emphasize that this sensitivity to a large range of over-densities allows for tighter constraints on the power law index of the temperature-density relation. This is valuable, since an improved measurement of the temperature-density relation might be useful for constraining the reionization histories of hydrogen and helium.

In the fourth chapter, we consider constraints on the dark energy contribution to the energy density of the universe, resulting from the absorption spectra of close quasar pairs (Lidz et al. 2003). As described above, a single Ly α absorption spectrum essentially provides a one-dimensional map of the density fluctuations along the line of sight to a distant quasar. The absorption spectra of adjacent lines of sight, towards background close quasar pairs, contain further, three-dimensional information. In particular, a comparison between the clustering in the Ly α forest along a line of sight with the clustering transverse to the line of sight provides a version of the classic Alcock-Paczyński test (Alcock & Paczyński 1979, McDonald & Miralda-Escudé 1999, Hui, Stebbins & Burles 1999, McDonald 2003, Lin & Norman 2002, Rollinde et al. 2003). A model that matches the observed clustering along the line of sight will only match the observed transverse clustering, measured at a given transverse separation, $\Delta\theta$, if the correct cosmology is assumed in converting from the observed $\Delta\theta$ to transverse physical size, denoted by $u_{\perp}(\Delta\theta)$ in velocity units. In this chapter of the thesis, we implement a methodology to obtain constraints on dark energy from this comparison, and apply it to a sample of 5 quasars pairs. We model redshift distortions from peculiar velocities and thermal broadening, a potential systematic difficulty in applying this test, explicitly using numerical simulations. We find only

weak constraints on dark energy, but quantify what will be necessary to do better in the future, examining the dependence of constraints on the spectral resolution and signal to noise of future data samples. This test for dark energy is valuable in that it relies on only one type of data, does not require assuming that a set of astrophysical objects are standard candles, and has a completely different set of systematics than other techniques. This provides an important cross-check on other methods.

In the concluding section, we discuss our main results and mention future research directions. We briefly address recent developments in the field, mention some work in progress, and close with our expectation that upcoming years will be exciting times for the study of the Ly α forest.

Chapter 2

Probing Reionization with the Ly α Forest

2.1 Introduction

Recent spectroscopic observations of $z \gtrsim 4.5$ quasars discovered by the SDSS have opened up new windows into the study of the high redshift IGM (Fan et al. 2000, Zheng et al. 2000, Schneider et al. 2001, Anderson et al. 2001, Fan et al. 2001a, Becker et al. 2001, Djorgovski et al. 2001). In particular, Becker et al. (2001) observed Gunn-Peterson troughs (Gunn & Peterson 1965) in the spectrum of a $z = 6.28$ quasar, which were interpreted as suggesting that the universe was close to the reionization epoch at $z \sim 6$.

That the absorption increases quickly with redshift is not by itself surprising: ionization equilibrium tells us that the neutral hydrogen density is proportional to the gas density squared, which is proportional to $(1 + z)^6$ at the cosmic mean. The evolution of the ionizing background and gas temperature will modify this redshift dependence, but the rapid evolution of absorption remains a robust outcome. What is interesting, as Becker et al. (2001) emphasized, is that the observed mean transmission at redshift $z \sim 6$ is lower than what one would expect based on an extrapolation of the column density distribution and its redshift evolution (number density of clouds scaling as

$\sim (1 + z)^{2.5}$) from lower redshifts. On the other hand, the popular gravitational instability theory of structure formation provides detailed predictions for how the IGM should be clustered, and how this clustering evolves with redshift, which has been shown to be quite successful when compared with observations at $z \sim 2 - 4$ (See e.g. Cen et al. 1994, Zhang et al. 1995, Reisenegger & Miralda-Escudé 1995, Hernquist et al. 1996, Miralda-Escudé 1996, Muecket et al. 1996, Bi & Davidsen 1997, Bond & Wadsley 1997, Hui et al. 1997, Croft et al. 1998, Theuns et al. 1999, Bryan et al. 1999, McDonald et al. 2000a). These predictions allow us to directly infer the neutral fraction of the IGM from the observed absorption (the relation between the two depends on the nature of clustering of the IGM), and so can further inform our interpretations of the recent $z \sim 6$ results.

How neutral is the IGM at $z \sim 6$, and how different is the neutral fraction compared to lower redshifts? These are the questions we would like to address quantitatively, making use of the gravitational instability model of the IGM.

This chapter is organized as follows. First, we start with a brief description of the gravitational instability model for the IGM and the simulation technique in §2.2. In §2.3.1, we derive the neutral hydrogen fraction X_{HI} , and equivalently the level of ionizing flux J_{HI} , at several different redshifts leading up to $z \sim 6$ from the observed mean Lyman-alpha (Ly α) transmission. This exercise using the Ly α spectrum is similar to the one carried out in McDonald & Miralda-Escudé (2001), except for the addition of new high redshift data.¹ We then examine in §2.3.2 the constraints on the same quantities X_{HI} and J_{HI} from the observed mean Lyman-beta (Ly β) transmission, Ly β being particularly useful at high Ly α optical depth, because the Ly β absorption cross-section is a factor of ~ 6 smaller than the Ly α cross-section. The goal here is to use Ly β absorption to obtain constraints on X_{HI} and J_{HI} that are as stringent as possible. In §2.3.2, we also examine the sensitivity of our conclusions to the power

¹This part of the calculation involving the matching of the mean Ly α transmission is also similar to a number of earlier papers where the primary quantity of interest is the baryon density (e.g. Rauch et al. 1997, Weinberg et al. 1997, Choudhury et al. 2000, Hui et al. 2001). Here, we fix the baryon density and study the ionizing background or the neutral fraction instead (see §2.2).

spectrum normalization.

An intriguing question is: instead of focusing on the mean transmission, can one make use of the fact that the observed spectrum at $z \sim 6$ contains a continuous and long stretch ($\sim 200 - 300$ Å) with little or no detected flux to obtain more stringent limits on the neutral fraction or J_{HI} ? The idea is that since the IGM gas density naturally fluctuates spatially, it seems a priori unlikely to have no significant upward fluctuation in transmission for many pixels in a row – unless of course the neutral fraction X_{HI} is indeed quite high. We will show in §2.3.3 this provides constraints that are slightly weaker to those obtained using the mean transmission.

In all the simulations discussed in this chapter, the ionizing background is assumed uniform spatially, just as in the majority of high redshift IGM simulations. A natural worry is that as the universe becomes more neutral at higher redshifts, the ionizing background would be more non-uniform. One way to test this is to use several lines of sight, available at $z \sim 5.5$, and compare the observed line-of-sight scatter in mean transmission against the predicted scatter based on simulations with a uniform background. We discuss this in §2.4, and make predictions for the scatter at $z \sim 6$. Here, we also introduce a technique to handle the problem of limited box-size.

Readers who are not interested in details can skip to §2.5 where we summarize the constraints obtained. We also discuss in §2.5 the issue of continuum placement, and how the associated uncertainties can be estimated. While the work described in this chapter was being carried out, several papers appeared which investigate related issues (Barkana 2002, Razoumov et al. 2002, Cen & McDonald 2002, Gnedin 2001, Fan et al. 2002). Where there is overlap, our results are in broad agreement with these papers. We present a comparison with other authors at the end of §2.3.2. Our approach here is most similar to that of Cen & McDonald (2002). In addition to obtaining constraints on the ionizing background from the Ly α and Ly β transmission as was considered by Cen & McDonald, we consider the possible constraint from the Gunn-Peterson trough itself, examine the dependence on power spectrum normalization, and develop a method to predict the scatter in mean transmission by relating it to the

power spectrum, which might be of wider interest. We also place a slightly stronger emphasis on the neutral fraction, which is more robustly determined compared to the ionizing background or photoionization rate.

2.2 The Gravitational Instability Model for the IGM

The Ly α optical depth is related to the IGM density, assuming photo-ionization equilibrium , via

$$\tau_\alpha = A_\alpha (1 + \delta)^{2 - 0.7(\gamma - 1)} \quad (2.1)$$

where δ is the gas overdensity ($\delta = (\rho - \bar{\rho})/\bar{\rho}$, where ρ is the gas density and $\bar{\rho}$ its mean), γ is the equation of state index for the IGM², and A_α is given by (see e.g. Hui et al. 2001 and references therein):

$$A_\alpha = 51 \left[\frac{X_{\text{HI}}}{1.6 \times 10^{-4}} \right] \left[\frac{\Omega_b h^2}{0.02} \right] \left[\frac{0.65}{h} \right] \left[\frac{1+z}{7} \right]^3 \left[\frac{11.7}{H(z)/H_0} \right] \quad (2.2)$$

where $X_{\text{HI}} \equiv n_{\text{HI}}/n_{\text{H}}$ (n_{H} is the total density of neutral and ionized hydrogen, and n_{HI} is the neutral hydrogen density) is the neutral hydrogen fraction at mean density ($\delta = 0$).³ Here $H(z)$ is the Hubble parameter at redshift z , H_0 is the Hubble parameter today, $H_0 = 100h$ km/s/Mpc, Ω_b is the baryon density in units of the critical density. The value of 11.7 for $H(z)/H_0$ above corresponds to that appropriate

²The photoionized IGM at overdensity of a few or less is expected to follow a tight temperature-density relation of the form $T = T_0(1 + \delta)^{\gamma - 1}$, where T is the gas temperature and T_0 is its value at the cosmic mean density (see Hui & Gnedin 1997). We caution that close to reionization, these quantities may not be a function of δ alone. The IGM may be heated inhomogeneously, causing spatial fluctuations in T_0 and γ .

³The neutral fraction at arbitrary δ is given by X_{HI} times $(1 + \delta)^{1 - 0.7(\gamma - 1)}$. Throughout this chapter, whenever we quote values for X_{HI} , we refer to the neutral hydrogen fraction at the cosmic mean density $\delta = 0$.

for a cosmology with $\Omega_m = 0.4$ and $\Omega_\Lambda = 0.6$ at $z = 6$, where Ω_m and Ω_Λ are the matter and vacuum densities in units of the critical density today.

The neutral fraction X_{HI} is related to the ionizing background by⁴

$$X_{\text{HI}} = 1.6 \times 10^{-4} \left[\frac{\Omega_b h^2}{0.02} \right] \left[\frac{2.55 \times 10^{-2}}{J_{\text{HI}}} \right] \left[\frac{T_0}{2 \times 10^4 \text{ K}} \right]^{-0.7} \left[\frac{1+z}{7} \right]^3 \quad (2.3)$$

where the dimensionless quantity J_{HI} is related to the photoionization rate Γ_{HI} by

$$\Gamma_{\text{HI}} = 4.3 \times 10^{-12} J_{\text{HI}} \text{ s}^{-1} \quad (2.4)$$

The quantity J_{HI} provides a convenient way of describing the normalization of the ionizing background, without specifying the exact spectrum, in a way that is directly related to the physically relevant Γ_{HI} (e.g. Miralda-Escudé et al. 1996). It is related to the specific intensity at 912 Å $j_{\nu_{\text{HI}}}$ by $J_{\text{HI}} = j_{\nu_{\text{HI}}} \times [3/(\beta+3)]$, where β is the slope of the specific intensity just blueward of 912 Å ($j_\nu \propto \nu^{-\beta}$ where ν is frequency), and $j_{\nu_{\text{HI}}}$ is measured in the customary units of $10^{-21} \text{ erg s}^{-1} \text{ cm}^{-2} \text{ Hz}^{-1} \text{ ster}^{-1}$ (for non-power law j_ν , eq. [2.4] provides the exact definition for J_{HI} ; see e.g. Hui et al. 2001).

Two more ingredients should be mentioned to complete the specification of our model for the Ly α absorption (see e.g. Hui et al. 1997 for details). First, the optical depth as a function of velocity is computed by taking the right hand side of eq. (2.1) in velocity space (i.e. taking into account peculiar velocities) and smoothing it with a thermal broadening window. Second, the gas density and velocity fields are predicted by some Cold Dark Matter (CDM) cosmological model using numerical simulations.

There are obviously a number of free parameters in our model. Let us discuss each of them in turn.

Throughout this chapter, we assume $\Omega_b h^2 = 0.02$, as supported by cosmic microwave background measurements (Netterfield et al. 2002, Pryke et al. 2002, Spergel et al. 2003) and the nucleosynthesis constraint from primordial deuterium abundance

⁴This equation assumes that hydrogen is highly ionized and that helium is largely doubly ionized. If helium is only singly ionized, the relation between J_{HI} and X_{HI} will be changed slightly: the right hand side of eq (2.3) will be multiplied by 0.93.

(Burles et al. 2001). We also assume throughout $h = 0.65$, $\Omega_m = 0.4$, and $\Omega_\Lambda = 0.6$. Variations of these parameters within the current bounds do not contribute significantly to the uncertainties of the constraints obtained in this chapter (see Hui et al. 2001).

The temperature T_0 and equation of state index γ at the redshifts of interest in this chapter are somewhat uncertain. There are no direct measurements of the thermal state of the IGM at our redshifts of interest, $z \gtrsim 4$. Measurements at $z \lesssim 4$ yield values consistent with $T_0 = 2 \times 10^4$ K and $\gamma = 1$ (McDonald et al. 2000b, Ricotti et al. 2000, Zaldarriaga et al. 2001. Schaye et al. 2000, however, measure a slightly lower temperature). Given that the temperature right after reionization is expected to be about 25000 K with $\gamma = 1$ (with some dependence on the hardness of the ionizing spectrum; see e.g. Hui & Gnedin 1997), which is not too different from the measurements at $z \lesssim 4$, we will assume throughout this chapter, when making use of eq. (2.3) to infer J_{HI} , that $T_0 = 2 \times 10^4$ K and $\gamma = 1$. Note that while the theoretically allowed range for γ is from 1 to 1.6 (Hui & Gnedin 1997), what matters for our purpose is $2 - 0.7(\gamma - 1)$ (eq. [2.1]), which only ranges from 1.58 to 2, and does not significantly affect our results. It is also important to emphasize that *the inference of X_{HI} from observations, unlike the case for J_{HI} , is not subject directly to uncertainties in the temperature T_0* . This is because observations constrain A_α from which we can obtain X_{HI} without knowing T_0 (see eq. [2.2]).⁵

To generate realizations of the density and velocity fields for a given cosmology, we run Hydro-Particle-Mesh (HPM) simulations (Gnedin & Hui 1998). The HPM algorithm is essentially a Particle-Mesh code, modified to incorporate a force term due to gas pressure in the equation of motion.⁶ For the initial power spectrum, we use

⁵The above statement is subject to two small caveats. First, the optical depth given in eq. (2.1) has to be smoothed with a thermal broadening window whose width depends on T_0 . We find that in practice, the exact width of the thermal broadening kernel does not affect very much quantities such as the mean transmission, which is what we will be interested in. Second, T_0 also affects the gas dynamics via the pressure term in the equation of motion. As we will discuss below, the effect of varying T_0 also appears to be small in this regard.

⁶The temperature-density relation has to be specified as a function of redshift in the HPM code to

a Cold Dark Matter (CDM) type transfer function, as parameterized by Ma (1996), which is very similar to the commonly used Bardeen et al. (1986) transfer function. For the primordial spectral slope, we adopt $n = 0.93$ (Croft et al. 2002, McDonald et al. 2000a). For the linear power spectrum normalization, we employ the range suggested by measurements from the Ly α forest of Croft et al. (2000): $\Delta^2(k) \equiv 4\pi k^3 P(k)/(2\pi)^3 = 0.74^{+0.20}_{-0.16}$ at $z = 2.72$ at a velocity scale of $k = 0.03(\text{km/s})^{-1}$.⁷ We, however, caution that the error-bar given is somewhat dependent on the assumed error of the mean transmission measurements, which is sensitive to the accuracy of the continuum-fitting procedure (see e.g. Zaldarriaga et al. 2001 for a slightly different assessment of the error-bar). The power spectrum in this model has a similar shape to that of favored cosmological models, but slightly lower amplitude (Croft et al. 2002). In §2.3.2 we demonstrate that our main conclusion, that the neutral fraction increases dramatically near $z \sim 6$, is insensitive to our assumptions about the amplitude of the power spectrum. In practice, we examine models with different normalizations by running a simulation with outputs at several different redshifts: each redshift then corresponds to a different power spectrum normalization, and linear interpolation is performed to reach any desired normalization.⁸

Our simulations have a box size of 8.9 Mpc/h, with a 256^3 grid. McDonald & Miralda-Escude (2001) found this box size and resolution to be adequate for IGM compute the pressure term. We follow McDonald & Miralda-Escudé (2001) and linearly interpolate between $T_0 = 19000$ K and $\gamma = 1.2$ at $z = 3.9$ and $T_0 = 25000$ K and $\gamma = 1$ at the redshift of reionization z_{reion} . We found that assuming $z_{\text{reion}} = 7$ versus $z_{\text{reion}} = 10$ results in negligible difference in our results, in particular concerning the mean decrement and the probability distribution of transmission. All results in this chapter are quoted from the $z_{\text{reion}} = 7$ HPM simulations. Note that in inferring X_{HI} and J_{HI} from eq. (2.2) and (2.3), we always use $T_0 = 20000$ K and $\gamma = 1$ for simplicity, as mentioned before.

⁷This normalization corrects an error in an earlier draft of Croft et al. (2002). (R. Croft, private communication.)

⁸We do not vary the primordial spectral index n here. Quantities such as the mean transmission which we are interested in here are generally sensitive to power on only a small range of scales. Varying n is therefore largely degenerate with varying Δ^2 .

studies up to $z \sim 5$. We have verified that the same is true up to $z = 6$, in the sense that the transmission probability distribution has converged for our choice of simulation size and resolution.

Finally, we should say a few words about simulations of the Ly β region. We will elaborate on this topic in chapter 3. In regions of the quasar spectrum that are between $973 \text{ \AA}(1 + z_{\text{em.}})$ and $1026 \text{ \AA}(1 + z_{\text{em.}})$, where $z_{\text{em.}}$ is the redshift of the quasar, two kinds of absorption can exist: one is Ly β due to material at redshift $0.948(1 + z_{\text{em.}}) < 1 + z < 1 + z_{\text{em.}}$, the other is Ly α due to material at redshift $0.800(1 + z_{\text{em.}}) < 1 + z < 0.844(1 + z_{\text{em.}})$. In other words, in such a region, the observed optical depth would be given by $\tau = \tau_\beta + \tau_\alpha$ where τ_β and τ_α arises at different redshifts. The Ly α optical depth can be computed as before. The Ly β optical depth τ_β can be computed using eq. (2.1), except that A_α is replaced by A_β ⁹:

$$A_\beta = \frac{1}{6.25} A_\alpha \quad (2.5)$$

The factor of 6.25 reflects the fact that the Ly β transition has a cross-section that is 6.25 times smaller than Ly α .

⁹In the analysis we present in this thesis, we mistakenly used a different relationship, $A_\beta = A_\alpha/5.27$, following Becker et al. (2001). The factor of 5.27 is the ratio of the *oscillator strengths*, f_α/f_β . The *correct* factor is the ratio of the cross sections, which is the ratio of *the product of the oscillator strength and the wavelength*, i.e., $(f_\alpha \lambda_\alpha)/(f_\beta \lambda_\beta)$ (Songaila 2004), which is 6.25. The same error occurs in the papers of Becker et al. (2001), Fan et al. (2002), Lidz et al. (2002), White et al. (2003), Djikstra, Lidz, & Hui (2004), and perhaps others. We will not presently examine the effect of this error, but point out that this would only *strengthen* the constraints on the neutral fraction we present below.

z	$\langle f \rangle$
4.5	0.25
5.2	0.09 ± 0.02
5.5	0.097 ± 0.002
5.7	0.070 ± 0.003
6.05	0.004 ± 0.003

Table 2.1 A summary of the observed mean transmission. The observation at redshift 4.5 is from Songaila et al. (1999). For this observation no error bars were provided by the authors. The observation at 5.2 is from Fan et al. (2000). The other observations are from Becker et al. (2001). Becker et al. (2001) have two observations at $z = 5.5$. The above mean transmission at $z = 5.5$ is the average of these two observations.

2.3 Constraints on the Neutral Hydrogen Fraction and the Ionizing Background

2.3.1 Constraints from the Ly α Mean Transmission

Using eq. (2.1) and (2.2), we compute the X_{HI} , which also fixes J_{HI} (eq. [2.3]), necessary to match the observed Ly α mean transmission $\langle e^{-\tau_\alpha} \rangle$ at $z = 4.5 - 6$ (see Table 1 for a summary of the measurements). The results of our calculation are presented in Fig. 2.1. This plot also contains a point at $z = 6.05$ which is the result of matching the mean transmission in the Ly β forest, as we describe in §2.3.2.

Also shown in the figure is a dotted line which shows $X_{\text{HI}} \propto (1 + z)^3$, which appears to be a good fit to the data from $z = 4.5$ to $z = 5.7$. From eq. (2.3), one can see that such a trend for the neutral fraction is equivalent to assuming constant J_{HI} (or more accurately, constant $J_{\text{HI}} T_0^{0.7}$; see eq. [2.3]).

As one can see, ignoring for now the Ly β point, the neutral fraction does appear to have a modest jump around $z \sim 6$: it increases by a factor of ~ 4.0 from $z = 5.7$ to $z = 6.05$, while it changes at most by ~ 1.9 from $z = 4.5$ to $z = 5.7$. A similar trend

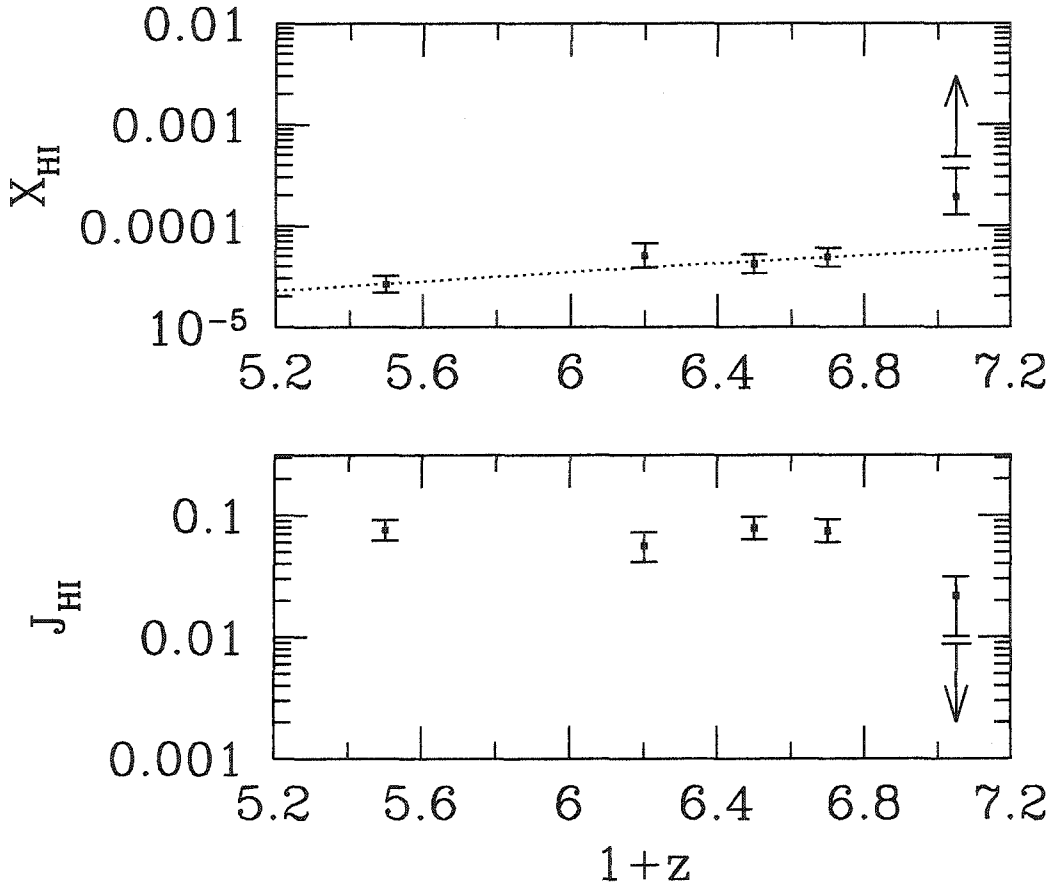


Figure 2.1 The top panel shows the neutral fraction of hydrogen at mean density as a function of redshift implied by the measurements of the mean transmission in the Ly α forest. The point with the error bar pointing towards a completely neutral IGM comes from matching the mean transmission in Ly β . The error bars include the 1σ uncertainty in power spectrum normalization and the 1σ error in the observed mean transmission. The dotted line is offered as a guide to the eye. It shows $X_{\text{HI}} = 3.5 \times 10^{-5}(1+z/6)^3$. The bottom panel shows the corresponding evolution in the ionizing background.

(but opposite in sign) can be seen in the ionizing flux J_{HI} . The 1σ error-bar here takes into account the measurement error in mean transmission, and the range of power spectrum normalization stated in §2.2. As we have explained in §2.2, while X_{HI} is not sensitive to the assumed temperature of the IGM (T_0), our constraints on J_{HI} are directly influenced by it. As emphasized before, we assume $T_0 = 2 \times 10^4$ K. In other words, our constraints on J_{HI} are really constraints on the quantity $J_{\text{HI}}(T_0/2 \times 10^4 \text{ K})^{0.7}$ (see eq. [2.3]). It is therefore straightforward to rescale our constraints on J_{HI} if the temperature were a little bit different.¹⁰ It is an interesting question to ask whether the apparent jump in the ionizing flux can instead be attributed to a jump in the temperature. In general, the temperature is expected to evolve slowly with redshift after reionization (Hui & Gnedin 1997).

Regarding the measurement error, we should also emphasize that the Becker et al.'s 2σ error actually includes the possibility of having zero transmission at $z = 6.05$. This means that at 2σ , we would only have a lower limit on X_{HI} , or an upper limit on J_{HI} , for the highest redshift point in Fig. 2.1, allowing the possibility that the IGM is neutral at $z \sim 6$, $X_{\text{HI}} = 1$.

2.3.2 Constraints from the Ly β Mean Transmission

In this section we consider the constraints placed by Becker et al.'s measurement of the mean transmission in the Ly β region. As we elaborate in chapter 3, absorption in the Ly β region has two components: $\tau = \tau_\alpha + \tau_\beta$, where the Ly α optical τ_α and the Ly β optical depth τ_β originate at different redshifts. Ly β absorption due to material at $z = 6$ coincides in wavelength with Ly α absorption due to material at $z = (1+6) \times 1026/1216 - 1 = 4.9$. Because the points of origin are so widely separated, they can be effectively treated as statistically independent i.e. $\langle e^{-\tau} \rangle = \langle e^{-\tau_\alpha} \rangle \langle e^{-\tau_\beta} \rangle$. Becker et al. measured $\langle e^{-\tau_\beta} \rangle$ at $z \sim 6$ by dividing the net mean transmission $\langle e^{-\tau} \rangle$ in the Ly β region by the mean transmission in Ly α at $z \sim 5$. They obtained

¹⁰The temperature also affects the thermal broadening window, but we find that in practice its effect on our constraints on A_α (eq. [2.2]) is small; see discussion in §2.2.

$\langle e^{-\tau_\beta} \rangle = -0.002 \pm 0.020$. Clearly, this measurement is consistent with a completely neutral IGM. However, the interesting question is: what kind of lower limit does it set on the neutral fraction, and does it improve upon the lower limit from the mean Ly α absorption?

We carry out a calculation that is analogous to what is described in §2.3.1, except for the key difference that in computing τ_β from the simulated density and velocity fields, we employ A_β which is a factor of 6.25 smaller than A_α (see eq. [2.1] & [2.5], and the caveat mentioned in the footnote attached to eq. [2.5]). The results of our calculation are shown in Fig. 2.1, as the highest redshift points in the plot, which have error bar arrows pointing towards a completely neutral IGM and a vanishing ionizing background. It can be seen that the $(1 - \sigma)$ lower limit on X_{HI} is $X_{\text{HI}} > 4.7 \times 10^{-4}$. This is a factor of ~ 3 larger than the neutral fraction required to match the upper limit on the mean transmission in Ly α for our fiducial normalization, and a slightly stronger constraint than that obtained in section 2.3.1, including the uncertainty in power spectrum normalization. Similarly, the upper limit on J_{HI} is $J_{\text{HI}} < 9.0 \times 10^{-3}$. The moral here is that because the Ly β absorption cross-section is substantially smaller than the Ly α cross-section, Ly β offers a more sensitive probe of the neutral fraction, especially when the Ly α optical depth is high.

The neutral fraction at $z \sim 6$ is thus a factor of ~ 10 higher than that at redshift $z \sim 5.7$, where it is $X_{\text{HI}} = 4.9 \times 10^{-5}$. This dramatic change in the neutral fraction is suggestive, probably indicating that the reionization epoch is nearby.

Furthermore, this conclusion is not sensitive to our assumptions about the amplitude of the power spectrum. Although the neutral fraction at redshift $z = 6.05$ is itself sensitive to the amplitude of the power spectrum, we find that the factor by which the neutral fraction increases from $z = 5.7$ to $z = 6.05$ depends only weakly on the amplitude. In Fig. 2.2 we plot both the neutral fraction at $z = 6.05$ and the jump in the neutral fraction for a range of different power spectrum normalizations. The jump is defined as the ratio $X_{\text{HI}}(z = 6.05)/X_{\text{HI}}(z = 5.7)$. Here $X_{\text{HI}}(z = 6.05)$ is the lower limit resulting from the 1σ error in the mean transmission in Ly β at $z = 6.05$ and

the error bars in the jump arise from the 1σ error in the mean transmission in Ly α at $z = 5.7$. As one can see in the plot, the lower limit on the neutral fraction at $z = 6.05$ varies from $X_{\text{HI}} > 3 \times 10^{-4}$ to $X_{\text{HI}} > 9 \times 10^{-4}$ as $\Delta^2(k = 0.03(\text{km/s})^{-1}, z = 2.72)$ varies from 0.5 to 1.3. The neutral fraction itself varies significantly with power spectrum normalization, scaling approximately as $X_{\text{HI}} \propto [\Delta^2(k = 0.03 \text{s/km}, z = 2.72)]^{1.1}$, for this range of normalizations. The jump, however, changes only slightly over a large range of normalizations. As $\Delta^2(k = 0.03(\text{km/s})^{-1}, z = 2.72)$ varies from 0.5 to 1.3, the jump changes only from ~ 9.7 to ~ 11.1 . Our conclusion that the neutral fraction of the IGM increases dramatically near $z \sim 6$ seems robust.

One can also consider the absorption in the Ly γ region, or even the higher Lyman series. In practice, the accumulated amount of absorption from Ly α as well as Ly β at different redshifts makes it harder to measure the Ly γ transmission itself with good accuracy.

Our constraints on the neutral fraction and the intensity of the ionizing background are consistent with those found by other authors, given our different choices of power spectrum normalization. Fan et al. (2002) found, from the mean Ly β transmission, that $\Gamma_{-12} < 0.025$, where Γ_{-12} is the photoionization rate of eq (2.4) in units of 10^{-12}s^{-1} . Although this constraint is somewhat stronger than the constraint implied by our fiducial model, $\Gamma_{-12} < 0.039$, we expect the difference due to our different power spectrum normalizations. Fan et al.'s (2001b) constraint comes from semi-analytic arguments, shown consistent with an LCDM simulation with $\Omega_m = 0.3$, $\Omega_\Lambda = 0.7$, $h = 0.65$, $\Omega_b h^2 = 0.02$, and $\sigma_8 = 0.9$. This model has a substantially larger normalization, $\Delta^2(k = 0.03(\text{km/s})^{-1}, z = 2.72) = 1.25$, than our fiducial model of $\Delta^2(k = 0.03(\text{km/s})^{-1}, z = 2.72) = 0.74$. The difference in normalization reflects some tension between the normalization derived from the observed cluster abundance, which Fan uses, and that from the Lyman- α forest which our model is based on (Croft et al. 2002). Fan et al. (2002) assume $T_0 = 2.0 \times 10^4$ K in placing their constraint. Their limit, $\Gamma_{-12} < 0.025$, includes only uncertainties in the mean transmission and not additional uncertainties from the power spectrum normaliza-

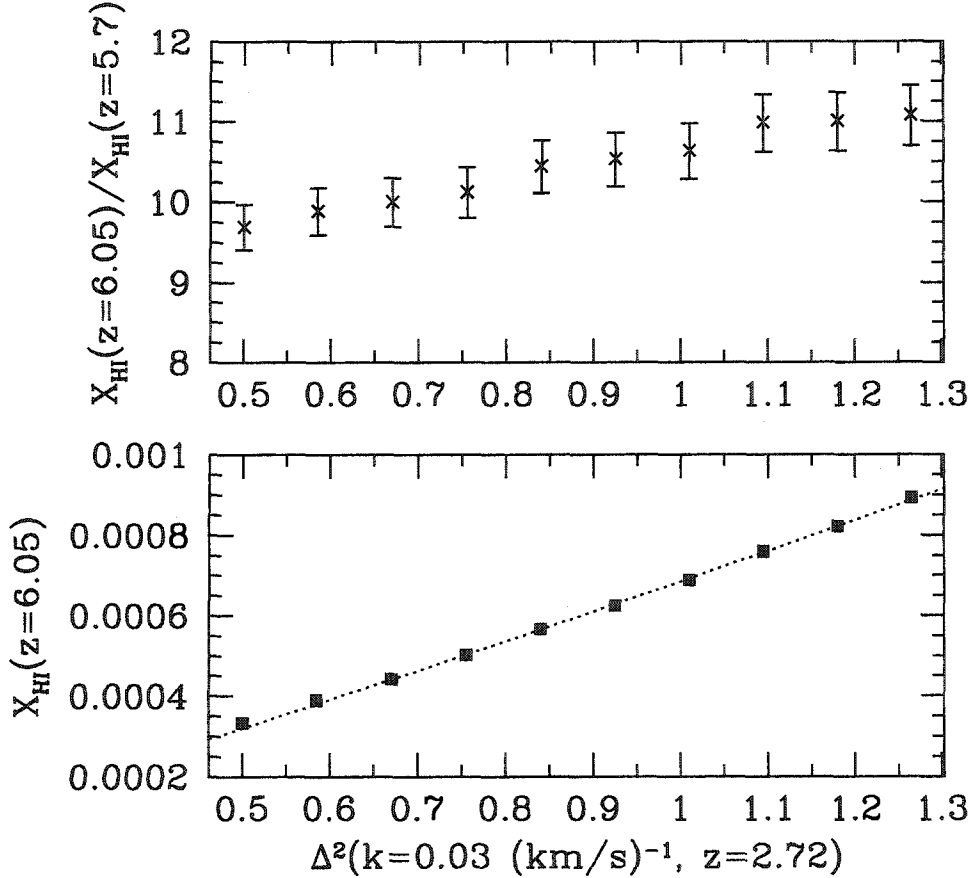


Figure 2.2 The upper panel shows the size of the jump in neutral fraction, $X_{\text{HI}}(z = 6.05)/X_{\text{HI}}(z = 5.7)$, as a function of power spectrum amplitude. The amplitude is described by the value of $\Delta^2(k) \equiv 4\pi k^3 P(k)/(2\pi)^3$ at $z = 2.72$ and velocity scale $k = 0.03(\text{ km/s})^{-1}$. $X_{\text{HI}}(z = 6.05)$ corresponds to the lower limit arising from the 1σ error in the mean transmission. The error bars come from the 1σ uncertainty in the mean transmission at $z = 5.7$. The lower panel shows the neutral fraction itself at $z = 6.05$. The dotted line is $X_{\text{HI}} = 5.8 \times 10^{-4} (\Delta^2(k)/0.86)^{1.1}$, demonstrating how the neutral fraction scales with amplitude.

tion. From figure (2.2), we infer that Fan et al.'s (2001b) normalization implies $X_{\text{HI}} > 8.8 \times 10^{-4}$ in our cosmology. Rescaling this result from our assumed $\Omega_m = 0.4$ to an $\Omega_m = 0.3$ cosmology, and using eqs. (2.3) and (2.4) we predict $\Gamma_{-12} < 0.024$, or $X_{\text{HI}} > 7.6 \times 10^{-4}$, for Fan et al.'s (2001b) model. The constraint of Fan et al. (2002) is thus consistent with our constraint given our different choice of normalization. Cen & McDonald (2002), using a model similar to that of Fan et al. (2002), obtained the constraint $\Gamma_{-12} < 0.032$, using the Ly β mean transmission. The constraint is slightly weaker than that of Fan et al. (2002) and our extrapolation to their normalization, because Cen & McDonald (2002) consider a larger upper limit to the observed mean transmission, including an estimate of the uncertainty due to sky subtraction. At slightly lower redshifts, we can also compare with the results of McDonald & Miralda-Escudé (2001) derived from matching the mean Ly α transmission. For example, at $z = 5.2$, these authors found $\Gamma_{-12} = 0.16$ to match the observed mean transmission of $\langle e^{-\tau_\beta} \rangle = 0.09$. McDonald & Miralda-Escudé (2001) consider a model whose normalization we infer to be $\Delta^2(k = 0.03(\text{km/s})^{-1}, z = 2.72) = 0.98$. To match the same mean transmission with this normalization we infer a somewhat higher photoionization rate, $\Gamma_{-12} = 0.19$. Part of the difference may be that the Γ_{-12} necessary to match a given mean transmission varies by $\sim 5\%$ between two different realizations of the density field. The remaining difference may come from the procedure of linearly interpolating between outputs or from some modeling difference. At any rate, our results are roughly consistent with those of other authors given our different power spectrum normalizations.

2.3.3 Constraints from the Gunn-Peterson Trough Itself – the Fluctuation Method

The fact that Becker et al. (2001) observed a Gunn-Peterson trough, where a long stretch of the spectrum contains little or no flux, can conceivably be used to further tighten the constraints obtained from the previous sections. Since the IGM is expected to have spatial fluctuations, the probability of having many pixels in a row turning up

a very small transmission must be low, unless the neutral fraction is intrinsically quite high. The same reasoning can be applied to either the Ly α or Ly β absorption. We will discuss our method for Ly α in detail. The method for Ly β is a straightforward extension. For simplicity, we will call this method, the fluctuation method.

Becker et al. (2001) finds from the spectrum of SDSS 1030+0524, the $z = 6.28$ quasar, the Ly α transmission is consistently below about 0.06 for a region that spans 260 Å, between 8450 Å to 8710 Å. The noise level per 4 Å pixel is $\sqrt{\langle n^2 \rangle} \sim 0.02$, where n represents the photon noise fluctuation.¹¹ The observed transmission F at a given pixel is $F = e^{-\tau} + n$, where $e^{-\tau}$ is the true transmission. The noise here should be dominated by Poisson fluctuations of the subtracted sky background (as well as perhaps read-out error). Let $P(F_1, F_2, \dots, F_N)dF_1 \cdots dF_N$ be the probability that N consecutive pixels have observed transmission fall into the range $F_1 \pm dF_1/2 \dots F_N \pm dF_N/2$. In our case, $N = 65$ for the pixel size of 4 Å. The problem is then to find the probability $\int_{<0.06} \cdots \int_{<0.06} P(F_1 \dots F_N)dF_1 \cdots dF_N$ as a function of J_{HI} , and ask what maximal J_{HI} (or equivalently, minimal X_{HI}) would give an acceptable probability. By choosing the “acceptable probability” to be within 68% of the maximum likelihood (maximum likelihood is achieved when the neutral fraction is unity), we obtain the 1 σ upper limit on J_{HI} or 1 σ lower limit on X_{HI} .

Our simulation has a comoving box size of 8.9 Mpc/h, corresponding to 42 Å for Ly α at $z \sim 6$, which falls short of the wavelength range we need for this problem, which is 260 Å. In other words, the probability $P(F_1, F_2, \dots, F_N)dF_1 \cdots dF_N$ can be estimated directly from our simulation only for $N \leq 10$. However, the mass correlation length scale at this redshift ($\lesssim 1$ Mpc/h) is actually a fraction of the box size, which means one can treat fluctuations on scales beyond the box size as roughly uncorrelated. Assuming so, we estimate $\int_{<0.06} \cdots \int_{<0.06} P(F_1, F_2, \dots, F_{10})dF_1 \cdots dF_{10}$

¹¹We estimate the noise per pixel from Becker et al.’s error-bar in the mean transmission, which is ~ 0.003 . This is estimated from a chunk of the spectrum which is 260Å long, and so the dispersion per 4 Å pixel should be approximately $\sqrt{\langle n^2 \rangle} \sim 0.003 \times \sqrt{65} \sim 0.02$. Note that the actual dispersion varies across the spectrum, but this should suffice as a rough estimate. This estimate also agrees with an estimate of the error by comparing Fig. 1 and Fig. 3 of Becker et al.

from the simulation, and then take its 6-th power, which would give us the probability that 60 consecutive pixels have transmission below 0.06. This is slightly smaller than the number 65 that we need, but at least will provide us conservative constraints on X_{HI} and J_{HI} . We have also tested our approach by using fractions of the box-size as a unit, and find that our results do not change significantly (less than 10%).

Fig. 2.3a (dotted curve) shows our estimate of the probability $\int_{<0.06} \cdots \int_{<0.06} P(F_1, F_2, \dots, F_N) dF_1 \cdots dF_N$ for $N = 60$ and pixel size 4 Å, as a function of J_{HI} . Our simulated spectra have been convolved with the observation resolution (full-width-at-half-maximum of 1.8 Å), rebinned into pixels of 4 Å each and added Gaussian noise with a dispersion of 0.02. From the dotted curve in Fig. 2.3a, applying a likelihood analysis, we obtain a 1σ upper limit on J_{HI} of $J_{\text{HI}} < 0.014$, and a corresponding lower limit on X_{HI} of $X_{\text{HI}} > 2.95 \times 10^{-4}$. This is for a model with a power spectrum normalization of $\Delta^2(k = 0.03 \text{ s/km}, z = 2.72) = 0.74$ (see §2.2). The mean Ly α transmission constraints for the same model are $J_{\text{HI}} < 0.028$ and $X_{\text{HI}} > 1.5 \times 10^{-4}$.¹² *This means that considering Ly α alone, the fluctuation method yields somewhat stronger constraints compared to using simply the mean transmission.*

Fig. 2.3b (dotted curve) shows the same methodology applied to the Ly β Gunn-Peterson trough. A new ingredient here is that one needs an additional simulation of the same model at redshift $z = 4.9$ to produce the Ly α absorption that can be overlaid on top of the Ly β absorption from $z = 6.05$. This additional simulation should have different initial phases to mimic the fact that fluctuations at $z = 4.9$ and those at $z = 6.05$ should be uncorrelated. We obtain 1σ limits of $J_{\text{HI}} < 0.012$ and $X_{\text{HI}} > 3.4 \times 10^{-4}$. This is about 40% weaker than the constraints we obtain from the Ly β mean transmission. *In other words, from Ly β absorption, the fluctuation method yields slightly weaker constraints compared to using the mean transmission.* It is also only slightly stronger than the constraint obtained from the fluctuation

¹²Do not confuse these constraints, which are for the particular power spectrum normalization mentioned above, with the constraints discussed in earlier sections, which include the uncertainty in the power spectrum normalization. We focus on a single model in this section for simplicity.

method applied to Ly α .

It is an interesting question to ask how many sightlines one would need to improve the constraints by, say a factor of 2. Our approach can be easily extended to multiple (uncorrelated) sightlines, and we find that about 5 sightlines (each containing a Gunn-Peterson trough of the same length and same signal to noise) are necessary for such an improvement.

Part of the difficulty with obtaining stronger constraints, in addition to the small number of sightlines, is the dominance of noise. The lower panel of Fig. 2.4 shows the one-pixel (4 Å) probability distribution function (PDF) of the true transmission $e^{-\tau}$ (i.e. no noise added), for three different values of J_{HI} (the power spectrum normalization is the same as that in Fig. 2.3). The upper panel shows the corresponding PDF's of the observed transmission F (i.e. after convolving $P(e^{-\tau})$ with a Gaussian of dispersion 0.02). As expected, noisy data make the PDF's more similar. Nonetheless, as we pointed out above, with sufficient number of sightlines, there might be a non-negligible chance of seeing pixels with high transmission that take place at the tail of the PDF's, hence allowing us to distinguish between the different levels of the ionizing background. Alternatively, one can try improving the signal-to-noise per pixel. In Fig. 2.3b, we show with a dashed curve the corresponding probability if the noise per pixel is lowered by a factor of 4. The constraints improve by a little more than a factor of 2. We should emphasize, however, systematic errors are likely important here – we will discuss them in the next two sections.

2.4 The Variance of the Mean Transmission

If, as is suggested by our discussion in §2.3.2 (see Fig. 2.1), the IGM is close to the epoch of reionization at $z \sim 6$, one might expect large fluctuations in the ionizing background near that time. For instance, one line of sight might probe a region of the IGM where the ionized bubbles around galaxies or quasars have percolated, while another might probe the pre-percolation IGM. As mentioned before, the simulations

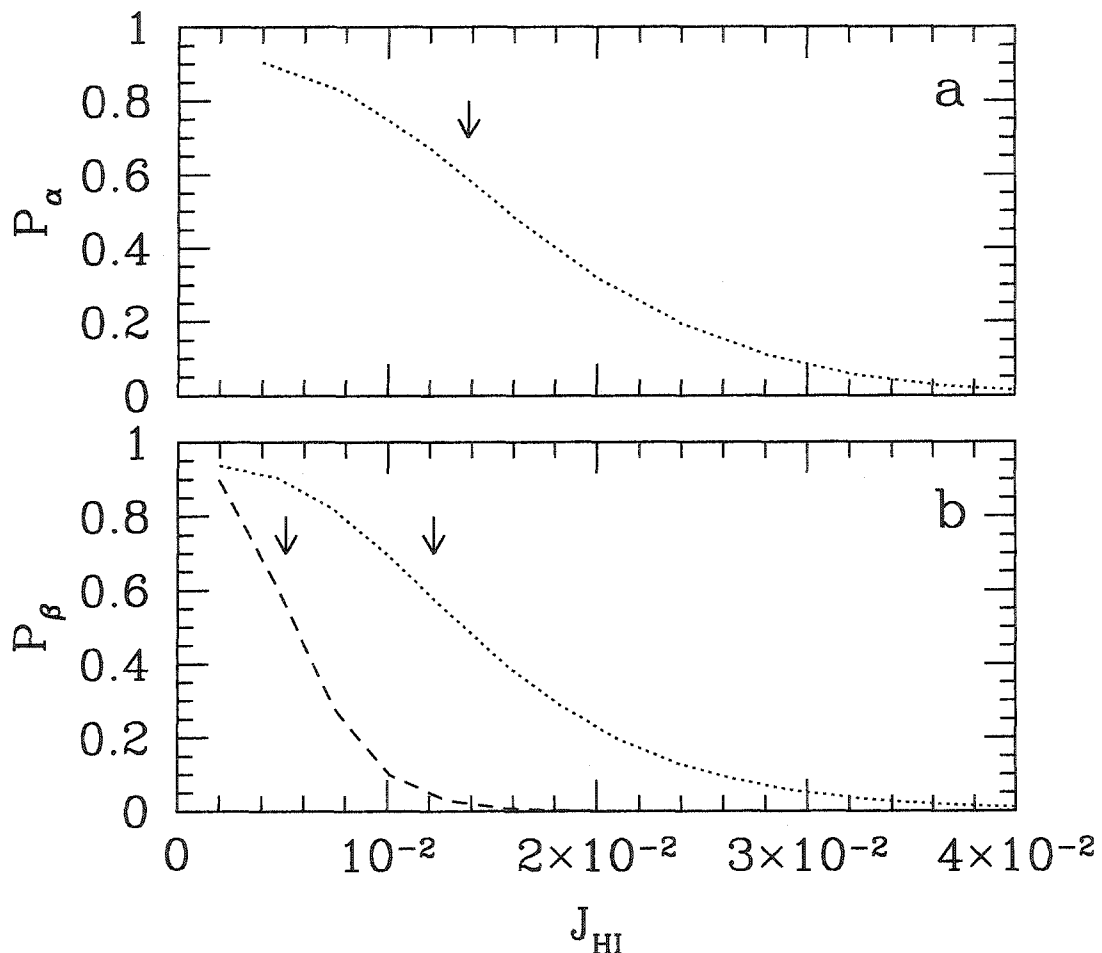


Figure 2.3 The upper panel a shows the probability $P_\alpha \equiv \int_{<F_m} P(F_1 \dots F_N) dF_1 \dots dF_N$ where F_i is the Ly α transmission at each pixel i of width 4 \AA . Here, $N = 60$, the noise per pixel is $\sqrt{\langle n^2 \rangle} = 0.02$ and $F_m = 3\sqrt{\langle n^2 \rangle}$. The lower panel b shows an analogous probability P_β except that F_i now contains both Ly α and Ly β absorption. Here, $N = 48$, $\sqrt{\langle n^2 \rangle} = 0.02$ and 0.005 for dotted and dashed line respectively. The arrows indicate the corresponding 1σ upper limit on J_{HI} for these different probability distributions.

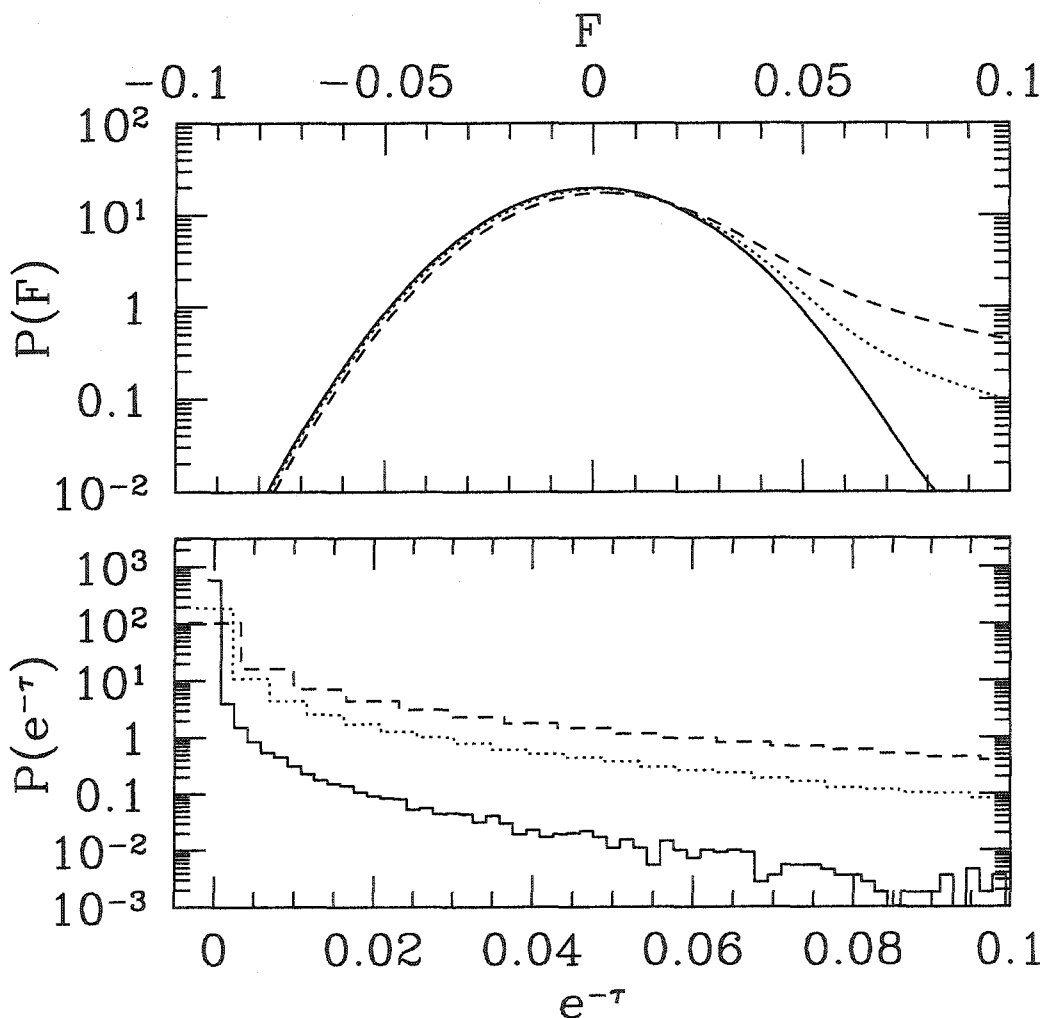


Figure 2.4 The lower panel shows the one-pixel (4 \AA) probability distribution function of the true noiseless transmission $e^{-\tau}$ (i.e. $P(e^{-\tau})de^{-\tau}$ gives the probability) for 3 different values of J_{HI} : 0.004 (solid), 0.012 (dotted) and 0.028 (dashed). The upper panel shows the probability distribution function of the noisy observed transmission F for the same three values of J_{HI} . The negative values for F occur because of sky subtraction.

we employ do not take into account fluctuations in the ionizing background. (For simulations incorporating radiative transfer see e.g., Gnedin & Abel 2001, Razoumov et al. 2002). One useful check would then be to predict the sightline to sightline scatter in mean transmission from our simulations, and compare that against the observed scatter. At $z \sim 5.5$, 4 lines of sight are available for a measurement of the scatter. We will examine this, as well as make predictions for the scatter at $z \sim 6$, which more high redshift quasars in the future will allow us to measure.

Our estimate relies on simulation measurements of the transmission power spectrum. This is in contrast to an estimate of the same quantity made by Zuo (Zuo 1993) who makes a prediction based on extrapolations of the column density distribution and of the number of absorbing clouds per. unit redshift (Zuo & Phinney 1993). Zuo also assumes that the clouds are Poisson distributed, while our measurement incorporates the clustering in the IGM via our numerical simulation.

An immediate problem presents itself: sightlines from which the mean transmission is measured are typically longer than the usual simulation box. We tackle this problem by expressing the variance of mean transmission in terms of the transmission power spectrum, and making use of a reasonable assumption about the behavior of the power spectrum on large scales.

The mean transmission from one sightline is estimated using

$$\bar{F} = \frac{1}{N} \sum_{i=1}^N F_i \quad (2.6)$$

where N is the number of pixels, F_i is the observed transmission at pixel i , $F_i = f_i + n_i$ where $f = e^{-\tau}$ is the true transmission and n is the noise fluctuation. We use the symbol \bar{F} to represent the estimator, and \bar{f} to denote the true mean transmission. The variance of the estimated mean transmission is then

$$\begin{aligned} \sigma_T^2 &\equiv \langle \bar{F}^2 \rangle - \langle \bar{F} \rangle^2 = \frac{1}{N^2} \sum_{i,j} [\langle F_i F_j \rangle - \langle F_i \rangle \langle F_j \rangle] \\ &= \frac{1}{N^2} \sum_{i,j} \xi_{ij} + \frac{1}{N} \sigma_n^2 = 2 \int_0^\infty \frac{dk}{2\pi} \left[\frac{\sin(kL/2)}{kL/2} \right]^2 P_f(k) + \frac{\sigma_n^2}{N} \end{aligned} \quad (2.7)$$

where $\sigma_n^2 \equiv \langle n^2 \rangle$ is assumed roughly independent of position, and ξ_{ij} is the unnormalized two-point correlation of the transmission i.e. $\xi_{ij} \equiv \langle f_i f_j \rangle - \bar{f}^2$, and $P_f(k)$ is its one-dimensional Fourier transform. The symbol L denotes the comoving length of the spectrum from which the mean transmission is measured, and k is the comoving wavenumber.

To evaluate σ_T , we need to know the transmission power spectrum on scales generally larger than the size of the typical simulation box. It is expected that the transmission power spectrum takes the shape (not the normalization) of the linear mass power spectrum on large scales (i.e. essentially linear biasing; see Scherrer & Weinberg 1998, Croft et al. 1997, Hui 1999). We therefore use this to extrapolate the simulation $P_f(k)$ to large scales (small k 's). We find that $P_f(k)$ is well approximated by $P_f(k) = B \exp(-ak^2) \int_k^\infty (dk/2\pi) k P_{\text{mass}}(k)$ where P_{mass} is the three-dimensional linear mass power spectrum.

Becker et al. gave an estimate of $\sigma_T \sim 0.03 \pm 0.01$, $\bar{f} = 0.1$, at $z = 5.5$ using 4 different sightlines, each spanning $\Delta z = 0.2$, which corresponds to $L \sim 57$ Mpc/h.¹³ An estimate of the noise term is provided by the error in the mean transmission, $(\sigma_n^2/N)^{0.5} \sim 0.003$. For the $\Delta^2(k = 0.03 \text{ s/km}, z = 2.72) = 0.74$ case, the fitting parameters are $B = 0.033$ and $a = 0.013 \text{ Mpc}^2/\text{h}^2$. Using eq. (2.5), we then find $\sigma_T = 0.030$ for $\Delta^2(k = 0.03 \text{ s/km}, z = 2.72) = 0.74$, $\sigma_T = 0.031$ for $\Delta^2(k = 0.03 \text{ s/km}, z = 2.72) = 0.94$, and $\sigma_T = 0.028$ for $\Delta^2(k = 0.03 \text{ s/km}, z = 2.72) = 0.58$. The variance is similar between the different normalizations because each normalization requires a different A_α in eq. (2.1) to match the mean transmission. This difference in A_α probably compensates for the effect of the different normalizations on σ_T . The predicted scatter of $\sigma_T \sim 0.030$ is consistent with the measured σ_T of 0.03 ± 0.01 .

We apply the same methodology as the above to estimate σ_T at $z \sim 6$. In Fig. 2.5, we show the results for a range of different J_{HI} 's for each of our canonical power

¹³The error on σ_T is estimated assuming Gaussian statistics and that the four lines of sight are independent. Then $\text{var}(\sigma_T) = \sigma_T^2/2n$ (see e.g. Kendall & Stuart 1958).

spectrum normalizations, $(\Delta^2(k = 0.03 \text{ s/km}, z = 2.72) = 0.58, 0.74 \text{ and } 0.94)$.¹⁴ Photon noise is not included in the estimates of this figure. Even for relatively large J_{HI} 's the scatter is small. For instance, for $J_{\text{HI}} = 4.5 \times 10^{-2}$, $\sigma_T = 1.1 \times 10^{-2}$, assuming our fiducial normalization. This J_{HI} is large in that it already gives a mean transmission, $\bar{f} = 1.75 \times 10^{-2}$, in excess of the observations. By $J_{\text{HI}} = 1.4 \times 10^{-2}$, the scatter is only $\sigma_T = 2.8 \times 10^{-3}$ for our fiducial normalization. The scatter depends somewhat on normalization, as one can see in the figure. To measure the scatter well would require data that are less noisy than the one discussed here, which has photon noise of $(\sigma_n^2/N)^{0.5} \sim 0.003$, comparable to the predicted scatter.

On the other hand, the smallness of this scatter makes it a possibly interesting diagnostic. As we have emphasized before, this predicted scatter ignores fluctuations in the ionizing background. For sufficiently small J_{HI} 's, the IGM should be close to the epoch of reionization, and one would expect large sightline by sightline variations. An observed scatter well in excess of what is predicted would be an interesting signature.

2.5 Discussion

Our findings are summarized as follows.

- The most stringent (1σ) lower limit on the neutral hydrogen fraction X_{HI} (eq. [2.3]) or upper limit on the ionizing background J_{HI} (eq. [2.4]) at $z \sim 6$ is obtained from the observed mean Ly β transmission: $X_{\text{HI}} > 4.7 \times 10^{-4}$. A comparison of this limit versus constraints at lower redshifts is presented in Fig. 2.1. The fact that the neutral fraction increases by a factor of ~ 10 from redshift of 5.7 to 6 even though it changes by no more than a factor of about 2 from $z = 4.5$ to $z = 5.7$ suggests that $z \sim 6$ might be very close to the epoch of reionization. We emphasize that current constraints are still

¹⁴The comparison across normalizations is done here at fixed J_{HI} while at $z = 5.5$ we compared the results of different normalizations at fixed mean transmission. We find that the dependence on normalization is larger at fixed J_{HI} than at fixed mean transmission.

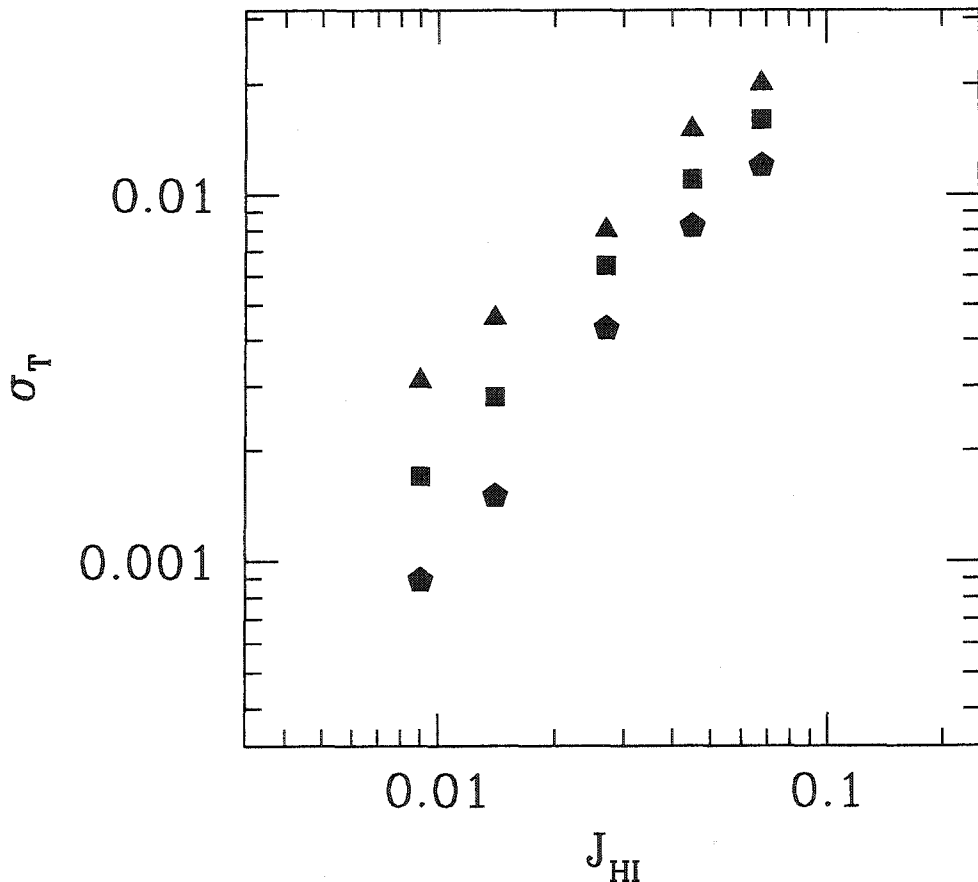


Figure 2.5 A prediction of the variance of the mean transmission, σ_T , (see Section 2.4) at $z \sim 6$, for several values of the ionizing background, J_{HI} . The estimate ignores contributions from photon noise. The triangles are for a model with power spectrum normalization $\Delta^2(k = 0.03 \text{ s/km}, z = 2.72) = 0.94$, the squares $\Delta^2(k = 0.03 \text{ s/km}, z = 2.72) = 0.74$, and the pentagons $\Delta^2(k = 0.03 \text{ s/km}, z = 2.72) = 0.58$.

consistent with a highly ionized IGM at $z \sim 6$ – it is the steep rise in X_{HI} that is suggestive of dramatic changes around or just before that redshift. We should also mention that the constraints on X_{HI} are less subject to uncertainties in the IGM temperature compared to those on J_{HI} (see §2.2).

- The existence of a long Gunn-Peterson (Ly α or Ly β) trough at $z \sim 6$, where little or no flux is detected, can also be used to obtain constraints on X_{HI} or J_{HI} . This we call the fluctuation method: the fact that a long stretch of the spectrum exhibits no large upward fluctuations in transmission provides interesting information on the neutral fraction or ionizing background. The constraints obtained this way turn out to be fairly similar to those obtained using the mean transmission. We estimate that a reduction in noise by a factor of 4, or an increase in number of sightlines to 5, would result in constraints that are 2 times stronger (§2.3.3).
- We develop a method to predict the dispersion in mean transmission measured from sightlines that are longer than the typical simulation box (eq. [2.7] and Fig. 2.5). Our predicted dispersion is consistent with that observed at $z = 5.5$ (Becker et al. 2001). We also predict the scatter at redshift $z = 6$, which can be measured when more sightlines become available. Assuming a spatially homogeneous ionizing background, we predict a small scatter at $z = 6$, $\sigma_T \sim$ a few $\times 10^{-3}$, neglecting photon noise. The dispersion provides a useful diagnostic of fluctuations in the ionizing background – close to the epoch of reionization, one expects large fluctuations from one line of sight to another depending on whether it goes through regions of the IGM where percolation of HII regions has occurred.

There are at least three issues that will be worth exploring. First, with more quasars at $z \sim 6$ or higher discovered in the future, applying some of the ideas mentioned above would be extremely interesting, such as the measurement of the line of sight scatter in mean transmission, or the use of the Gunn-Peterson trough to

obtain stronger constraints on the neutral fraction. Second, as we have commented on before, fluctuations in the ionizing background are expected to be important as we near the epoch of reionization. We have not discussed it here, but a calculation of the size of these fluctuations would be very interesting. Such a calculation will depend both on the mean free path of the ionizing photons as well as the spatial distribution of ionizing sources. The latter is probably quite uncertain, but useful estimates might be made (e.g. Razoumov et al. 2002). Lastly, a main source of systematic error which we have not discussed is the continuum placement. The mean transmissions at various redshifts given by Becker et al. are all obtained by extrapolating the continuum from the red side of Ly α by assuming a power law of $\nu^{-0.5}$. The continuum likely fluctuates from one quasar to another, and therefore, it would be very useful to apply exactly the same procedure to quasars at lower redshifts where the continuum on the blue side can be more reliably reconstructed. This will tell us how much scatter (and possibly systematic bias) the continuum placement procedure introduces to the measured mean transmission. This kind of error is especially important to quantify given the limited number of quasars available for high redshift measurements at the moment.

Chapter 3

The Utility of the Ly β Forest

3.1 Introduction

A typical high redshift quasar spectrum is shown in Fig. 3.1. Most studies of the IGM focus on the part of the spectrum where the only kind of absorption (aside from occasional absorption by metal systems) is that by neutral hydrogen via Lyman-alpha (Ly α), i.e. the well-known Ly α forest. This is the part of the spectrum that has a wavelength between $(1 + z_q)\lambda_{\beta}^0$ and $(1 + z_q)\lambda_{\alpha}^0$, where z_q is the quasar redshift. (Hereafter, we will use the symbols $\lambda_{\alpha}^0 = 1215.67 \text{ \AA}$, $\lambda_{\beta}^0 = 1025.72 \text{ \AA}$, and $\lambda_{\gamma}^0 = 972.54 \text{ \AA}$ to denote the rest-frame Ly α , Ly β and Ly γ wavelengths.) Absorption blueward of $(1 + z_q)\lambda_{\beta}^0$ is generally ignored because Ly α absorption is entangled with absorption by the higher Lyman series (for exceptions, see e.g. Press, Rybicki & Schneider 1993). For instance, absorption at a wavelength λ between $(1 + z_q)\lambda_{\gamma}^0$ and $(1 + z_q)\lambda_{\beta}^0$ has two sources:

$$e^{-\tau_{\text{tot}}(\lambda)} = e^{-\tau_{\alpha}(z_{\alpha})} e^{-\tau_{\beta}(z_{\beta})} \quad (3.1)$$

where τ_{tot} is the net total optical depth observed at the wavelength λ , and τ_{α} and τ_{β} are the Ly α and Ly β optical depths respectively, which arise from absorption by materials at two different redshifts: $z_{\alpha} = [\lambda/\lambda_{\alpha}^0] - 1$, and $z_{\beta} = [\lambda/\lambda_{\beta}^0] - 1$. We will refer to this part of the spectrum as the Ly $\alpha + \beta$ region. In §2.3.2 we used the Ly $\alpha + \beta$

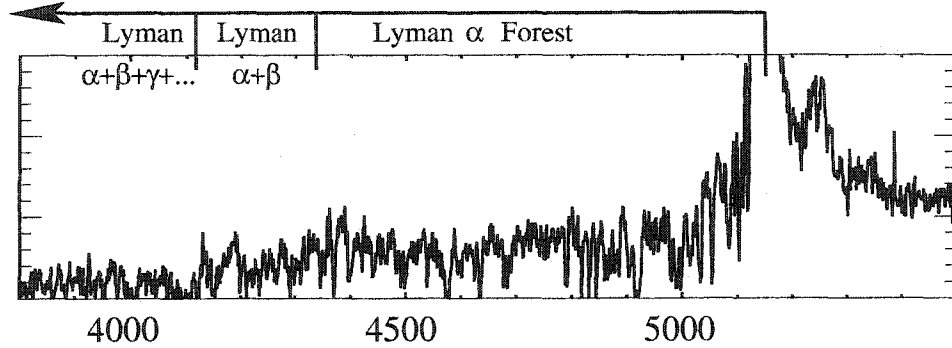


Figure 3.1 A schematic diagram to show the relevant regions discussed in this chapter. The region in which only Ly α photons can be absorbed: $((1+z_q)\lambda_{\beta}^0, (1+z_q)\lambda_{\alpha}^0)$, where z_q is the quasar redshift, is the famous Ly α forest. The focus of this chapter is on the Lyman $\alpha + \beta$ region, $((1+z_q)\lambda_{\gamma}^0, (1+z_q)\lambda_{\beta}^0)$. The spectrum is of the quasar Q2139-4434, at $z_q = 3.23$, kindly provided by Arlin Crotts. Note that the rest-frame Ly α , β , γ wavelengths are: $\lambda_{\alpha}^0 = 1215.67$ Å, $\lambda_{\beta}^0 = 1025.72$ Å and $\lambda_{\gamma}^0 = 972.54$ Å. The Lyman α emission line at $\lambda = 5144$ Å is not fully shown.

region of the $z = 6.28$ quasar spectrum of Becker et al. (2001) to constrain the neutral fraction of the $z \sim 6$ IGM. Here we consider further the cosmological utility of the Ly $\alpha + \beta$ region.

The key observation needed to understand the cosmological utility of the Ly β forest is to notice that z_{α} and z_{β} are associated with physically widely separated parts of the IGM:

$$u \sim 2c \times (\lambda_{\alpha}^0 - \lambda_{\beta}^0) / (\lambda_{\alpha}^0 + \lambda_{\beta}^0) = 5.1 \times 10^4 \text{ km/s} \quad (3.2)$$

where c is the speed of light. The velocity separation u is much larger than the correlation scale at redshifts of a few: ~ 100 km/s. This means that to good approximation, the Ly α and Ly β optical depths that contribute to the total τ_{tot} at a given

observed wavelength are uncorrelated. This implies

$$\begin{aligned}\langle e^{-\tau_{\text{tot}}(\lambda)} \rangle &= \langle e^{-\tau_\alpha(z_\alpha)} \rangle \langle e^{-\beta_\alpha(z_\beta)} \rangle, \\ \langle e^{-\tau_{\text{tot}}(\lambda^1)} e^{-\tau_{\text{tot}}(\lambda^2)} \rangle \\ &= \langle e^{-\tau_\alpha(z_\alpha^1)} e^{-\tau_\alpha(z_\alpha^2)} \rangle \langle e^{-\tau_\beta(z_\beta^1)} e^{-\tau_\beta(z_\beta^2)} \rangle,\end{aligned}\quad (3.3)$$

where $\langle \rangle$ denotes ensemble averaging (or, operationally, averaging over lines of sight), and λ^1 and λ^2 refers to two different wavelengths that reside in the Ly $\alpha + \beta$ region. The redshifts z_α^1, z_α^2 are the corresponding Ly α redshifts, and similarly, z_β^1 and z_β^2 are the corresponding Ly β redshifts.

The first equality in eq. (3.3), which states that the average transmission in the Ly $\alpha + \beta$ region factorizes into two parts, is implicitly assumed in §2.3.2 and other existing work that makes use of Ly β absorption (e.g. Cen & McDonald 2002, Fan et al. 2002, Lidz et al. 2002).

The second equality goes one step further: it tells us that the two-point correlation in the same region also factorizes into two parts: the Ly α correlation and the Ly β correlation respectively. Since both the two-point correlation in $e^{-\tau_{\text{tot}}}$ and the two-point correlation in $e^{-\tau_\alpha}$ can be measured directly (the latter from separate lines of sight to quasars at lower redshifts), eq. (3.3) tells us we have a handle on the two-point correlation in $e^{-\tau_\beta}$ as well.¹ In the present chapter, we concentrate on what can be learned from measuring the two-point correlation in $e^{-\tau_\beta}$ in addition to the usual two-point correlation in $e^{-\tau_\alpha}$.

The crucial point here is *not* to separate Ly α and Ly β absorption on an absorption-line by absorption-line basis, which is a challenging task. Rather, the strategy is to exploit the property of uncorrelated absorption to statistically separate out the two sources of absorption in the Ly $\alpha + \beta$ region of quasar spectra.

Why is the Ly β absorption interesting? As we already emphasized in §2.3.2, its utility lies in the smallness of the Ly β absorption cross-section: it is lower by a factor

¹Obviously, the same logic applies to the three-point correlation and so on, which we will not discuss here.

of 6.25 compared to the Ly α cross-section.² This means that for a given neutral hydrogen density, the associated Ly β optical depth is a factor of 6.25 lower compared to the Ly α optical depth. Therefore, Ly β absorption is more sensitive to structure at higher overdensities compared to Ly α (because Ly α goes saturated before Ly β does). As we will explain, this allows a better measurement of the equation of state of the IGM. Furthermore, by the same token, Ly β absorption also offers a better hope for constraining the large scale structure at high redshifts ($z \gtrsim 5$) where Ly α absorption is often saturated.

The organization of this chapter is as follows. In §3.2, we demonstrate how the Ly β forest is more sensitive to high overdensities than the Ly α forest, especially as far as the equation of state is concerned. In §3.3, we develop the method of statistically separating Ly β from Ly α absorption by rewriting eq. (3.3) in Fourier space. We demonstrate using a concrete example how the Ly β transmission power spectrum differentiates between different equation of states that have very similar Ly α transmission power spectra. We end in §3.4 with a discussion of **1.** how a better measurement of the equation of state might allow stronger constraints on the slope of the mass power spectrum, **2.** how the Ly β transmission power spectrum provides a more precise test of the gravitational instability model of the forest, and yields more stringent constraints on feedback processes, **3.** corrections to eq. (3.3).

3.2 The Equation of State of the IGM: Lyman- α versus Lyman- β

The photoionized IGM is well described by a temperature-density relation, or an effective equation of state, which we denote here by:

$$T = T_0 \Delta^\alpha \quad (3.4)$$

²See the footnote near eq. (2.5) in §2.2. The analysis in this chapter was actually carried out assuming this factor was 5.27, rather than 6.25. This difference should only strengthen our conclusions moderately.

where α denotes the slope of the temperature-density relation and $\Delta = \rho/\bar{\rho}$, with ρ being the gas density, and $\bar{\rho}$ its mean (i.e., $\alpha \equiv \gamma - 1$, and $\Delta \equiv 1 + \delta$ in the notation of eq. [2.1]). Such a relation appears to hold for $\Delta \lesssim 5$ (Miralda-Escude & Rees 1994, Hui & Gnedin 1997).

Current measurements from the Ly α forest in the redshift range $\sim 2.4 - 4.0$ yield much better constraints on T_0 than on α (Ricotti, Gnedin & Shull 2000, Schaye et al. 2000, Bryan & Machacek 2000, McDonald et al. 2001, Meiksin, Bryan & Machacek 2001, Zaldarriaga, Hui & Tegmark 2001 [ZHT01 hereafter]). The reason is quite simple to understand. Ly α absorption is sensitive largely to $\Delta \sim 1 - 2$, and the short lever arm does not allow a precise measurement of the slope α . Present constraints are consistent with the full physically plausible range $\alpha = 0 - 0.6$ (Hui & Gnedin 1997), according to ZHT01.³

To illustrate the range of overdensities that the Ly α forest is sensitive to, we measure the transmission power spectrum from mock Ly α spectra which are generated using N-body simulations. The simulations used throughout this chapter are 256^3 -grid, 128^3 -particle, P3M simulations of a Standard Cold-Dark-Matter model with a box size of $16 \text{ Mpc}/\text{h}$. The simulations are dark-matter only simulations generated with the HYDRA code of Couchman et al. (1995). The baryon density is obtained by smoothing the dark matter density to mimic the effect of pressure forces (See ZHT01 for more details). These simulations have lower resolution than recommended by McDonald (2003) and Meiksin & White (2004) to achieve convergence in measuring the flux power spectrum. We expect, however, that our present simulations are adequate to qualitatively illustrate the benefits of measuring the Ly β flux power spectrum.

In the left panel of Fig. 3.2 we show the Ly α transmission power spectrum at

³ZHT01 constrain α using measurements of the small scale flux power spectrum. McDonald et al. (2001), using a line-fitting method, find a tighter constraint on α at $z = 2.4$, requiring $\alpha \geq 0.38$ at a 1σ -confidence level. Schaye et al. (2000) obtain still tighter constraints using also a line-fitting method. The difference between Schaye et al. (2000)'s error bars and McDonald et al. (2001)'s error bars are due to different line selection criteria (See McDonald et al. (2001) for a discussion on this).

$z = 3.0$ for a set of artificial equations of state parameterized in the form (following ZHT01):

$$\begin{aligned} T &= T_0 \quad , \quad \text{for } \Delta < \Delta_c \\ T &= 2T_0 \quad , \quad \text{for } \Delta \geq \Delta_c \end{aligned} \quad (3.5)$$

where Δ_c defines the density threshold where the gas temperature T has a jump and $T_0 = 1.2 \times 10^4 \text{ } ^\circ K$. The left panel shows the Ly α transmission power spectrum for Δ_c varying from 0.0 to 3.2 in steps of 0.4. We have subtracted from each power spectrum a baseline power spectrum corresponding to that of $\Delta_c = 0.0$. In comparing power spectra with different Δ_c , we fix all of the other IGM modeling parameters.

The Ly α transmission (or flux) power spectrum $P_{f,\alpha}(k)$ is defined as follows:

$$\begin{aligned} \xi_{f,\alpha}(u) &= \langle \delta_{f,\alpha}(u^1) \delta_{f,\alpha}(u^1 + u) \rangle , \\ P_{f,\alpha}(k) &= \int \frac{dk}{2\pi} \xi_{f,\alpha}(u) e^{-iku} \end{aligned} \quad (3.6)$$

where $\xi_{f,\alpha}(u)$ is the two-point correlation function at a velocity separation of u , the transmission power spectrum $P_{f,\alpha}(k)$ is its Fourier counterpart as a function of wavenumber k , and $\delta_{f,\alpha}$ is the fluctuation of the Ly α transmission about its mean:

$$\delta_{f,\alpha} \equiv \frac{e^{-\tau_\alpha}}{\langle e^{-\tau_\alpha} \rangle} - 1 . \quad (3.7)$$

Note that the definition of $\xi_{f,\alpha}$ differs from the kind of two-point correlation in eq. (3.3) in that $\xi_{f,\alpha}$ involves the correlation of $\delta_{f,\alpha}$, which has zero mean, and is properly normalized. We will sometimes refer to ξ_f as the normalized two-point function.

The left panel of Fig. 3.2. shows that the Ly α transmission power spectrum at high k ($\sim 0.1 \text{ s/km}$) increases, as Δ_c increases from 0 (or, in other words, according to eq. (3.5), as the temperature drops). This is consistent with the intuition that thermal broadening acts like a smoothing, and suppresses small scale power, a fact that is used to constrain the thermal state of the IGM from observations (ZHT01). The interesting point of the left panel of Fig. 3.2. is that changes in the Ly α transmission power spectrum are most pronounced in a narrow range of Δ_c 's, from about 1 to 2. For

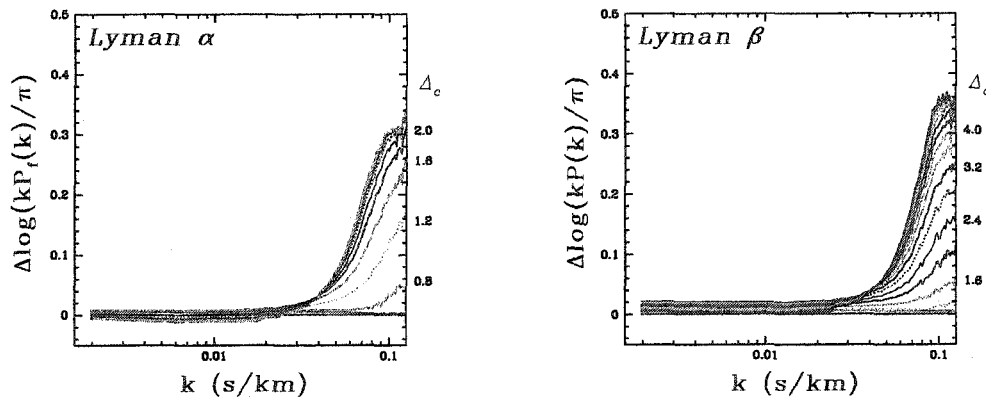


Figure 3.2 An illustration of how Ly α and Ly β absorption probes different overdensities. *Left panel:* the differential Ly α transmission power spectra for a set of artificial temperature-density relations defined by eq. (3.5) for Δ_c ranging from 0 to 3.6 in steps of 0.4 (bottom to top, as seen around $k = 0.1$ s/km). What is shown in each case is not the absolute power spectrum, but rather the logarithmic difference from a baseline power spectrum defined by that of $\Delta_c = 0$ (this is why the line corresponding to $\Delta_c = 0$ is exactly zero). *Right panel:* the differential Ly β transmission power spectra for Δ_c ranging from 0 to 6.0 in steps of 0.4. The redshift in both panels is $z = 3.0$.

smaller or larger Δ_c 's, the Ly α power spectrum does not change in a substantial way. This is fundamentally why current observations from the Ly α forest yield useful constraints on the temperature around mean density (or 1–2 times the mean density), but not on the slope of the equation of state α (eq. (3.4)). A stronger constraint can be obtained if one has the means to probe the temperature of the IGM over a larger range of densities.

The Ly β transmission power spectrum provides the requisite probe of the IGM over a large range of densities, as illustrated by the right panel of Fig. 3.2. This panel is similar to the left panel, except that it shows the Ly β transmission power spectrum rather than the Ly α power spectrum. The Ly β transmission power is defined by (similar to eq. (3.6), and (3.7)):

$$\xi_{f,\beta}(u) = \langle \delta_{f,\beta}(u^1) \delta_{f,\beta}(u^1 + u) \rangle, \quad (3.8)$$

$$P_{f,\beta}(k) = \int \frac{dk}{2\pi} \xi_{\beta}^f(u) e^{-iku},$$

$$\delta_{f,\beta} \equiv \frac{e^{-\tau_\beta}}{\langle e^{-\tau_\beta} \rangle} - 1. \quad (3.9)$$

In the right panel, we let Δ_c vary from 0.0 at the bottom to 6.0 at the top. Clearly, the Ly β transmission power spectrum is sensitive to higher densities: it continues to vary from Δ_c of 1 to about 4.⁴

Note that the experiment shown in Fig. 3.2. is done at $z = 3$. If one moves to higher redshifts, the Δ 's one is sensitive to shift to lower values for both Ly α and Ly β . This is simply because the mean density of the universe is higher, and lower overdensities give rise to the same amount of absorption as at $z = 3$. For instance, we have repeated the above experiment at $z = 3.74$, and find that the range of sensitive Δ 's shift downward by about 0.5 for both Ly α and Ly β .

⁴At sufficiently high overdensities, the equation of state given in eq. (3.4) would no longer be a good description of the temperature-density relation, because large scale shock-heating becomes important which introduces a significant scatter to the temperature. The temperature-density relation for overdensities of Δ up to ~ 5 is probably still describable by eq. (3.4) (Hui & Gnedin 1997).

Fig. 3.2. is only meant to illustrate the range of densities that Ly α and Ly β absorption are sensitive to. Does the Ly β transmission power spectrum differentiate between realistic equations of state that are otherwise difficult to disentangle using the Ly α power spectrum alone? This is addressed in Fig. 3.3. At the top of the figure, we show three different Ly α transmission power spectra, each assuming a different equation of state slope (α in eq. (3.4)). The other IGM model parameters (see ZHT01) are adjusted slightly (well within observational uncertainties)⁵ in each case to give very similar $P_{f,\alpha}(k)$'s. The Ly β transmission power spectra for these three cases show more differences at high k , suggesting that observational constraints on $P_{f,\beta}(k)$ might be useful. Our next task is to describe how to tease out $P_{f,\beta}(k)$ from the Ly $\alpha + \beta$ region of quasar spectra.

3.3 Constraining the Ly β Power Spectrum

As discussed in §3.1, the coincident Ly α and Ly β absorption in the Ly $\alpha + \beta$ region of a quasar spectrum are to a good approximation uncorrelated. This gives rise to a simple factorization of the (un-normalized) two-point function (eq. (3.3)). The normalized two-point function obeys

$$\xi_{f,\text{tot}}(u) = \xi_{f,\alpha}(u) + \xi_{f,\beta}(u) + \xi_{f,\alpha}(u)\xi_{f,\beta}(u) \quad (3.10)$$

where $\xi_{f,\text{tot}}$ as a function of velocity separation u is defined in a similar way to eq. (3.6) and (3.8) (i.e. $\xi_{f,\text{tot}}(u) \equiv \langle \delta_{f,\text{tot}}(u_1)\delta_{f,\text{tot}}(u_1+u) \rangle$, with $\delta_{f,\text{tot}} \equiv [e^{-\tau_{\text{tot}}}/\langle e^{-\tau_{\text{tot}}} \rangle] - 1$, and τ_{tot} being the total Ly $\alpha + \beta$ optical depth). The velocity separation u is related to the quantities λ^1 , λ^2 , z_α^1 , z_α^2 , z_β^1 and z_β^2 in eq. (3.3) by:

$$u = c \frac{\lambda^2 - \lambda^1}{\bar{\lambda}} = c \frac{z_\alpha^1 - z_\alpha^2}{1 + \bar{z}_\alpha} = c \frac{z_\beta^1 - z_\beta^2}{1 + \bar{z}_\beta} \quad (3.11)$$

where $\bar{\lambda}$ is the mean observed wavelength in the Ly $\alpha + \beta$ region, and $\bar{\lambda} = (1 + \bar{z}_\alpha)\lambda_\alpha^0 = (1 + \bar{z}_\beta)\lambda_\beta^0$.

⁵In the notation of ZHT01, model A/B has $(k_F, \alpha, T_0, \bar{f}) = (36, 0.0, 310, 0.512) / (39, 0.4, 305, 0.507)$. Here k_F is in units of $h \text{ Mpc}^{-1}$ and T_0 is in units of $(\text{km/s})^2$.

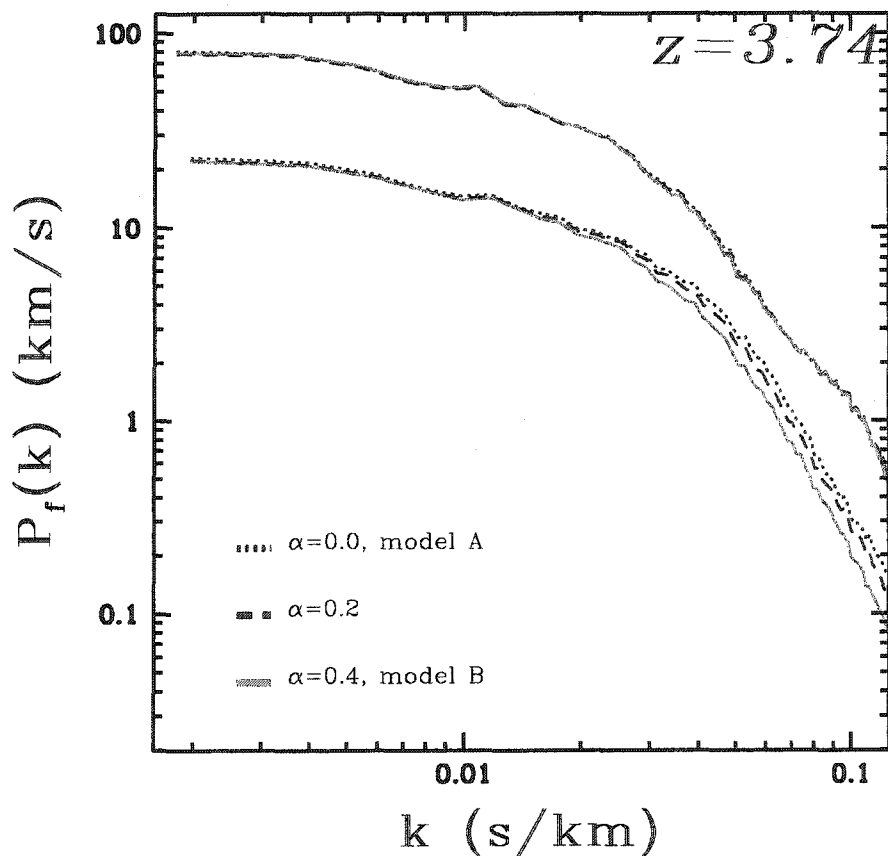


Figure 3.3 The transmission power spectra for Ly α (upper set of 3 curves) and Ly β (lower set of 3 curves) for three models that have different equations of state. The models are chosen so that the Ly α power spectra are very similar. This is at $z = 3.74$.

The Fourier counterpart of eq. (3.10) is

$$\begin{aligned} P_{f,\text{tot}}(k) &= P_{f,\alpha}(k) + P_{f,\beta}(k) \\ &+ \int \frac{dk'}{2\pi} P_{f,\alpha}(k - k') P_{f,\beta}(k') \end{aligned} \quad (3.12)$$

where $P_{f,\text{tot}}$ is the power spectrum of the total transmission in the Ly $\alpha + \beta$ region. We will often refer to $P_{f,\text{tot}}$ as the total power. Note that implicit in the above expression is that $P_{f,\alpha}$ and $P_{f,\beta}$ are at different mean redshifts: $\bar{z}_\alpha, \bar{z}_\beta$.

One can directly measure both $P_{f,\text{tot}}$ and $P_{f,\alpha}$ from observational data. To constrain the Ly β power spectrum $P_{f,\beta}$, it is important that quasars at different redshifts are employed to measure $P_{f,\text{tot}}$ and $P_{f,\alpha}$ – the former from higher redshift quasars, and the latter from lower redshift quasars whose Ly α -only region overlaps in wavelengths with the Ly $\alpha + \beta$ region of the former.

In principle, once $P_{f,\text{tot}}$ and $P_{f,\alpha}$ are given, eq. (3.12) can be inverted to obtain $P_{f,\beta}$ if one thinks of it as a linear vector equation:

$$\mathbf{P}_{f,\text{tot}} - \mathbf{P}_{f,\alpha} = \mathbf{M} \cdot \mathbf{P}_{f,\beta} \quad (3.13)$$

where \mathbf{M} is a matrix whose components are

$$M(k_i, k_j) = \delta_{ij} + \frac{dk_j}{2\pi} P_{f,\alpha}(k_i - k_j). \quad (3.14)$$

In other words, from eq. (3.13), one can in principle obtain:

$$\mathbf{P}_{f,\beta} = \mathbf{M}^{-1} \cdot (\mathbf{P}_{f,\text{tot}} - \mathbf{P}_{f,\alpha}) \quad (3.15)$$

While such an inversion is useful for visually inspecting the Ly β power spectrum, in practice it can be noisy and one is likely better off focusing on the total power but keeping in mind that the Ly α contribution is known.

We therefore will not pursue the path of inversion here. Instead, we will be content with posing the question: how different is the total observable power $P_{f,\text{tot}}$ for models that are quite degenerate in their Ly α power, for instance those shown in Fig. 3.3?

The answer is provided by Fig. 3.4. Shown here is the fractional difference (squared) in the total power (top curve) between the two models labeled *A* and

B ($\alpha = 0$ and $\alpha = 0.4$ respectively) in Fig. 3.3. The total power here is computed using eq. (3.12) by taking $P_{f,\beta}$ at $\bar{z}_\beta = 3.74$, and $P_{f,\alpha}$ at $\bar{z}_\alpha = 3.0$.

For comparison, we show in the same figure the fractional difference in the Ly α power (lower curve) between the same two models, at the same redshift as the Ly β power, i.e. $z = 3.74$. Comparing the two curves tells us how much more the total power (due to the information from Ly β absorption) can constrain the equation of state at $z = 3.74$ compared to the Ly α power spectrum alone. We assume implicitly here that $P_{f,\alpha}$ at $\bar{z}_\alpha = 3.0$ is well known from data at low redshifts.⁶

From Fig. 3.4, we can infer the signal-to-noise (S/N) with which one can distinguish between the two different equations of state (models A and B). The $(S/N)^2$ is given by

$$(S/N)^2 = \sum_k (P_f^A(k) - P_f^B(k))^2 / \sigma_P(k)^2 \quad (3.16)$$

where P_f^A and P_f^B are the power spectra for model A and B respectively (P_f here can stand for either $P_{f,\alpha}$ or $P_{f,tot}$), and $\sigma_P(k)^2$ is the variance in power (here taken to be that for model B). The summation extends to all modes with positive k 's, up to $k_{\max} = 0.12$ s/km. The power at higher k is expected to be contaminated significantly by metal lines (McDonald et al. 2000) and so the sum is truncated at k_{\max} . The variance $\sigma_P(k)^2$ equals $(P_f^B(k) + \text{shot})^2$, if one approximates the fluctuations as Gaussian random (see Hui et al. 2001). It is likely inaccurate to assume Gaussian errors for some of the high k modes considered here. A more accurate error estimate is, however, unlikely to change our main point that the Ly β flux power spectrum distinguishes between models with different temperature-density relations, α , that have identical Ly α flux power spectra. The shot-noise term 'shot' is approximately equal to $(\Delta u / \langle e^{-\tau} \rangle)(n/s)^2$, where Δu is the size of a pixel in km/s, and s/n is the signal-to-noise per pixel of the data (different from S/N defined above). High quality spectra (e.g. Kim et al. 1997, Kirkman & Tytler 1997, Simcoe, Sargent & Rauch

⁶In order to calculate the total power, we use the same $P_{f,\alpha}$ at $\bar{z}_\alpha = 3.0$ in each of model A and model B – the difference in the total power of these models comes only from differences in their Ly β power.

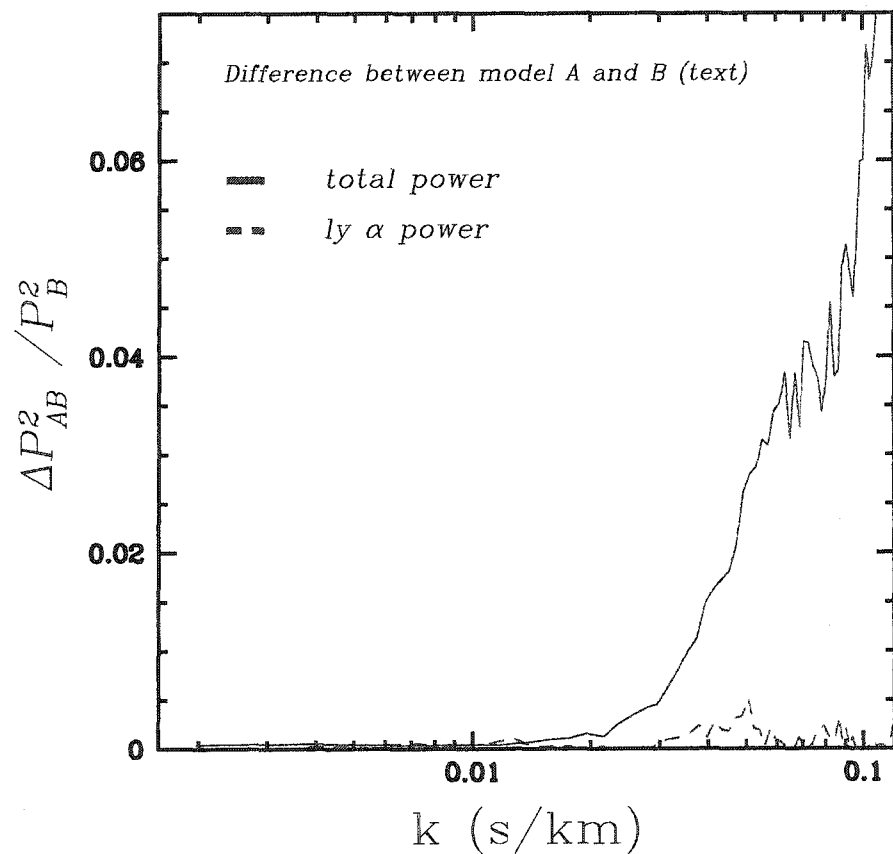


Figure 3.4 Fractional differences (squared) between the two models A and B (with the slope of the equation of state $\alpha = 0.0$ and $\alpha = 0.4$ respectively; see Fig. 3.2.) in the total and Ly α power spectra.

2002, Kim et al. 2002) often have a sufficiently low shot-noise that shot-noise can be ignored altogether, in which case, $(S/N)^2 = \sum_k (P_f^A(k) - P_f^B(k))^2 / P_f^B(k)^2$, which is the area under the curve shown in Fig. (3.4).

We find that using the Ly α power spectrum at a mean redshift of $z = 3.74$ gives a discriminating power of $(S/N)^2 = 0.8$, while using the total power from the Ly $\alpha + \beta$ region (corresponding to Ly β at the same $z = 3.74$) gives $(S/N)^2 = 7.6$. This is the $(S/N)^2$ for one line of sight, assuming that the Ly α and Ly $\alpha + \beta$ regions have a length of 5.1×10^4 km/s and $\frac{\lambda_\alpha^0 - \lambda_\beta^0}{\lambda_\beta^0 - \lambda_\gamma^0} \times 5.1 \times 10^4 = 1.4 \times 10^4$ km/s respectively. The discriminating power $(S/N)^2$ scales linearly with the number of line of sights used. Note that this estimate assumes that one has enough resolution to measure the power spectra at high k (up to $k = 0.12$ s/km) i.e. a resolution of Full-Width-at-Half-Maximum (FWHM) = 8 km/s or better. In summary, using the Ly β forest boosts the discriminating power (S/N) between an equation of state of $\alpha = 0$ and an equation of state $\alpha = 0.4$ by a factor of ~ 3 . If only modes up to $k = 0.1$ s/km are included then this number goes down to 2.5. These numbers are typical for models very close in Ly α .

To completely *quantify* how much better one can constrain the equation of state, α , using the Ly β flux power spectrum in addition to the Ly α flux power spectrum, a more rigorous approach is necessary. One should run a large grid of simulated models, simulating both $P_{f,\text{tot}}$ and $P_{f,\alpha}$, compare with mock data, and marginalize over all of the other modeling parameters to obtain the reduced likelihood function for α . A comparison between the resulting likelihood function formed using $P_{f,\alpha}$ alone, with that formed using $P_{f,\text{tot}}$ plus $P_{f,\alpha}$, quantifies how much one gains using the Ly β forest. Here we are content to illustrate that the Ly β flux power spectrum adds extra information on α that is not available from the Ly α flux power spectrum alone (Fig. 3.3), without completely quantifying how much tighter the resulting constraints on α are.

3.4 Discussion

The discussion in the last section suggests that the Ly β forest can indeed be beneficially used in conjunction with the Ly α forest to help discriminate between different models, especially between different equations of state. The reason for its utility lies in its sensitivity to higher overdensities. Better measurements of the equation of state are useful in constraining the reionization history of the universe (Theuns et al. 2002, Hui & Haiman 2003). Since spectra of quasars at sufficiently high redshifts often extend well into the Ly β forest, there is no reason not to exploit this part of the spectrum to increase the scientific return. An alternative possibility for constraining the equation of state is to use the Ly α flux bispectrum in conjunction with the flux power spectrum. Referring to Table 3 of Mandelbaum et al. (2003), it appears that combining the flux bispectrum and power spectrum yields tighter constraints on the temperature density relation than using the power spectrum alone.

Zaldarriaga, Scoccimarro & Hui (2001) pointed out that from the Ly α power spectrum alone, there is a near-degeneracy between models that trade off variations in the mass power spectral index n_s with variations in the equation of state. Our finding that the Ly β forest can place stronger constraints on the equation of state suggests one might be able to break this degeneracy using the Ly β power spectrum.

We have carried out a similar experiment as that in Fig. 3.4, except we replace models A and B by the following two models: one has $n_s = 0.7$, $\alpha = 0.0$, $T_0 = 2.1 \times 10^4$ °K, and the other has $n_s = 1.1$, $\alpha = 0.6$ and $T_0 = 1.6 \times 10^4$ °K (see eq. (3.4) for definitions of α and T_0) – these two models have quite similar Ly α power spectra. The total power distinguishes between the models at a level similar to that shown in Fig. 4. However a perhaps more readily realizable option is to break the degeneracy by measuring the Ly α power spectrum as accurately as possible on large scales, $k \sim 0.001 - 0.01$ s/km. In this range the models *are* different in the Ly α power spectrum, albeit at a level that is too small to distinguish with existing data. Quasar spectra from the Sloan Digital Sky Survey are well suited for this.

An interesting use of the Ly β forest is to search for signs of feedback processes

in the IGM. Recent interest in the Ly α forest as a cosmological probe relies on a framework in which fluctuations in the forest arise naturally from gravitational instability (e.g. Bi, Borner, & Chu 1992, Cen et al. 1994, Zhang et al. 1995, Reisenegger & Miralda-Escude 1995, Hernquist et al. 1996, Miralda-Escude et al. 1996, Muecket et al. 1996, Bi & Davidsen 1997, Bond & Wadsley 1997, Rauch et al. 1997, Hui, Gnedin & Zhang 1997, Croft et al. 1998, Theuns et al. 1999, Nusser & Haehnelt 2000, McDonald et al. 2000, White & Croft 2000, Meiksin et al. 2001, Pichon et al. 2001, Croft et al. 2002, Gnedin & Hamilton 2002, Viel et al. 2002). An important assumption behind this picture is that feedback processes, such as galactic winds (Adelberger et al. 2003), do not significantly disturb the IGM. The good agreement between observations (particularly the Ly α transmission power spectrum) and the gravitational instability model is often used as an argument that feedback processes, while inevitably present, do not affect large volumes of the IGM. A reasonable expectation is that they preferentially affect higher density regions. If so, the Ly β forest offers a better hope of testing for the presence of such feedback processes. Particularly interesting is the fact that once the gravitational instability model parameters (such as the mass power spectrum, cosmology, etc) are tuned to match observations of the Ly α forest, there are definite predictions for the correlations observed in the Ly β forest, since Ly α and Ly β optical depths are simply related by a rescaling in the cross-section. As we have discussed, changing the slope of the equation of state (α) does seem to modify the Ly β power spectrum while leaving the Ly α power spectrum relatively unchanged. Feedback processes might behave in the same way i.e. affecting the Ly β forest more than the Ly α forest, except that it is unlikely their effects can be mimicked simply by varying α . Galactic winds for instance change the density structure of the IGM, by creating evacuated shells around galaxies. They might also introduce a larger than expected scatter in the IGM temperature at high overdensities.

It is important to reiterate the method we advocate is *not* to decipher the Ly β forest on an absorption-line by absorption-line basis. Rather, the strategy is to sta-

tistically detect the presence of Ly β correlation, exploiting the fact that the Ly α and Ly β absorptions that fall within the Ly $\alpha + \beta$ region of a quasar spectrum are uncorrelated (eq. (3.3)). A natural question is: how good an approximation is it? The fractional correction to the first equality of eq. (3.3) is the two-point correlation between Ly α and Ly β transmission fluctuations at a velocity separation of $u \sim 5.1 \times 10^4$ km/s (eq. (3.2)). It is safe to assume that this correlation is weaker than the Ly α two-point correlation ($\xi_{f,\alpha}$; see eq. (3.6)), since we know from experience that Ly β absorption weakens the correlation (compare the Ly α and Ly β curves in Fig. 3.3). The observed two-point correlation function in the Ly α forest has only been reliably measured at velocity separations of $u \lesssim 1700$ km/s (McDonald et al. 2000). In order to estimate the two-point correlation function at velocity separations of $u \sim 5.1 \times 10^4$ km/s, we follow the approach of §2.4 and extrapolate our simulation measurements to large scales assuming linear biasing (Scherrer & Weinberg 1998, McDonald et al. 2000, Lidz et al. 2002). The resulting estimate is $\xi_{f,\alpha}(u = 5.1 \times 10^4 \text{ km/s}) \lesssim 10^{-5}$. Therefore, any correction to the first part of equation (3.3), $\langle e^{-\tau_{\text{tot}}(\lambda)} \rangle = \langle e^{-\tau_\alpha(z_\alpha)} \rangle \langle e^{-\tau_\beta(z_\beta)} \rangle$, must be very small: $\lesssim 10^{-5}$. Such a correction is even smaller at lower redshifts where the two-point correlation is weaker. We can similarly estimate the corrections to the factorization of the two-point function (second part of eq. (3.3), or equivalently, eq. (3.10)). The fractional error we make in the two point function is roughly $\sim 2\xi_{f,\alpha\beta}(u_{\alpha\beta}, \bar{z}_{\alpha\beta})/\xi_{f,\beta}(u, \bar{z}_\beta)$. Here $\xi_{f,\alpha\beta}$ refers to the two point correlation between the Ly β absorber that absorbs at observed wavelength λ^2 and the Ly α absorber that absorbs at λ^1 , $\bar{z}_{\alpha\beta}$ is the mean redshift between these absorbers, and $u_{\alpha\beta}$ is their velocity separation. The fractional error depends on the relative size of u and $u_{\alpha\beta}$. Here we estimate the error when the Ly β absorbers are separated by one correlation length, $u \sim 100$ km/s, and situated at $\bar{z}_\beta = 3.74$. In this case the Ly α absorber is separated from the Ly β absorber by $u_{\alpha\beta} \sim 5.1 \times 10^4$ km/s. A conservative error estimate then comes from taking $\xi_{f,\beta}(u, \bar{z}_\beta) \sim \xi_{f,\alpha}(u, \bar{z}_\beta)/5$, (see Fig. 3.3), and $\xi_{f,\alpha\beta}(u_{\alpha\beta}, \bar{z}_{\alpha\beta}) \sim \xi_{f,\alpha}(u_{\alpha\beta}, \bar{z}_\beta)/\sqrt{5}$. From McDonald et al. (2000), the observed two-point function at a separation of one corre-

lation length is $\xi_{f,\alpha}(u \sim 100 \text{ km/s}, \bar{z} \sim 4) \sim 0.2$, which gives that the fractional error is $\lesssim (10/\sqrt{5}) \frac{10^{-5}}{0.2} \sim 0.03\%$. For very widely spaced pixels in the quasar spectrum, the fractional error is larger, but these pixels have a negligible correlation.

Two issues are worth further exploration. First, one must take care in masking out the intervening metal absorption lines in the Ly $\alpha + \beta$ region of the spectrum, just as one normally does in the Ly α forest. Metal lines that cannot be easily masked out, such as OVI, can be suitably divided out using a similar method to the one mentioned in this chapter i.e. use lines of sight where the red-side of Lyman-alpha coincides in wavelengths with the Ly β forest of interest; the two-point correlation of metal absorption from these lines of sight can be used to take out the metal contamination, much like how we take out the Ly α contamination to the Ly β forest (a similar technique for 'cleaning' the Ly α forest has been developed by McDonald and Seljak, private communication). Second, it is interesting to explore whether the ideas presented here can be extended to the higher Lyman series. While this is in principle possible, it is likely that the combination of diminishing path lengths, and the increasing entanglement of different kinds of absorption (i.e. the coexistence of Ly α , β , γ , and so on), makes it difficult to exploit the factorization of correlations in practice.

Chapter 4

Constraining Dark Energy with the Ly α Forest

4.1 Introduction

Motivated by recent cosmological constraints from the Ly α forest flux/transmission auto power spectrum (e.g. Croft et al. 1998, 1999, 2002, Hui 1999, McDonald et al. 2000, Zaldarriaga, Hui & Tegmark 2001a, Zaldarriaga, Scoccimarro & Hui, 2003, Gnedin & Hamilton 2002), it is natural to extend observations and simulations to compare the cross-correlation, or in Fourier space the cross spectrum, between the absorption in neighboring lines of sight. Measuring the flux cross spectrum is a more ambitious project observationally than measuring the auto spectrum because extracting a good signal requires Ly α forest spectra of many close quasar pairs, which are rare. However, good observations of the Ly α forest in a handful of close quasar pairs have already existed for several years (Bechtold et al. 1994, Crofts & Fang 1998, Petitjean et al. 1998), and yielded information on the size and shape of Ly α absorbers. Theoretically, simulating the cross-correlation is challenging since it depends more sensitively on redshift distortions than the auto spectrum, the detailed modeling of which requires large volume, high resolution simulations. Although difficult to obtain, the information contained in the cross-correlation signal is rich. In particular, using

the auto spectrum of the absorption in the Ly α forest and the cross spectrum one can constrain the cosmological constant or dark energy through a version of the Alcock-Paczyński (AP) test (Alcock & Paczyński 1979, McDonald & Miralda-Escudé 1999, Hui, Stebbins & Burles 1999, McDonald 2003, Lin & Norman 2002, Rollinde et al. 2003). In spite of this, little work has been done in comparing pair spectra with simulations using the modern picture of the Ly α forest and focusing on continuous-field statistics. (See however Rollinde et al. 2003.)

As a step in this direction, in this chapter we aim to measure the cross spectrum from data and from simulations. Our present data set, consisting of five pairs with $z \gtrsim 2.2$, includes two new pairs and a triplet from Crotts & Fang (1998). From our measurements of the cross spectrum, which have large error bars owing to the small number of pairs in our current sample, and using the precise measurements of the auto spectrum from Croft et al. (2002), we attempt to obtain a constraint on the cosmological constant.

It is appropriate to ask: why carry out this exercise if we already know the value of the cosmological constant to fair accuracy from supernova measurements (Riess et al. 1998, Perlmutter et al. 1999), especially when used in conjunction with the microwave background anisotropies (Spergel et al. 2003)? The answer lies partly in the elegance of the Alcock-Paczyński test, in that it does not require a standard candle, and is therefore free of assumptions about evolution. The application to the Ly α forest of course suffers from systematics of its own. It is the cross-checks provided by different methods that give us confidence in our current picture of the universe. The present work should be viewed as a warm-up exercise – as quasar pair samples increase in size, the method described here might prove to give competitive constraints on the cosmological constant/dark energy, and as will be discussed below, the resulting constraints will be nicely complementary to those from other methods.

The present chapter is organized as follows. In §4.2 we briefly review the AP test, its application using the Ly α forest and its sensitivity to cosmological parameters, especially dark energy. In §4.3 we describe the statistics that we use in our implemen-

tation of the AP test and describe how we measure them from simulations. In §4.4 we describe and quantify the effect of redshift distortions on the three-dimensional flux power spectrum by measurements from simulations. In §4.5 we present measurements of the cross spectrum from a small sample of quasar pairs and attempt to place a constraint on the cosmological constant from the measurements. The constraint comes from comparing simulated auto and cross spectra from a grid of models with the observed auto and cross spectra. The grid of models examined here is rather small, but our constraints are correspondingly weak. In §4.6 we consider the possibilities for constraining dark energy with future observations and consider the dependence on spectral resolution and shot noise. This section should be helpful in planning future observations. In §4.7 we conclude the chapter. In Appendix A we include some details concerning the simulations we run and show resolution and boxsize tests.

4.2 The AP Test

In this section we briefly review the AP test and its application in the Ly α forest. Alcock & Paczyński (1979) considered an astrophysical object, with redshift extent Δz and angular extent $\Delta\theta$, and pointed out that the object's inferred shape depends on cosmology. To be specific, the dependence on cosmology is as follows. The length of the hypothetical object along the line of sight in velocity units is $u_{\parallel} = \frac{c\Delta z}{1+z}$, and its perpendicular extent in velocity units is $u_{\perp} = \frac{H(z)}{1+z} D_A(z)\Delta\theta$. Here z is the mean redshift of the object, and $H(z)$ and $D_A(z)$ are respectively the Hubble parameter and the co-moving angular diameter distance at the mean redshift. The radiation-free Hubble parameter is $H(z) = H_0 [\Omega_m(1+z)^3 + \Omega_k(1+z)^2 + \Omega_\Lambda]^{\frac{1}{2}}$, where H_0 is the present day Hubble parameter, and Ω_m , Ω_k , Ω_Λ are the present day matter, curvature and cosmological constant contributions to the energy density. The curvature density is related to the matter and cosmological constant densities by $\Omega_k = |1 - \Omega_m - \Omega_\Lambda|$. The co-moving angular diameter distance, (as opposed to the proper angular diameter distance), is $D_A(z) = \frac{c}{H_0} \frac{1}{\sqrt{\Omega_k}} S_k \left[\sqrt{\Omega_k} \int_0^z \frac{dz'}{H(z')/H_0} \right]$. The function $S_k(x)$ that appears in

the angular diameter distance is $S_k(x) = \sin(x)$ for a closed universe, $S_k(x) = \sinh(x)$ for an open universe and $S_k(x) = x$ for a flat universe, in which case $D_A(z)$ is just the co-moving distance out to redshift z .

The ratio, $\frac{u_{\parallel}}{u_{\perp}}$, is a measure of the object's shape, equal to one for spherical objects. The cosmological dependence of this ratio means that observers converting angles and redshifts to distances assuming different cosmologies will reach different conclusions about the object's shape. One can assume any possible value of the cosmological parameters Ω_m , Ω_Λ ; if the assumed parameters differ from the true cosmology, an object's inferred shape will be distorted from its true shape. In particular we consider the distortion an observer assuming an Einstein-de-Sitter (EDS) cosmology measures in a universe with a cosmological constant (a Lambda cosmology), or any other postulated "true" cosmology. We define a squashing factor, $g_{\text{squash}}(z)$, to quantify the distortion in the object's shape (see e.g. Ballinger et al. 1997),

$$g_{\text{squash}}(z) = \left(\frac{u'_{\perp}}{u'_{\parallel}} \right) \left(\frac{u_{\parallel}}{u_{\perp}} \right) = \frac{H'(z)D'_A(z)}{H(z)D_A(z)} \quad (4.1)$$

The primed variables represent coordinates in the EDS cosmology and the unprimed variables denote coordinates in the Lambda (or other postulated "true") cosmology. This ratio is larger than one in the case of a Lambda cosmology; $\frac{H'(z)D'_A(z)}{H(z)D_A(z)} > 1$. The object appears squashed along the line of sight to the observer converting redshifts and angles to distances assuming an EDS cosmology; i.e., a spherical object with true dimensions $u_{\parallel} = u_{\perp}$, seems squashed by a factor g_{squash} so that $u'_{\perp} > u'_{\parallel}$. In figure (4.1) we plot the squashing factor, $g_{\text{squash}}(z)$, as a function of redshift for several different cosmological models. In each case, the squashing factor shown is the squashing an EDS observer measures in a given "true" cosmology. In the top panel we show the squashing factor for several different values of Ω_Λ , assuming a flat universe. In the middle panel we show the squashing factor assuming an open universe with no cosmological constant. The squashing factors in the open universe, zero cosmological constant models are close to unity, the squashing effect is always $\lesssim 10\%$ and typically only a $\sim 5\%$ effect in these models. As we can see in the top panel of the figure,

the squashing effect is rather sensitive, however, to the presence of a cosmological constant. The squashing factor in the flat, Lambda universes shown here rises quickly with redshift, but plateaus around $z \sim 1$. After reaching this plateau, the squashing effect is only a $\sim 20\%$ effect for an $\Omega_\Lambda = 0.7$ universe, but is a $\sim 50\%$ effect for an $\Omega_\Lambda = 0.9$ flat universe. The plateau effect arises because the squashing is sensitive to the presence of a cosmological constant, which is small at high redshift. At redshifts beyond the plateau, the AP test should be particularly good at constraining the existence of a very large cosmological constant.

We also consider the sensitivity of the AP test to the equation of state of a dark energy, or quintessence, component to the energy density (Hui, Stebbins & Burles 1999). The equation of state of the quintessence component is parameterized by $p = w\rho_Q$, where p is the (negative) pressure, and ρ_Q is the component's energy density. Here we consider the equation of state to be constant as a function of redshift, in which case $\rho_Q = \Omega_Q(1+z)^{3(1+w)}$. In the bottom panel of figure (4.1) we plot the squashing factor as a function of redshift for a few different quintessence cosmologies. At redshifts near $z = 3$, where one can apply the AP test to the Ly α forest, the squashing factor is extremely similar for all of the quintessence cosmologies considered. This is in accord with McDonald (2003), (see also Kujat et al. 2002), who notes that this insensitivity to w makes the Ly α forest a particularly good probe of Ω_m since constraints obtained on Ω_m are then insensitive to prior assumptions regarding w . The squashing factor at this redshift is more sensitive to the equation of state of dark energy, w , if $w(z \sim 3) \gtrsim -0.4$, however (McDonald 2003).¹ At lower and higher redshifts, the squashing factor is more sensitive to the equation of state, w . At low redshift the difference between squashing factors for the different quintessence cosmologies peaks near $z \sim 0.5$. The difference between squashing factors in a $w = -0.5$ cosmology and in a $w = -1$ cosmology is still only $\sim 6\%$ near this redshift, but the clustering of low/intermediate redshift objects is certainly a better probe of w than the Ly α

¹As we discuss below, the expected signal from the Ly α AP test also depends on the effect of redshift distortions. The equation of state w does affect redshift distortions, but only to a small degree, as long as $w \lesssim -0.4$.

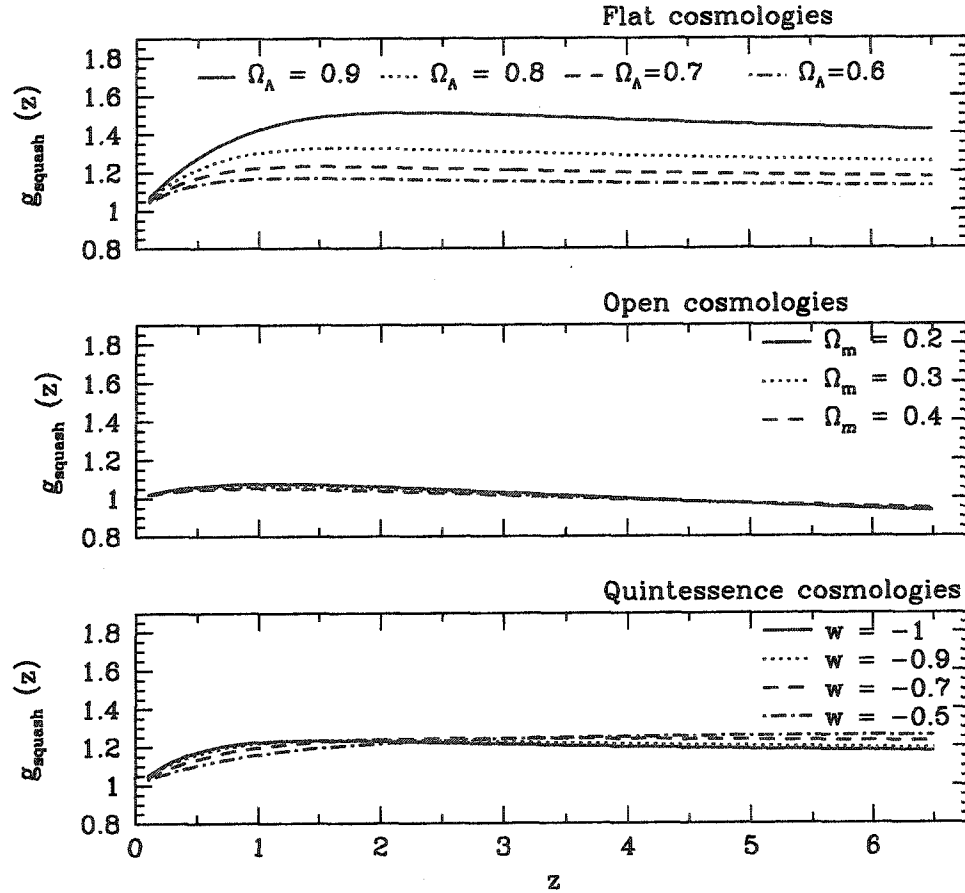


Figure 4.1 The top panel shows the squashing factor, $g_{\text{squash}}(z)$, defined in §4.2, as a function of redshift for various flat, Lambda cosmologies. The middle panel shows the same factor for open universes. The bottom panel shows the squashing factor for flat quintessence models with $\Omega_m = 0.3$. The equation of state of the quintessence field is assumed to be constant as a function of redshift. In each panel, the squashing factor is defined relative to the EDS case; it is the squashing an observer converting angles and redshifts to distances assuming an EDS cosmology would measure in a given “true” cosmology.

forest at $z \sim 3$. For instance, Matsubara & Szalay (2002) suggest applying the AP test using the clustering of luminous red galaxies, as a good low/intermediate redshift sample, to constrain w . At any rate, we now have an idea of the size of the geometric distortion in different cosmologies, and proceed to discuss some complications in applying the AP test with real ‘astrophysical objects’.

To apply this test in the pure form mentioned above, one needs a spherical object or an object of other known shape, expanding with the Hubble flow. The three-dimensional power spectrum of galaxy or quasar clustering, $P(k)$, for instance, could provide such an object since it should be spherical by the cosmological principle if measured in real space (see e.g., Phillips 1994, Matsubara & Suto 1996, Ballinger,Peacock & Heavens 1997, Popowski et al. 1998, Outram et al. 2001, Hoyle et al. 2002, Seo & Eisenstein 2003. See also Ryden 1995 and Ryden & Melott 1996 for an application using the shape of voids). This quantity is not directly accessible to observations, however, because measurements are performed in redshift space rather than in real space; one measures redshifts rather than absolute distances along the line of sight.² The shape of the observed three-dimensional power spectrum is thereby distorted by the presence of peculiar velocities which affect distances inferred along the line of sight, but not across the line of sight. On large scales, as overdense regions undergo gravitational infall, the clustering pattern is squashed along the line of sight by these redshift-space distortions, mimicking the effect of a cosmological constant. On small scales, redshift distortions elongate structure along the line of sight in a “finger-of-god” effect. To use the AP test one must accurately model the effect of the redshift distortions. In the case of galaxy or quasar clustering, this requires knowledge of the biasing between the dark matter clustering and the galaxy/quasar clustering. The underlying physics of galaxy biasing is somewhat uncertain, making a first principles prediction of the bias difficult, forcing one to determine the biasing

²Of course one can measure the real space power spectrum by considering only transverse modes, i.e. $P_r(k) = P_s(k_{\parallel} = 0, k_{\perp} = k)$ (see e.g. Hamilton & Tegmark 2002, Zehavi et al. 2003), but this is not helpful for the AP test where one wants to compare clustering along the line of sight to that across the lines of sight.

in other ways. The use of the galaxy bispectrum is one such promising method (Fry 1994, Scoccimarro et al. 2001, Verde et al. 2002), but it is as yet unclear whether the bias obtained in this way can be used in conjunction with the usual linear Kaiser formula (Kaiser 1987) to describe redshift distortions to sufficient accuracy at mildly nonlinear scales (Scoccimarro & Sheth 2002). This makes application of the AP test to galaxy surveys non-trivial, because one must disentangle the degenerate effects of redshift distortions, which depend on the biasing, and the cosmological distortion.

The proposed versions of the AP test using the Ly α forest at least partly circumvent this difficulty (McDonald & Miralda-Escudé 1999, Hui, Stebbins & Burles 1999). In these versions of the AP test, one uses the power spectrum of fluctuations in absorption in the Ly α forest as the ‘astrophysical object’ for applying the test. In the case of the forest, there is also a biasing that affects the redshift distortions, but the relevant biasing is between the fluctuations in the Ly α absorption and the dark matter fluctuations. The advantage provided by the forest is that the physics of the absorbing gas is relatively simple, unlike the physics involved in galaxy biasing. The relevant physics is primarily just that of gas in photoionization equilibrium with an external radiation field. On large scales the hydrogen gas distribution follows the dark matter distribution – i.e. gravity-driven, and on small scales it is Jeans pressure-smoothed (see e.g. Cen et al. 1994, Zhang et al. 1995, Hernquist et al. 1996, Miralda-Escudé 1996, Muecket et al. 1996, Bi & Davidsen 1997, Bond & Wadsley 1997, Hui et al. 1997, Croft et al. 1998, Theuns et al. 1999, Bryan et al. 1999, Nusser & Haehnelt 1999). The hope is that one can thereby use numerical simulations to model this simple physics, and understand the biasing between the flux power spectrum and the mass power spectrum. In this way we might model the effect of redshift distortions from first principles and thereby isolate the cosmological distortion. One might worry that the relevant physics is actually not so simple and that the small scale structure of the absorbing gas is modified by hydrodynamic effects, such as massive outflows from galaxies (Adelberger et al. 2003), that are not modeled properly, or at all, in simulations. There is direct observational evidence that indicates that

this is not the case, at least near $z \sim 3$ for the low column density gas responsible for most of the absorption in the Ly α forest. Rauch et al. (2001), by directly measuring the cross-correlation between lines of sight towards a lensed quasar, find, in fact, that the density field is quite smooth on small scales, arguing against a turbulent IGM constantly stirred up by massive outflows. One might also worry about the effect of a fluctuating ionizing background, but at $z \sim 3$, this has been shown to be negligible on relevant scales of interest (Croft et al. 1999, Meiksin & White 2004). A further possible systematic effect is from spatial fluctuations in the temperature of the IGM (Zaldarriaga 2002), expected if HeII is reionized near $z \sim 3$ (Theuns et al. 2002). Another line of evidence, however, that supports the simple gravitational instability picture of the forest comes from higher order statistics – gravity predicts a unique hierarchy of correlations, which so far seems to be consistent with data (either from bispectrum type measurements (Zaldarriaga et al. 2001b; see however Viel et al. 2003), or the one point probability distribution of flux (PDF) (e.g. Gaztanaga & Croft 1999, McDonald et al. 2000a)). While increasing amount of data will test these assumptions more precisely, it is worthwhile to push theoretical and observational efforts forward to obtain further cosmological constraints using, for instance, the AP test.

One other important difference with the case of galaxy clustering is that in the Ly α forest one does not directly measure the full three-dimensional flux power spectrum. Instead one measures the power spectrum of flux fluctuations along a line of sight (the auto spectrum) and the cross-correlation of power between two neighboring lines of sight (the cross spectrum). An observer measuring a given auto spectrum will infer the wrong cross spectrum if the observer assumes an incorrect cosmology in converting from the observed angular separation between the lines of sight to their transverse velocity separation. If the true cosmology is a Lambda cosmology, an observer converting between angles and distances assuming an EDS cosmology will infer too large a transverse velocity separation between the two lines of sight and predict too weak a cross correlation.

4.3 Simulation measurements of the flux power spectra

Our basic strategy for using the AP test in the Ly α forest is to simultaneously generate auto spectra and cross spectra from simulations for a range of different models describing the IGM. A model that fits the observed auto spectrum will only match the observed cross spectrum, measured at a given transverse separation, $\Delta\theta$, if the correct cosmology is assumed in converting from the observed $\Delta\theta$ to transverse velocity, $u_{\perp}(\Delta\theta)$. This, at least in principle, should allow us to constrain the underlying cosmology of the universe. In this section we define the relevant statistics and describe how we measure them from simulations. (Hui 1999, Viel et al. 2002)

It is instructive to describe the relationship of the auto spectrum and the cross spectrum to the fully three-dimensional flux power spectrum. In the presence of redshift distortions, the three-dimensional power spectrum of the flux field³, δ_f , depends on both the magnitude of the three dimensional wave vector, k , and its line of sight component, k_{\parallel} , as we discuss in §4.4. The auto spectrum, $P_{1d}(k_{\parallel})$, is related to the full (not directly observable) three-dimensional flux power spectrum, $P_F(k, \frac{k_{\parallel}}{k})$, by

$$P_{1d}(k_{\parallel}) = \int_{k_{\parallel}}^{\infty} \frac{dk'}{2\pi} k' P_F(k', \frac{k_{\parallel}}{k'}) \quad (4.2)$$

which is the general relationship between the three-dimensional power spectrum of an azimuthally symmetric random field and the projected power along a line of sight (Kaiser & Peacock 1991). Generally instead of the auto spectrum we will plot the dimensionless quantity, $k_{\parallel} P_{1d}(k_{\parallel})/\pi$, which is the contribution per interval in $\ln(k)$ to the flux variance.

³The flux power spectra considered in this chapter are power spectra of the random field $\delta_f = (f - \langle f \rangle)/\langle f \rangle$, where f is the transmitted flux and $\langle f \rangle$ is its mean. Observationally this quantity is not sensitive to estimates of the absolute continuum level, unlike the quantity $\tilde{\delta}_f = f - \langle f \rangle$, which is sometimes used. (Hui et al. 1999)

The cross spectrum, $P_x(k_{\parallel}, \Delta\theta)$ is related to the flux power spectrum by

$$P_x(k_{\parallel}, \Delta\theta) = \int_{k_{\parallel}}^{\infty} \frac{dk'}{2\pi} k' J_0 \left[\sqrt{k'^2 - k_{\parallel}^2} u_{\perp}(\Delta\theta) \right] P_F(k', \frac{k_{\parallel}}{k'}) \quad (4.3)$$

where J_0 is a zeroth order Bessel function. The above form follows from azimuthal symmetry, the Bessel function coming from an integration over azimuthal angle. The dependence on cosmology is embedded primarily in the form of $u_{\perp}(\Delta\theta)$. $P_F(k', \frac{k_{\parallel}}{k'})$ also depends on cosmology, through redshift distortions (§4.4), but the dependence should be weak for currently favored ranges of cosmologies. Again we will generally plot the dimensionless quantity, $k_{\parallel} P_x(k_{\parallel}, \Delta\theta)/\pi$. These definitions illustrate the relation between the auto and cross spectra and the full three-dimensional flux power, but in practice we measure the auto and cross spectra by one-dimensional Fast Fourier Transforms (FFTs) as described below.

4.3.1 Simulation Method

We summarize here the model parameters used in simulating the forest. The temperature of the IGM follows a power-law in the gas density, $T = T_0(1 + \delta)^{\alpha}$, where α should be between 0 and 0.6 (Hui & Gnedin 1997). From photo-ionization equilibrium, it then follows that the optical depth of a gas element is related to the gas density by $\tau = A(1 + \delta)^{\nu}$. The power law index ν is related to the power law index of the temperature-density relation by $\nu = 2.0 - 0.7\alpha$ and A is a parameter related to the intensity of the ionizing background which is adjusted to match the observed mean transmission. The optical depth is then shifted into redshift space, taking into account the effects of peculiar velocities, and then convolved with a thermal broadening window. We thereby have a recipe for creating artificial Ly α spectra from realizations of the density and velocity fields, which cosmological simulations provide us with.

In this chapter we wish to examine many different models, and will thus use N-body only simulations as opposed to hydrodynamic simulations which are much more computationally expensive. Our methodology will follow that of Zaldarriaga et al. (2001a,2003): we produce a grid of models with different points in the grid

corresponding to different models of the IGM, compute the auto and cross spectra for each model in the grid, and compare with observations. For the most part we rely on 256^3 particle, $20.0 \text{ Mpc}/\text{h}$ box size, particle-mesh (PM) simulations, run assuming an Standard-Cold-Dark-Matter (SCDM; $\Omega_m = 1$) cosmology. On the range of scales probed by the Ly α forest, the linear power spectrum is effectively power law, so running multiple simulations in an SCDM cosmology suffices to probe a range of power spectrum amplitudes and slopes. As we discuss in more detail in Appendix A, running the SCDM simulations to approximate Lambda cosmologies means that we neglect the dependence of dynamics and redshift distortions on Ω_m , but the dependence should be small since $\Omega_m(z \sim 3) \sim 1$ for the Lambda cosmologies considered. The details of the simulations are provided in Appendix A, where we also show resolution and boxsize tests.

Our N-body simulation supplies us with a realization of the dark matter density and velocity fields.⁴ To obtain the hydrogen gas density field and velocity field we smooth the dark matter density and momentum fields in order to incorporate roughly the effects of gas pressure. The smoothing is applied in k-space, after which the resulting smoothed real space density field is obtained by a three-dimensional FFT. The smoothing is described in k-space by $\delta_g(k) = \exp\left(-\frac{k^2}{k_f^2}\right) \delta_{\text{dm}}(k)$, where δ_g is the gas density, δ_{dm} is the dark matter density, and k_f describes the smoothing scale. This simplified prescription for computing the gas density fields seems likely to produce reasonably good agreement with fully hydrodynamic simulations, but more tests are warranted (Meiksin & White 2001, Gnedin & Hui 1998, McDonald 2003).

Given the gas density and velocity fields, we generate mock Ly α spectra; the gas density is mapped into an optical depth, which is shifted into redshift space, and convolved with a thermal broadening window. To summarize, then, our model of the IGM thus has several free parameters: a , the output scale factor of the simulation which is related to the power spectrum normalization; n , the slope of the primordial

⁴We use TSC interpolation to interpolate particle positions and velocities onto a mesh. We use the same number of mesh points as particles.

power spectrum which is related to the shape of the power spectrum on scales probed by Ly α forest measurements; k_f , the wave number of the pressure smoothing filter; T_0^5 , the temperature of the IGM at mean density; α , the logarithmic slope of the temperature-density relation; and $\langle f \rangle$, the mean flux in the Ly α forest. The parameter, A , related to the strength of the ionizing background, is adjusted to match the mean flux, $\langle f \rangle$, at each grid point in our grid of IGM models. To generate the cross spectrum we assume a flat universe and introduce the additional parameter Ω_Λ .

To measure the auto spectrum from a simulation we generate mock Ly α spectra along 6,000 random lines of sight, with the line of sight direction taken along each of the different box axes, and measure the auto spectrum by one-dimensional FFT, finally averaging the results over the different lines of sight. For examining our fiducial model introduced below, in order to reduce sample variance errors, we average over several different realizations of the density and velocity fields, each generated from the same cosmology, but with differing initial phases.

We then measure the cross spectrum as follows: 1) The desired angular separation between two lines of sight is converted into units of transverse cells by $u_\perp(\Delta\theta) = \frac{H(z)}{H_{\text{box}}(z)} D_A(z) \Delta\theta \frac{N^{1/3}}{L_{\text{box}}}$ cells, assuming a particular cosmology. Here $H(z)$ and $D_A(z)$ are the Hubble parameter and the co-moving angular diameter distance in the cosmology in which we wish to calculate the cross spectrum and $H_{\text{box}}(z)$ is the Hubble parameter in the cosmology of the simulation box; in this case an EDS cosmology. The parameters L_{box} and N are, respectively, the size of the simulation box in units of Mpc/h and the number of grid points. 2) We generate a flux field for 3,000 random pairs of lines of sight, each separated by a transverse distance of n_a cells, where n_a is the closest integer *less* than the desired u_\perp in cell units. 3) The same is done for an additional 3,000 random pairs of lines of sight, each of these pairs separated by n_b cells, where n_b is the closest integer *larger* than the desired u_\perp in cell units. 4) We measure the cross spectrum from the lines of sight separated by n_a cells

⁵We express T_0 in units of (km/s)². The relationship between T_0 in units of (km/s)² and T_0 in units of K is $T_0 = \frac{T_0[(\text{km/s})^2]}{165} 10^4 K$.

and from the lines of sight separated by n_b cells, and linearly interpolate between the two measurements to find the cross spectrum at the exact desired separation. 5) In considering the fiducial model introduced below, we average the results over five different realizations of the density and velocity fields.

4.3.2 Examples

From the auto and cross spectra measured in this way, we determine the goodness of fit of a model in our parameter grid by calculating, first for the auto spectrum, $\chi^2_{\text{auto}} = \sum_{i=1}^n \left[\frac{(P_{\text{sim}}(k_i) - P_{\text{obs}}(k_i))^2}{\sigma_i^2} \right]$. We then compute, as described in §4.5, the goodness of fit of the model to the observed cross spectrum, using an analogous χ^2 . We add a term coming from observational constraints on $\langle f \rangle$ to our calculated value of χ^2_{auto} . At $z = 2.82$ this term is $\chi^2 = [(\langle f \rangle - 0.682)/0.034]^2$, where the value 0.682 is from Press et al.'s (1993) measurement of the mean transmission, which, at this redshift, is in good agreement with recent measurements by Bernardi et al. (2003) from the SDSS quasar sample, although recently some authors have argued that these measurements may be biased low (Seljak, McDonald & Makarov 2003). The uncertainty in the mean transmission is taken to be 5% following Zaldarriaga et al. (2003). In the equation for χ^2_{auto} the sum runs over the data from Croft et al. (2002) with wavenumber $k_i \lesssim 0.03$ s/km, interpolated to $z = 2.82$. Here $P_{\text{obs}}(k_i)$ is the observed auto spectrum at wavenumber k_i , σ_i is Croft et al.'s (2002) observational error estimate for $P_{\text{obs}}(k_i)$, and $P_{\text{sim}}(k_i)$ is the simulation measurement interpolated to $k = k_i$. A resolution test shown in Appendix A demonstrates that our fiducial simulation, with 256^3 particles in a 20.0 Mpc/h box, gives a reliable (compared with present observational errors) flux auto spectrum on large scales, but misses some power in the auto spectrum on small scales. Because of this, we do not include the auto spectrum data at $k \gtrsim 0.03$ s/km in constructing our fits. (A plot of the auto spectrum is shown later in the text, in figure 4.10.)

From now on, whenever we refer to the fiducial model for the purpose of illustration, it refers to the following: $(a, n, k_f, T_0, \alpha, \langle f \rangle) = (0.19, 0.7, 35.0 \text{ h}^{-1} \text{ Mpc}, 250$

(km/s)², 0.2, 0.684). Similar models were found to fit the observed auto spectrum by Zaldarriaga et al. (2001a,2003). The power spectrum normalization and slope of this model can also be characterized by $\Delta^2(k_p, z = 2.82)$ and n_{eff} , which are the amplitude and slope of the linear power spectrum at $k_p = 0.03 \text{ s/km}$, $z = 2.82$ (Croft et al. 2002). This model has $\Delta^2(k_p, z = 2.82) = 0.44$, $n_{\text{eff}} = -2.7$. The fit has $\chi^2_{\text{auto}} = 6.7$. The model has roughly 4 free parameters, a , n , T_0 , and α , since k_f and $\langle f \rangle$ are fixed, and we fit to 11 data points, so there are 7 degrees of freedom. The fit, with χ^2 per degree of freedom of 0.96 is reasonable.

Since this fiducial model of the IGM provides a reasonable fit to the observed auto spectrum it is interesting to examine the cross spectra this model predicts for a range of cosmological geometries. From equation (4.1) we know how different the squashing factors in different cosmologies are, but have yet to examine how different the cross spectra are in these cosmologies. After all, the cross spectrum is the observationally relevant quantity in our study. We illustrate the difference in figure (4.2) for $\langle z \rangle = 2.82$, $\Delta\theta = 33''$ and for $\langle z \rangle = 2.89$, $\Delta\theta = 62''$, which correspond to the redshift and angular separation of two of the pairs we analyze in §4.5. The cross spectra shown in the figure are estimated from the average of 5 different simulation realizations. These predictions include the effect of redshift distortions as discussed below in §4.4. Looking first at the $\Delta\theta = 33''$ plot, it will clearly be difficult to discriminate between a flat $\Omega_\Lambda = 0.7$ cosmology and a flat $\Omega_\Lambda = 0.6$ cosmology, as already implied by the similarity of the squashing factor for these two cosmologies in figure (4.1). At $k_{\parallel} = 3.2 \times 10^{-3} \text{ s/km}$, which is twice the wavenumber at the fundamental mode, the cross spectrum in the $\Omega_\Lambda = 0.7$ cosmology only differs from the cross spectrum in an EDS cosmology by $\sim 7\%$, while the cross spectrum in the $\Omega_\Lambda = 0.6$ cosmology differs from the EDS case by only $\sim 5.5\%$. By $k_{\parallel} \sim 0.03 \text{ s/km}$, the fractional differences with the EDS case are larger, around $\sim 33\%$ for $\Omega_\Lambda = 0.7$ and $\sim 27\%$ for $\Omega_\Lambda = 0.6$. However a cosmology with a significant cosmological constant makes its presence felt, and there is a sizeable difference between a flat, $\Omega_\Lambda = 0.9$ cosmology and a flat, $\Omega_\Lambda = 0.7$ cosmology. The fractional difference between the $\Omega_\Lambda = 0.9$ case and the

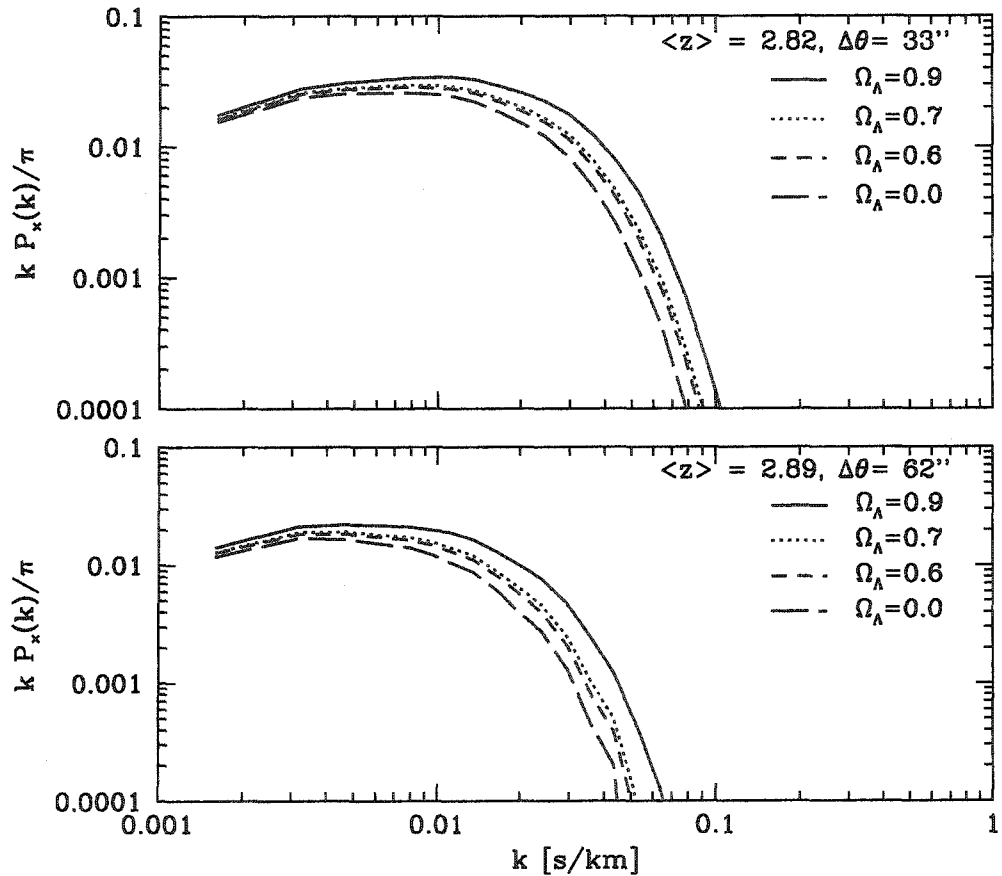


Figure 4.2 The cross spectrum for a range of flat cosmologies at $\langle z \rangle = 2.82, 2.89$, assuming a model of the IGM that provides a reasonable fit to the observed auto spectrum at each redshift. The top panel shows the cross spectrum for a separation of $\Delta\theta = 33''$ and the bottom panel shows the cross spectrum for a separation of $\Delta\theta = 62''$. These redshifts and separations correspond to those in the data set considered in §4.5.

EDS case is $\sim 14\%$ at $k_{\parallel} = 3.2 \times 10^{-3}$ s/km, and $\sim 53\%$ by $k_{\parallel} \sim 0.03$ s/km. Looking now at the $\Delta\theta = 62''$ plot, the difference between models is larger, but the magnitude of the cross spectrum is reduced slightly and the scale at which the cross spectrum turns over moves to lower k_{\parallel} . At this separation, the fractional difference between the $\Omega_{\Lambda} = 0.9$ case and the EDS case is $\sim 21\%$ at $k_{\parallel} = 3.2 \times 10^{-3}$ s/km and $\sim 73\%$ by $k_{\parallel} \sim 0.03$ s/km. As we describe in §4.6, however, the ability to discriminate between two cosmologies depends not on the fractional difference between the cross spectra in the two models, but rather on the difference between the cross spectra, divided by the square root of the sum of the squares of the true auto and cross spectra. This means that the discriminating power is actually better for the close separation, $\Delta\theta \lesssim 1'$, pairs. However, as we will flesh out in §4.6, the advantage provided by observing close separation pairs is nullified if the spectral resolution is not good enough to resolve the small scales where such models differ significantly. One can see some noise in the simulation measurement from the $\Delta\theta = 62''$ pairs at high k . Simulation measurements of the cross spectrum at large separations and high k are generally rather noisy. This is not too much of a concern for our present purposes since in this work we consider an observational data set of relatively close pairs, with poor spectral resolution, confining our measurements from data to large scales. In §4.6, however, we consider the expected cross spectrum signal at large separations, extrapolating our simulation measurements to these separations using the fitting formula proposed by McDonald (2003).

4.4 The Flux Power Spectrum and its Redshift Distortion

In order to use the AP test to determine the cosmological constant, we must take into account the effect of redshift distortions. It is our aim in this section to investigate the relative importance of cosmology versus redshift distortions in determining the anisotropy of the observed power spectrum. It is important to emphasize that while

we will make comparisons between simulations and linear theory predictions, we will not make use of the linear predictions in the rest of this work.

The detailed form of the full three-dimensional flux power spectrum involves non-linear effects, the effects of peculiar velocities and of thermal broadening. A start towards understanding these effects was made by Hui (1999), (see also McDonald & Miralda-Escudé 1999), who made a linear theory calculation of the effect of redshift distortions and found that $P_F(k, \mu) \propto (1 + \beta\mu^2)^2 e^{-\frac{k^2\mu^2}{k_s^2}} P(k)$. (Further investigations have been carried out by McDonald 2003). Here μ refers to the ratio of the component of the wavenumber along the line of sight, k_{\parallel} , to the total wavenumber, k . The optical depth is assumed to go as $\tau \propto (1 + \delta)^{\nu}$ before the effects of thermal broadening and redshift distortions are included; $P(k)$ is the mass power spectrum in real space⁶; and $\beta = f_g(\Omega_m, z)/\nu$. Here $f_g \equiv d\ln D/d\ln a$ is the logarithmic derivative of the linear growth factor, $D(a)$, and $f_g(\Omega_m, z) \sim \Omega_m(z)^{0.6}$ for Lambda cosmologies. On large scales $P_F(k, \mu)$ has the same qualitative form as the expression for the galaxy power spectrum in redshift space predicted by Kaiser (1987); the three-dimensional flux power is enhanced along the line of sight in redshift space. Here, however, the “bias factor” in the expression is given by ν , the power law in the relation between density and optical depth. On small scales the flux power spectrum is suppressed along the line of sight, as described by the factor $e^{-\frac{k^2\mu^2}{k_s^2}}$. In linear theory the smoothing scale, k_s , is the thermal broadening scale, $k_s = \sqrt{2}/\sqrt(T_0)$, where T_0 is the temperature at mean density in units of (km/s)². In the non-linear regime the flux power spectrum will be suppressed on small scales not only from thermal broadening, but also from non-linear peculiar velocities and the suppression will not generally be well described by a Gaussian. This suppression of power is analogous to the finger of god effect found in the case of the galaxy power spectrum in redshift space, but here the effect is due not only to peculiar velocities but also to thermal broadening. In this section we quantify the anisotropy due to redshift distortions by direct measurement from

⁶The power spectrum here is the baryonic power spectrum which is smoothed on small scales relative to the dark matter, $P(k) = \exp\left(-\frac{2k^2}{k_f^2}\right) P_{\text{dm}}(k)$

simulations.

We measure the three-dimensional flux power spectrum from a 512^3 , 20.0 Mpc/h simulation, assuming the fiducial model described in the last section.⁷ To measure the full three-dimensional flux power spectrum, we form the flux field at every pixel in the simulation box taking the line of sight along one of the box axes, form the power spectrum by three-dimensional FFT, then repeat the measurement with the lines of sight along the other box axes, and average the results over the three box axes.

Our measurement is illustrated in figure (4.3) where we show contours of constant flux power in the $k_{\perp} - k_{\parallel}$ plane. On large scales (small k) the contours of constant flux power have a slightly prolate shape. This means that in configuration space contours of constant correlation function would have a slightly oblate shape, signifying a squashing along the line of sight. This behavior, of the flux correlation function in redshift space, is qualitatively the same as the behavior of the galaxy correlation in redshift space; both are squashed on large scales from gravitational infall. At higher k , near $k \sim 0.05$ s/km, the situation reverses itself and the contours of constant flux power become oblate, signifying a finger-of-god elongation along the line of sight. This behavior is also exactly analogous to the behavior of the galaxy redshift space power spectrum and is qualitatively consistent with the predictions of Hui (1999), McDonald & Miralda-Escudé (1999), and McDonald (2003).

A useful statistic to quantify the measured anisotropy of the flux power spectrum is its quadrupole to monopole ratio $Q(k)$, as is often done for the galaxy power spectrum in redshift space. (See e.g., Cole, Fisher & Weinberg 1994, Hatton & Cole 1998, Scoccimarro, Couchman & Frieman 1999.) To compute this quantity one writes the anisotropic flux power spectrum, $P_F(k, \mu)$, as a sum of Legendre polynomials. The Legendre sum is $P_F(k, \mu) = \sum_{l=0}^{\infty} a_l(k) L_l(\mu)$, where $L_l(\mu)$ are the Legendre polyno-

⁷The temperature, $T_0 = 300$ (km/s)², and the temperature-density relation, $\alpha = 0.1$, are slightly different than the fiducial model from the 256^3 simulation which has $T_0 = 250$ (km/s)² and $\alpha = 0.2$. The model with the higher temperature, from the 512^3 simulation, gives a slightly better fit to the observed auto spectrum, when all data points from Croft et al.'s (2002) measurement are included in the fit. See Appendix A for resolution tests.

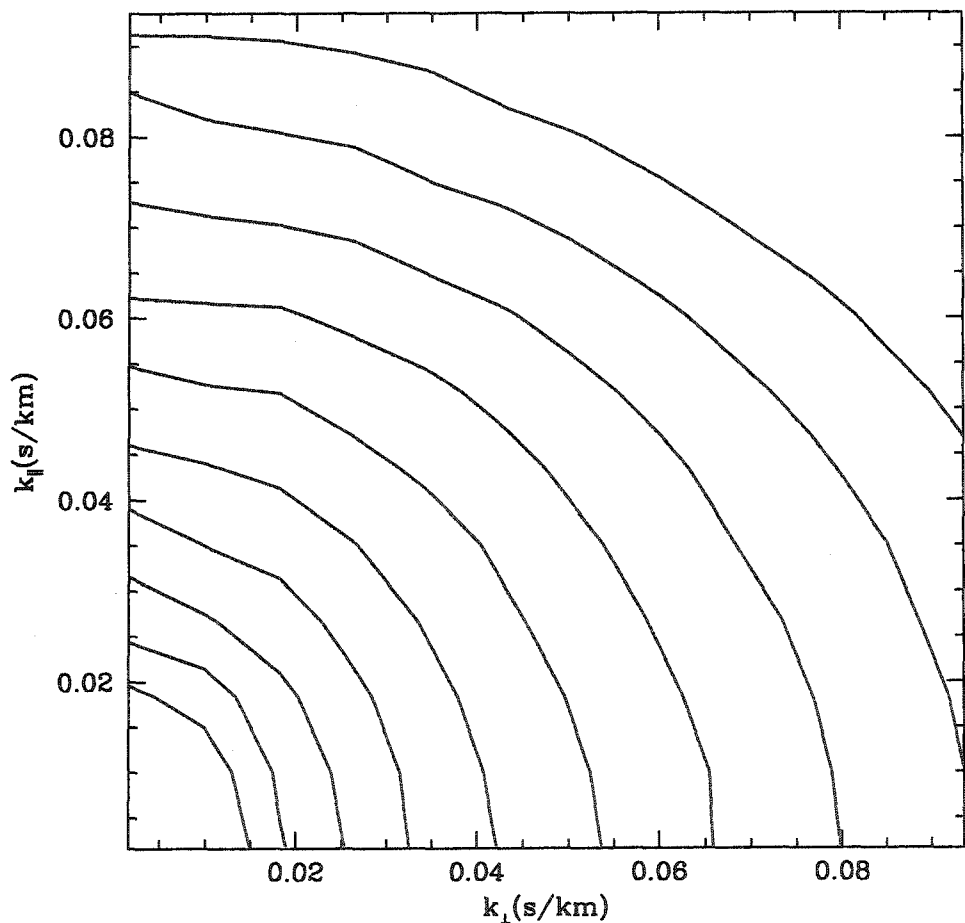


Figure 4.3 Contours of constant flux power in the $k_{\perp} - k_{\parallel}$ plane. The contours range from $\ln(P/(km/s)^3) = 6.5$ to $\ln(P/(km/s)^3) = 12.5$. The flux power is measured from an SCDM simulation with 512^3 particles in a $20.0 \text{ Mpc}/h$ box. The flux generation parameters are $(a, n, k_f, T_0, \langle f \rangle, \alpha) = (0.19, 0.7, 35.0 \text{ h Mpc}^{-1}, 300 \text{ (km/s)}^2, 0.684, 0.1)$

mials, and we wish to determine the coefficients, $a_l(k)$, in the expansion. Using the orthogonality of the Legendre polynomials we then have the quadrupole to monopole ratio,

$$Q(k) = \frac{a_2(k)}{a_0(k)} = \frac{5/2 \int_{-1}^1 d\mu \frac{1}{2} (3\mu^2 - 1) P_F(k, \mu)}{1/2 \int_{-1}^1 d\mu P_F(k, \mu)} \quad (4.4)$$

We have measured the quadrupole to monopole ratio at $z = 2.82$ assuming the same IGM model parameters as above. A plot of the measurement is shown as the solid line in figure (4.4). The measurement is shown starting from three times the fundamental mode, $k = 3.0 \times k_{\text{fun}}$, since on larger scales there are few k modes with which to estimate the anisotropy. The measurement is generally noisy since it comes from only one simulation realization. The measured quadrupole to monopole ratio has the approximate form expected given Hui's (1999) linear theory calculation. From the linear theory form of the flux power spectrum, one expects that on scales where thermal broadening is negligible, $Q(k) = \frac{4\beta/3 + 4\beta^2/7}{1 + 2\beta/3 + \beta^2/5}$. At small k , the quadrupole to monopole measurement from the simulation is positive and has approximately the linear theory magnitude, but it appears to be slightly larger on the largest scales measured. On smaller scales, the quadrupole to monopole goes negative due to the suppression of power along the line of sight from the combined effects of peculiar velocities and thermal broadening.

We caution, however, that the quadrupole to monopole ratio is somewhat sensitive to $\langle f \rangle$, which in turn is sensitive to small scale physics, some of which may be missing from our relatively low resolution, N-body simulations. It is not obvious that the linear theory calculation gives the correct biasing factor, as Hui (1999) points out. As Hui (1999) emphasizes, the redshift distortions of the flux power spectrum are complicated, involving several transformations; a transformation from gas density to neutral hydrogen density, a transformation of the optical depth into redshift space involving both a shift by peculiar velocity and convolution with a thermal broadening window, and finally an exponentiation to go from optical depth to flux. The effect then of small scale, non-linear behavior on the redshift distortions at large scales is

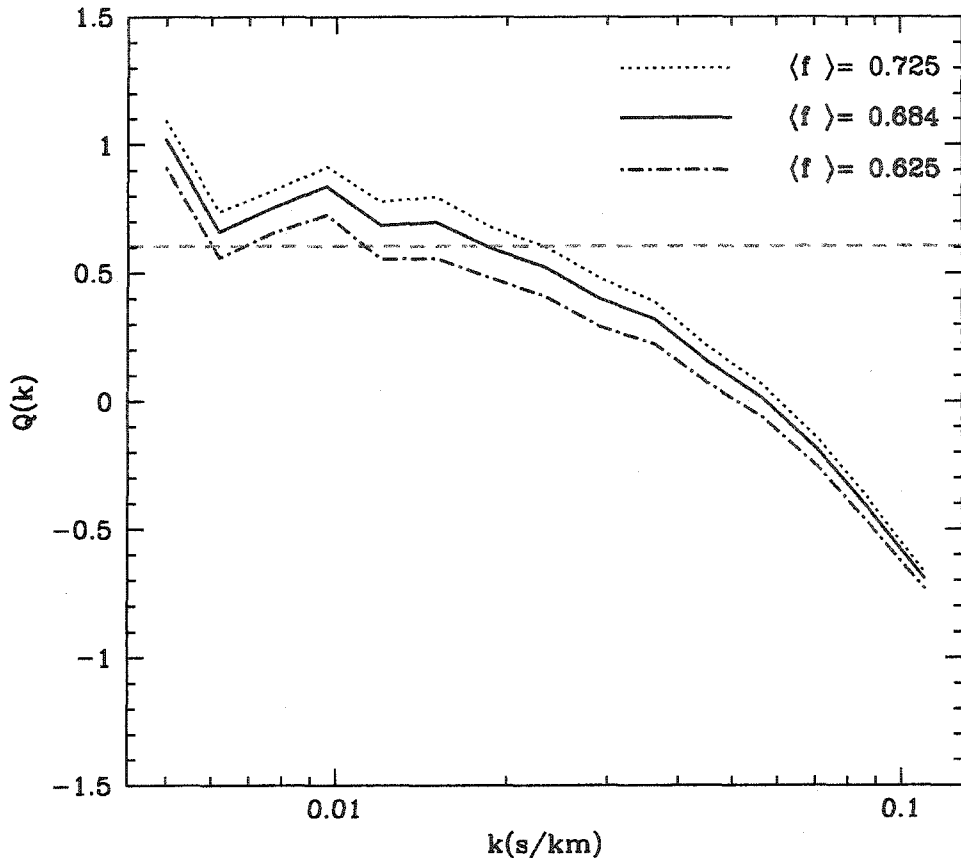


Figure 4.4 The quadrupole to monopole ratio of the flux power spectrum. The solid line is a simulation measurement with the same parameters as in figure (4.3). The simulation measurement is shown starting from $k = 3.0 \times k_{\text{fundamental}}$. The dashed line is the large scale linear theory prediction, which ignores the finger-of-god effect on small scales. We also show the quadrupole to monopole ratio for two models, identical to the above model, except with differing values of the mean transmission, $\langle f \rangle$, demonstrating the sensitivity of the measurement to $\langle f \rangle$. Note that only the model with $\langle f \rangle = 0.684$ provides a good fit to the auto spectrum.

not clear. We know, at any rate, that small scale physics is important in determining A (the parameter adjusted to match the observed mean transmission discussed in §4.3.1), which in turn affects the large scale flux power. It is perhaps not terribly surprising then that the quadrupole to monopole depends somewhat on $\langle f \rangle$, since this parameter sets which range of mass overdensities the flux field, δ_f , is sensitive to. The dotted and dot-dashed lines in figure (4.4) show the quadrupole to monopole ratios for models with $\langle f \rangle = 0.625, 0.725$, illustrating the dependence on $\langle f \rangle$.⁸ The quadrupole to monopole ratio for the model with the largest $\langle f \rangle$ is a bit larger than the fiducial model while the model with the smallest $\langle f \rangle$ has a smaller quadrupole to monopole ratio than the fiducial model. This means that the quadrupole to monopole ratio is likely to have a different magnitude at different redshifts, where the mean transmission is different. Indeed the fitting formula that McDonald (2003) found (see §4.6) for the three dimensional flux power spectrum at $\langle z \rangle \sim 2.25$ implies a somewhat larger quadrupole to monopole ratio on large scales, which is qualitatively consistent with our expectations given the larger mean transmission at that redshift. After performing these measurements and making the caveat about the dependence of our results on $\langle f \rangle$, we leave a more systematic investigation of flux power redshift distortions for future work.

Given these measurements of the anisotropy of the three-dimensional flux power spectrum due to redshift distortions, it is natural to ask how large the anisotropy from redshift distortions is in comparison to the anisotropy from cosmological distortions. To gauge the relative size of the two effects we consider the power spectrum of $f = e^{-A(1+\delta)^{\nu}}$; the flux power spectrum neglecting thermal broadening and peculiar velocities, which is isotropic. We refer to this field as *the isotropic flux field* to distinguish it from the *anisotropic flux field* that includes redshift distortions. In the top panel of figure (4.5) we show a comparison of the auto spectrum measured

⁸We caution however that all of the other parameters of the IGM remained fixed in this comparison, so that the models with high and low $\langle f \rangle$ do not provide a good fit to the observed auto spectrum. These values of $\langle f \rangle$ are also disfavored by observations. These values of $\langle f \rangle$ suffice to show, however, that the large scale redshift distortions appear sensitive to small scale physics.

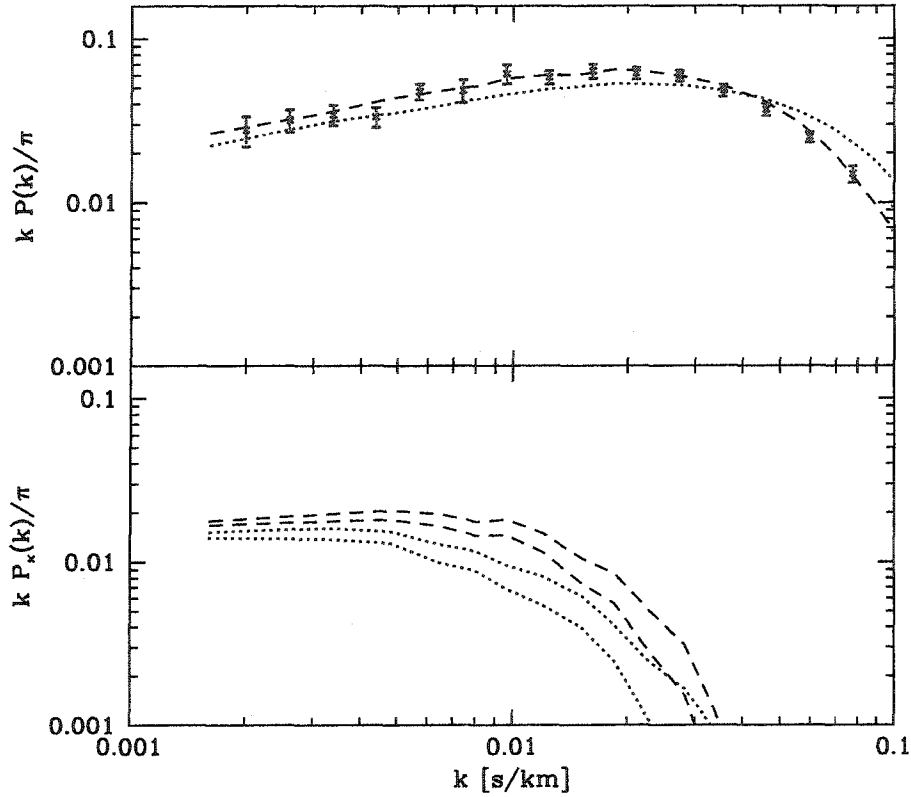


Figure 4.5 The top panel shows (dashed line) the auto spectrum from the 512^3 simulation including the effects of thermal broadening and peculiar velocities. The dotted line is the auto spectrum in the same model, without the effect of peculiar velocities and thermal broadening. The points with error bars are from Croft et al. (2002). The bottom panel shows (dashed lines) the cross spectrum measured at $\Delta\theta = 60''$ in a Lambda model (top dashed line) and in a EDS model (bottom dashed line). The dotted lines are the cross spectra measured in the same models, ignoring the effect of redshift distortions. *In calculating the cross spectra in the redshift distortion free case, the mass power spectrum amplitude of the model has been adjusted so that the corresponding auto spectrum matches observations on large scales.*

from the fully anisotropic flux field and that measured from the isotropic flux field for the same model of the IGM.⁹ On large scales, the auto spectrum measured from the anisotropic flux field is boosted compared to that measured from the isotropic flux field. On the other hand, on small scales the auto spectrum measured from the anisotropic flux field is suppressed relative to that measured from the isotropic flux field. This qualitative behavior of the auto spectrum, that redshift distortions boost the auto spectrum on large scales and suppress the auto spectrum on small scales is expected from our above measurements of the full three-dimensional flux power. How different then are the cross spectra of the isotropic flux field and the anisotropic flux field? To provide a fair comparison, we first boost the mass power spectrum normalization in the isotropic case so that the auto spectrum of the isotropic flux field matches the observed auto spectrum on large scales ($k \lesssim 0.03$ s/km). The corresponding cross spectra are shown in the bottom panel of figure (4.5) for lines of sight separated by $\Delta\theta = 60''$ in each of a Lambda ($\Omega_\Lambda = 0.7$) cosmology and an EDS cosmology. From the figure, one can see that redshift distortions significantly boost the amplitude of the cross spectrum in each cosmology. If one naively *neglects redshift distortions*, the cross spectrum one predicts in the Lambda cosmology (top dotted line) is less than that of the cross spectrum in the EDS cosmology *including redshift distortions* (bottom dashed line)! At larger separations, we expect that the geometrical effect will become more important relative to the effect of redshift distortions. At any rate, this clearly suggests that redshift distortions are an important effect and must be accounted for in detail in order to apply the Ly α AP test. Now that we have some sense of the size of the cosmological distortion and the size of the redshift distortions, we measure the cross spectrum from a small data sample.

⁹The isotropic and anisotropic models are each normalized to have the same $\langle f \rangle$. The two models hence have different A s, where A is the proportionality constant in the relation between optical depth and density.

Table 4.1. Pairs for Cross-Correlation Analysis

QSO Pair	z_1, z_2	$\lambda_{\text{low}}(\text{\AA}) - \lambda_{\text{high}}(\text{\AA})$	$\bar{z}_{Ly\alpha}$	$\Delta\theta$ (arcsec)
Q2139-4504A/B	3.06, 3.25	4467.56 – 4811.62	2.82	33
Q2139-4433/34	3.22, 3.23	4456.54 – 5000.52	2.89	62
KP76/77	2.467, 2.521	3809.60 – 4108.31	2.26	147
KP76/78	2.467, 2.607	3809.60 – 4108.31	2.26	130
KP77/78	2.521, 2.607	3809.60 – 4108.31	2.26	180

Note. — A summary of the quasar pairs included in the cross-correlation analysis. The first column gives the names of the members of the QSO pair, the second column gives the redshifts of each member of the pair, the third column shows the wavelength range analyzed, the fourth column indicates the mean redshift of absorption in the Ly α forest, and the fifth column is the separation of the pair in arcseconds. The pair Q2139-4433/34 has a typical resolution of FWHM = 3.6 Å, the pair Q2139-4504A/B has a typical resolution of FWHM = 3.0 Å, and the KP triplet has a typical resolution of FWHM = 2.79 Å.

4.5 Measurements of the Cross Power Spectrum from a sample of Close Quasar Pairs

In this section we present both a measurement of the cross spectrum from our data, and present constraints obtained from comparison with a small grid of simulated models. In Table (4.1) we provide a summary of pertinent information for the quasar pairs that we analyze. Observations were performed with the 4-meter/RC spectrograph combination at both Kitt Peak National Observatory and Cerro Tololo Inter-

american Observatory, using the T2KB CCD detector and grating BL420 in 2nd order, and the Loral 3K CCD and KPGL1 grating (1st order), respectively, delivering $3150\text{\AA} \lesssim \lambda \lesssim 4720\text{\AA}$ and $3575\text{\AA} \lesssim \lambda \lesssim 6675\text{\AA}$ for the KP triplet and 2139-44/45 pairs, respectively. Further details of these (and redder observations for the KP triplet, plus further spectra for additional objects) are detailed in Crotts & Bechtold (in preparation).

In order to estimate the cross spectrum of a given quasar pair the following procedure is followed:

- We extract the region of the Ly α forest that is common to each member of a quasar pair, avoiding regions close to each quasar that might be contaminated by the proximity effect. (Bajtlik et al. 1988) We make a conservative cut for the proximity effect, including only the region in the Ly α forest corresponding to rest frame wavelengths of $\lambda_{\text{rest}} \sim 1051\text{\AA} - 1185\text{\AA}$. We then discard regions that do not overlap in wavelength between each member of a given pair. In the case of the KP triplet, we discard regions that do not overlap across the entire triplet.

We have not made any attempt to remove metal absorption lines in the Ly α forest. The effect of metal lines on the flux power spectrum is expected to be small, except on scales smaller than the resolution of our present data (McDonald et al. 2000).

- We determine the flux field, $\delta_f = (f - \langle f \rangle)/\langle f \rangle$, for each member of a quasar pair. Here f is the flux at a given pixel and $\langle f \rangle$ is the mean flux. To do this we follow the procedure of Croft et al. (2002). We smooth the entire spectrum with a large radius, 50 Å, Gaussian filter giving the smoothed number of counts, $f_s(\lambda)$, as a function of wavelength. From the smoothed spectrum, δ_f is given by $\delta_f = (f(\lambda) - f_s(\lambda))/f_s(\lambda)$. This procedure estimates the mean flux directly, avoiding a measurement of the unabsorbed continuum level. Clearly, however, this procedure does not allow one to reliably measure the flux power on scales

$r \gtrsim 50$ Å, but the flux power on these scales is expected to be contaminated by continuum fluctuations anyway (Zaldarriaga et al., 2001b). We confine ourselves to measurements of cross power on scales of $k_{\parallel} \gtrsim 2.0 \times 10^{-3}$ s/km.

- We estimate the cross spectrum from the following estimator, utilizing 1d FFTs:

$$\hat{P}_{\times}(k_{\parallel}, \Delta\theta) = \frac{1}{n_k} \sum_{i=1}^{n_k} \frac{1}{2} [\delta_a(k_i)\delta_b^*(k_i) + \delta_b(k_i)\delta_a^*(k_i)] \quad (4.5)$$

Here the sum is over the n_k modes in a given k-bin, k_i is the ith mode in the bin, and k_{\parallel} is the average wave number in the bin. Our convention is that modes with $|k_i|$ and $-|k_i|$ fall within the same k-bin and that k_{\parallel} is always positive, so that $|k_i|$ and $-|k_i|$ count as two modes towards n_k . The Fourier amplitude $\delta_a(k_i)$ comes from the Fourier transform of the flux field of the first spectrum in the pair, $\delta_b(k_i)$ from the Fourier transform of the second spectrum in the pair and δ_a^* , δ_b^* are their complex conjugates. The cross spectrum is thereby a real quantity that contains information about the relative phase of the Fourier coefficients, $\delta_a(k_i)$, $\delta_b(k_i)$, as well as their amplitude.

- An estimate of the error on the cross spectrum measurements is made assuming Gaussian statistics, a procedure which seems to be supported on relevant scales by analyses from a large number of spectra from the SDSS (Hui et al., in preparation). With this assumption the error on the cross-spectrum estimate is (see Hui et al. 2001 for a derivation of the auto-spectrum variance)

$$\sigma_{\hat{P}}^2(k_{\parallel}) = \frac{1}{n_k} \left[(P_{\times}(k_{\parallel}, \Delta\theta))^2 + (P_{1d}(k_{\parallel}) + b^a(k_{\parallel})) (P_{1d} + b^b(k_{\parallel})) \right] \quad (4.6)$$

Here $P_{1d}(k_{\parallel})$ and $P_{\times}(k_{\parallel}, \Delta\theta)$ refer to the *true auto and cross spectra* as opposed to the noisy estimates from the data, which we refer to as \hat{P}_{1d} and \hat{P}_{\times} . In the above equation $b^a(k_{\parallel})$ and $b^b(k_{\parallel})$ are estimates of the shot-noise in each spectrum.¹⁰ As in equation (4.5), k_{\parallel} refers to the average wavenumber in a

¹⁰The shot-noise is estimated from the quasar spectrum variance array as in Hui et al. (2001).

k -bin and n_k is the number of modes in the bin counted with the convention described previously. When using these equations to estimate the error on the cross spectrum, we use simulation measurements to provide the true auto spectrum, $P_{1d}(k_i)$ and the true cross spectrum, $P_x(k_i, \Delta\theta)$. The simulation measurements are made assuming a model for the IGM that fits the observed auto spectrum at the relevant redshift. For the purposes of computing the error, we assume an $\Omega_m = 0.3$, $\Omega_\Lambda = 0.7$ cosmology. For pairs with large separations, the cross spectrum contribution to the error is negligible. In practice we measure the cross power of spectra that are smoothed by the limited spectral resolution of the observations, and so we take $\sigma_{\hat{P}}(k_{\parallel}) \rightarrow \sigma_{\hat{P}}(k_{\parallel})W(k_{\parallel})$, where $W(k_{\parallel})$ describes the smoothing due to limited spectral resolution.

- In deriving a constraint on Ω_Λ from the KP triplet, we need to take into account that each pair is not independent of the other pairs. A given pairing of lines of sight from the triplet has a line of sight in common with every other pairing and so measurements of the cross spectrum at a given scale are correlated across the different pairs. To take this correlation into account, we consider the covariance between cross spectrum measurements from two pairs that have a line of sight in common. Assuming Gaussian statistics, and ignoring shot-noise which should be unimportant on the scales we probe reliably with the KP triplet, we find that the covariance is

$$\begin{aligned} \langle \delta P_x^{12}(k_{\parallel}, \Delta\theta) \delta P_x^{23}(k_{\parallel}, \Delta\theta') \rangle = \\ \frac{1}{n_k} [P_x^{12}(k_{\parallel}, \Delta\theta) P_x^{23}(k_{\parallel}, \Delta\theta') + P_{1d}(k_{\parallel}) P_x^{13}(k_{\parallel}, \Delta\theta'')] \end{aligned} \quad (4.7)$$

The lines of sight are labeled by 1, 2, and 3. We write down the expression for the covariance between cross spectrum estimates of pairs 12 and 23, so that line of sight 2 is the common line of sight to the two pairs, expressions for other pairings follow from swapping the super-scripts. In this equation $P_x^{12}(k_{\parallel}, \Delta\theta)$ is the cross spectrum of lines of sight 1 and 2, which are separated by an angle $\Delta\theta$, $P_x^{23}(k_{\parallel}, \Delta\theta')$ and $P_x^{13}(k_{\parallel}, \Delta\theta'')$ have similar meanings, $P_{1d}(k_{\parallel})$ is the auto

spectrum, and k_{\parallel} , n_k have the meanings described above.

In figure (4.6) we provide an example of our procedure for forming δ_f . The spectra of the members of the pair Q2139-33/34 are shown, as well as the result of smoothing them with a 50 Å filter. The flux fields, δ_f , are shown one on top of the other, with the above cuts for the proximity effect. One can visually discern a cross-correlation between the two spectra in this pair, which has a separation of 62''. We generate flux fields for the other pairs in a similar fashion.

We then compare our measurements with a grid of models, using the method of Zaldarriaga et al. (2001a,2003). In particular for each of the two high redshift pairs we generate models with $a = (0.11, 0.14, 0.19, 0.24)$, $n = (0.7, 0.8, 0.9, 1.0)$, $k_f = 35.0 \text{ h Mpc}^{-1}$, $T_0 = (200, 250, 300) \text{ (km/s)}^2$, $\alpha = (0.0, 0.2, 0.4, 0.6)$, $\langle f \rangle = (0.625, 0.666, 0.700)$ at $\langle z \rangle = 2.89$ and $\langle f \rangle = (0.650, 0.684, 0.725)$ at $\langle z \rangle = 2.82$, $\Omega_\Lambda = (0.0, 0.1, 0.2, 0.3, 0.4, 0.5, 0.6, 0.7, 0.8, 0.9, 1.0)$.¹¹ At $\langle z \rangle = 2.26$, our grid spans a different range of power spectrum normalizations, $a = (0.24, 0.27, 0.31)$ and mean transmissions, $\langle f \rangle = (0.750, 0.800, 0.850)$. In computing the likelihood of each model in the grid, as described in §4.3.1, we include a prior constraint on $\langle f \rangle$. This constraint is $\langle f \rangle = 0.666 \pm 0.033$ at $\langle z \rangle = 2.89$, $\langle f \rangle = 0.682 \pm 0.034$ at $\langle z \rangle = 2.82$, and $\langle f \rangle = 0.802 \pm 0.040$ at $\langle z \rangle = 2.26$. The values of $\langle f \rangle$ come from the measurements of Press et al. (1993). In comparing the theoretical predictions with the observed auto spectrum, since we compare with only one simulation realization, we do not include points with $k \lesssim 2 \times k_{\text{fun}}$ where k_{fun} is the fundamental mode of the simulation box (see Appendix A). We do include such points in our cross spectrum analysis because the observational error bars on these points are very large and our results are not very sensitive to whether we include these points or not.

For each model in our grid, we then compute $\chi_{\text{tot}}^2 = \chi_{\text{auto}}^2 + \chi_{\text{cross}}^2$. The computation of χ_{auto}^2 , the goodness of fit of the model auto spectrum to the observed auto

¹¹Our treatment of redshift distortions for the high Ω_Λ models is probably inaccurate, since for these models $f(z \sim 3) \sim \Omega_m(z \sim 3)^{0.6} \neq 1$. For instance, if $\Omega_\Lambda = 0.9$ then $f(z = 2.26) = 0.87$. Given the size of our other uncertainties, we defer a more careful treatment to the future.

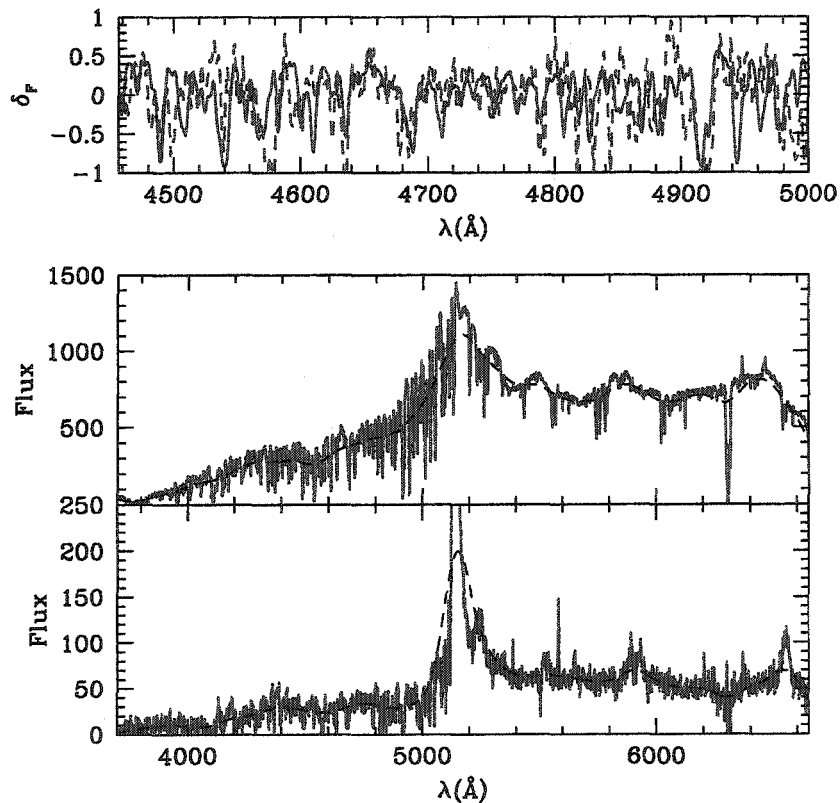


Figure 4.6 The bottom panel shows the spectrum of Q2139-4433 (solid line) and the middle panel shows the spectrum of Q2139-4434 (solid line). The dashed lines show the spectra when smoothed with a Gaussian filter of 50 Å radius in order to form δ_F (see text). The top panel shows δ_F overlayed for each spectrum. The solid line is δ_F for Q2139-4433 and the dashed line is Q2139-4434. The pair is separated by $\Delta\theta = 62''$.

spectrum of Croft et al. (2002) interpolated to the relevant redshift, is described in §4.3.1. To compute χ^2_{cross} we take the sum $\chi^2_{\text{cross}} = \sum_{i=1}^n \left[\frac{(\tilde{P}_{x,\text{sim}}(k_i, \Delta\theta) - P_{x,\text{obs}}(k_i, \Delta\theta))^2}{\sigma_i^2} \right]$. Here $P_{x,\text{obs}}(k_i, \Delta\theta)$ is the observed cross spectrum measurement at wavenumber k_i and transverse separation $\Delta\theta$, $\tilde{P}_{x,\text{sim}}(k_i, \Delta\theta)$ is the simulation measurement linearly interpolated to the same k_i and $\Delta\theta$, and smoothed to mimic the limited spectral resolution of our cross spectrum measurement.¹² The error estimates of 4.6 and 4.7 are multiplied by the smoothing window before calculating χ^2 . The spectral resolution of each spectrum is shown in Table (4.1). We truncate the sum at k_n , the scale at which the limited spectral resolution causes the measured cross power to drop to 50% of the value it would have with perfect resolution. From the values of χ^2_{tot} at each point in the parameter grid we determine marginalized constraints on Ω_Λ following the method of Tegmark & Zaldarriaga (2000), Zaldarriaga et al. (2001a,2003).

In brief, the method of Tegmark & Zaldarriaga (2000) is as follows. We begin from a grid of χ^2 points in a seven-dimensional parameter grid. We wish to find constraints on Ω_Λ , marginalized over all of the other “nuisance” parameters in the grid. To do this one should integrate over the “nuisance” parameters. Here we avoid the full multidimensional integration by assuming that the likelihood function is multi-variate Gaussian, in which case integrating out a parameter is equivalent to maximizing the likelihood over the parameter (Tegmark & Zaldarriaga 2000). We then maximize over each parameter in turn, first cubic spline-interpolating over the parameter. In this way we obtain marginalized constraints on Ω_Λ .

The cross spectrum measurements from the two high redshift pairs are shown in the top two panels of figure (4.7). From the figure one sees that the signal is generally weakly detected on large scales where few modes are available. On these scales some of the measurements in different k bins are consistent with zero at the 1σ level. A more significant signal is detected on small scales where more modes are available. Before comparing these cross spectrum measurements with models from the simulation grid,

¹²For the KP triplet, we use the full covariance matrix in calculating χ^2_{cross} , the off diagonal elements of which are calculated using equation (4.7).

it is useful to measure the cross spectrum from the overlapping regions in the Ly α forests of a widely separated quasar pair. If our underlying assumption that the cross spectrum signal arises from fluctuations in the underlying density field is correct, the cross spectrum of widely separated pairs should be consistent with zero. In the bottom panel of figure (4.7) we show a measurement of the cross spectrum between the spectra of Q2139-4504A/4433. Over the range of scales that we use here for our constraints, the cross spectrum of the widely separated pair is consistent with zero. Quantitatively, we find that χ^2 for the measurement, compared with the null hypothesis of $P_x(k_{\parallel}, \Delta\theta = \infty) = 0.0$, is 5.0 for 7 degrees of freedom.

We then compare the measured cross spectra with fits from the simulation grid. For the pair Q2139-4433/34, at separation $\Delta\theta = 62''$ and $\langle z \rangle = 2.89$, we find that the cross spectrum measurements are fit reasonably well by models from the simulation grid. In particular the minimum χ^2 is $\chi_{\text{tot}}^2 \sim 11.2$ obtained near $\Omega_\Lambda = 0.9$. This is a reasonable fit to the 16 data points considered, (9 auto spectrum points and 7 cross spectrum points), given that our model has roughly 5 free parameters. Each of the auto and cross spectrum are well fit by the model; a model at a nearby grid point in the parameter space has $\chi_{\text{auto}}^2 \sim 5.7$. To gauge the difference between models with different Ω_Λ we show models in figure (4.7) with $\Omega_\Lambda = 0.9$ and $\Omega_\Lambda = 0.0$ that are close to the interpolated best fit parameters. We emphasize that χ^2 is spline interpolated between grid points and so the minimum value of χ^2 does not, in general, lie on a grid point in the parameter space. We include the plots of the model cross spectra just to provide some visual comparison between the data and the model fits. The cross spectrum measurement of the pair Q2139-4504A/B is not as well fit by the models in the parameter grid. The best fit model in the grid has $\chi_{\text{tot}}^2 = 15.8$ obtained at $\Omega_\Lambda = 1.0$. The fit is to 18 data points (9 auto spectrum points and 9 cross spectrum points), with roughly 5 free parameters. The auto spectrum is very well fit for these models with nearby grid points having $\chi_{\text{auto}}^2 \sim 3.5$. The poor χ_{cross}^2 for this pair is somewhat surprising. We searched the spectra for contaminating metal line absorbers and for artifacts, but found no effects in the wavelength range we analyze. Another

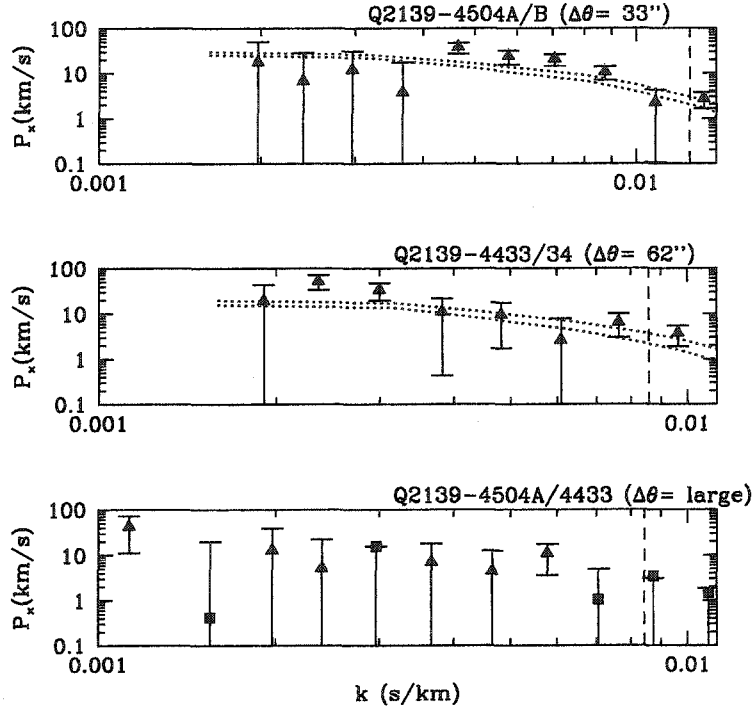


Figure 4.7 The top panel shows the cross spectrum measured from the pair Q2139-4504A/B. We also show models from our grid that are close to the best fit flat universe models with $\Omega_\Lambda = 0.9$ (top curve) and $\Omega_\Lambda = 0.0$ (bottom curve). The other IGM parameters are the same for both models, $(a, n, k_f, T_0, \langle f \rangle, \alpha) = (0.19, 0.8, 35, 200, 0.684, 0.4)$. The middle panel shows the same for the pair Q2139-4433/34. In this case, the IGM parameters are $(a, n, k_f, T_0, \langle f \rangle, \alpha) = (0.14, 0.9, 35, 250, 0.666, 0.0)$. The dashed line indicates the cut we make on the data due to the limited spectral resolution; only points to the left of the dashed line are included in our fit. The bottom panel shows the cross spectrum of a widely separated pair, which is consistent with zero. The diamonds indicate points with a positive cross spectrum and the squares indicate the absolute value of points with a negative cross spectrum.

possible issue is that we need to estimate our resolution window carefully, since we have included scales where the power is suppressed by the resolution by $\lesssim 50\%$. We made a careful estimate by looking at the widths of narrow metal lines and night sky lines. For now we consider the poor fit for Q2139-4504A/B to be a curiosity, but point out that larger data samples in the future will allow us to test more carefully for systematic effects.

In figure (4.8) we show the measurements obtained from the KP triplet. In this case the cross spectrum signal of the pairs, with $\langle z \rangle \sim 2.26$ and separations in the range of $\Delta\theta \sim 2' - 3'$, is only weakly detected. For the two larger separation pairs most of the measurements of the cross spectrum at different scales are consistent with zero. In spite of this, we still obtain a weak constraint on Ω_Λ from the KP triplet, taking into account the covariance between the cross spectrum estimates of the three pairs. The best fit model is obtained near $\Omega_\Lambda \sim 0.85$, where $\chi^2_{\text{tot}} = 24.6$. This is a reasonable fit given that there are 21 cross spectrum points and 9 auto spectrum points, and roughly 5 free parameters for a total of 25 degrees of freedom. We then combine the marginalized constraints on Ω_Λ by adding the χ^2_{tot} curve from the KP triplet with the constraints from Q2139-4433/34 and Q2139-4504A/B. Given that the cross spectrum of the pair Q2139-4504A/B is somewhat poorly fit by the models in the simulation grid, we also consider the combined constraint ignoring this pair. Including Q2139-4504A/B, the minimum total χ^2 for the five pairs is $\chi^2_{\text{tot}} \sim 52.5$, (for ~ 59 degrees of freedom), obtained near $\Omega_\Lambda \sim 0.9$. If we don't include the poorly fit pair, the total χ^2 is $\chi^2_{\text{tot}} \sim 36.1$ for the combined measurement, (for ~ 41 degrees of freedom) which occurs near $\Omega_\Lambda \sim 0.9$. The result, shown in figure (4.9), is that, if we include Q2139-4504A/B, $\Delta\chi^2 = \chi^2 - \chi^2_{\text{min}}$ is ~ 5.1 for a flat model with $\Omega_\Lambda = 0$, implying such a cosmology is excluded at the $\sim 2.3\sigma$ level.¹³ Ignoring the poorly fit pair, $\Delta\chi^2$ reaches ~ 2.3 for $\Omega_\Lambda = 0$. Our small sample of pairs seems to

¹³When we quote significances, we take a 2σ limit to be where $\Delta\chi^2 = 4$, or where the likelihood has fallen by a factor of e^{-2} from its maximum value. Strictly speaking, this corresponds to a 95% confidence limit only when the likelihood is multivariate Gaussian, which is assumed in the way we perform the marginalization. (See Tegmark & Zaldarriaga 2000).

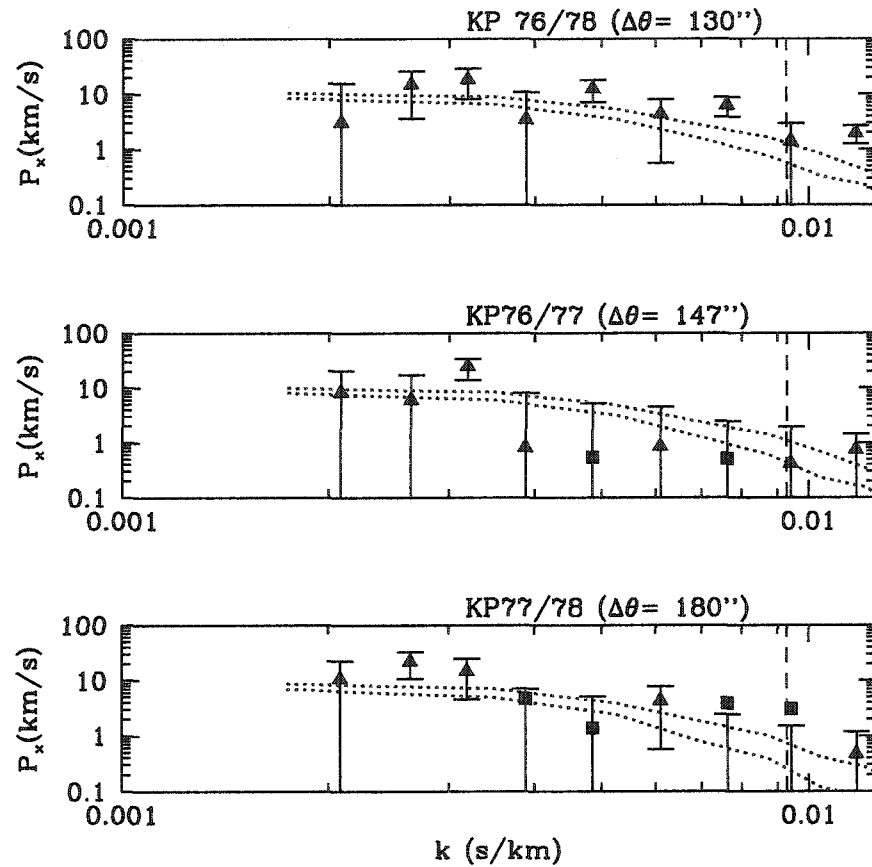


Figure 4.8 The panels show measurements of the cross spectrum from the KP triplet pairs, as well as models from the simulation grid with $\Omega_\Lambda = 0.9$ and $\Omega_\Lambda = 0.0$ to provide some comparison between the data and model fits. The models have $(a, n, k_f, T_0, \langle f \rangle, \alpha) = (0.24, 0.9, 35, 250, 0.800, 0.6)$. The diamonds indicate points with a positive cross spectrum and the squares indicate the absolute value of points with a negative cross spectrum. In examining this figure, one should keep in mind that the measurements of the cross spectrum at a given scale are correlated across the different pairs, as discussed in the text.

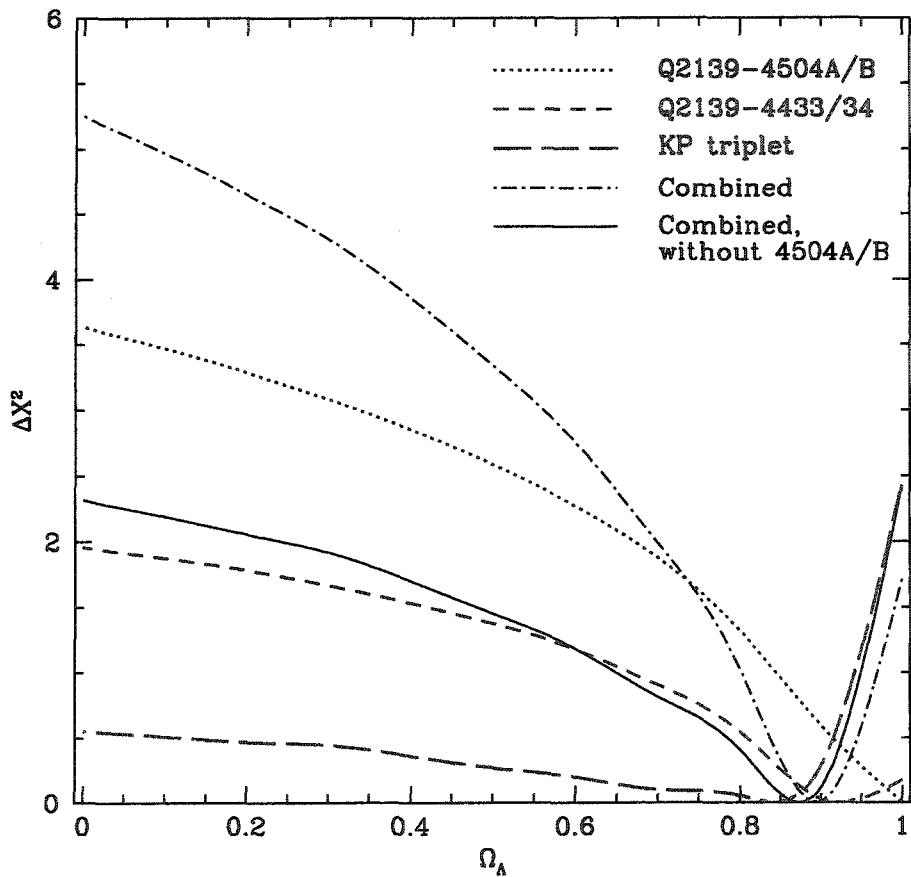


Figure 4.9 The constraint on Ω_Λ from the quasar pairs. The dotted line shows $\Delta\chi^2 = \chi^2 - \chi_{\min}^2$ from the pair Q2139-4504A/B. The short-dashed line shows the constraint from the pair Q2139-4433 and the long-dashed line shows the constraint from the KP triplet. The dot-dashed line is the combined constraint. The solid line shows the constraint obtained ignoring Q2139-4504A/B, since the cross spectrum of this pair is somewhat poorly fit by the models in our simulation grid.

already disfavor an EDS cosmology at a significance of $\sim 1.5\sigma$, or at an even larger significance if one includes the constraint from the poorly fit pair. There is a weak preference from each pair for a high value of Ω_Λ ; models with moderate $\Omega_\Lambda \sim 0.6$ are similarly disfavored at the $\gtrsim 1\sigma$ level. Admittedly, even ignoring the poorly fit pair, some our ability to rule out an EDS cosmology comes from just two k -bins in the pair Q2139-33/34 with particularly large cross power (see figure 4.7). While we have no reason to believe the measurements in these k -bins are unreliable, we can check how much the significance depends on them. Ignoring these two k -bins, we find that an EDS cosmology is still disfavored at the 1σ level.

4.6 Predictions for Future Samples/Observational Strategies

Clearly it is not possible to draw any strong conclusions with the limited sample of five pairs analyzed above. This motivates considering the type of sample necessary to do better in the future. In this section we make predictions for the signal-to noise level (S/N) at which one can distinguish between two different cosmologies with a given number of quasar pairs, and examine the dependence of the expected S/N level on observational resolution and shot noise. We hope that these considerations will be useful in constructing an optimal observing strategy. This is similar to estimates considered in (Hui, Stebbins & Burles 1999), but here we use more accurate expressions for the cross spectrum; our estimates coming from simulations that include the effects of redshift distortions and the detailed form of the three-dimensional flux power spectrum. These authors also limited their considerations to large scales, ($k \lesssim 0.02$ s/km), because of concerns about non-linear effects. We model the non-linear effects with simulations and so can consider the benefit gained from high k modes, which can be quite substantial given close separation pairs and high resolution data. In addition, we consider the effects of instrumental resolution and shot-noise. McDonald (2003) has also made this type of comparison, primarily considering the expected

signal from pairs obtained with the SDSS. While our results are broadly consistent with his, we emphasize the potential gain from very close separation pairs observed with high spectral resolution.

The expected signal to noise level at which one can distinguish between two cosmologies with the Ly α AP test is:

$$\frac{S}{N} \sim \left[\frac{fL}{\pi} \int_{k_{\parallel}=k_{\min}}^{k_{\parallel}=k_{\max}} dk_{\parallel} \left[\frac{P_x^A(k_{\parallel}, \Delta\theta) - P_x^B(k_{\parallel}, \Delta\theta)}{\sqrt{(P_{1d}(k_{\parallel}) + b(k_{\parallel}))^2 + (P_x^A(k_{\parallel}, \Delta\theta))^2}} \right]^2 \right]^{1/2} \quad (4.8)$$

In this equation $P_x^A(k_{\parallel}, \Delta\theta)$ is the assumed true cross spectrum, and $P_x^B(k_{\parallel}, \Delta\theta)$ is the cross spectrum in a model we would like to rule out. The denominator is the Gaussian error estimate on the variance of the cross spectrum given in equation (4.6) for a single k -mode.¹⁴ We caution that the Gaussian error estimate is likely to be inaccurate on small scales, but leave a more careful treatment of errors for future work. The integral is over all positive k -modes, from the lower limit of k_{\min} to the upper limit of k_{\max} , with a density of states factor of L/π . For the length of the spectrum we take $L \sim 37,500$ km/s.¹⁵ The factor f is the fraction of the wavelength coverage between Ly α and Ly β that is overlapping between the two spectra in the pair, which we take to be $f = 1$. The minimum wavenumber in the integral, k_{\min} is taken to be $k_{\min} = 2.0 \times 10^{-3}$ s/km since larger scales are expected to be contaminated by fluctuations in the continuum. The maximum wavenumber in the sum is set by the spectral resolution of the observation; it is taken to be the wavenumber where the measured power falls to $1/e$ of its true value. Modeling the effect of spectral resolution as a Gaussian smoothing, this wavenumber is given by $k_{\max} = \frac{1}{\sigma_s}$, where σ_s is related to the instrumental FWHM by $\sigma_s = \frac{FWHM}{2\sqrt{2\ln(2)}}$. In considering high spectral resolution data, we enforce an upper limit of $k_{\max} = 0.1$ s/km, since the Ly α forest

¹⁴For the shot-noise we assume $b(k_{\parallel}) \sim 1.0$ km/s. Below we consider the effect of different assumptions about the shot-noise.

¹⁵This is about 12,500 km/s shorter than the distance between Ly α and Ly β at our fiducial redshift of $\langle z \rangle = 2.82$. This corresponds to a cut of about 25 Å in the rest frame near each of Ly α and Ly β .

is expected to be contaminated by metal lines on such scales (McDonald et al. 2000). One caveat is that in estimating our ability to discriminate between models in this way, we assume perfect knowledge of the other parameters that go into our modeling; the power spectrum normalization, the primordial spectral index, the temperature of the IGM, etc. Measurements of the auto spectrum from SDSS should dramatically reduce the error bars on the observed auto spectrum, and make the associated errors in our modeling parameters smaller. Uncertainties in these modeling parameters will, however, affect our ability to constrain Ω_Λ , so the constraints quoted below are optimistic. We would like to estimate our ability to discriminate between cosmological models using pairs with a range of separations. Unfortunately, as described in §(4.3.1), direct measurements of the cross spectrum at large separations from simulations are rather noisy. To get around this difficulty, we use a fitting formula that describes the fully three-dimensional flux power spectrum and reproduces the results of simulation measurements at small separations. This allows us to extrapolate cross spectrum measurements to large angular separations. In particular, at our fiducial redshift of $\langle z \rangle = 2.82$, we find the cross and auto spectra are well fit if the three-dimensional flux power spectrum follows the fitting form found by McDonald (2003), $P_F(k, \mu) = b_\delta^2(1 + \beta\mu^2)D(k, \mu)P_L(k)$, with $D(k, \mu) = \exp\left[\left(\frac{k}{k_{NL}}\right)^{\alpha_{NL}} - \left(\frac{k}{k_p}\right)^{\alpha_p} - \left(\frac{k_{\parallel}}{k_v(k)}\right)^{\alpha_v}\right]$ and $k_v(k) = k_{v0}(1 + k/k'_v)^{\alpha'_v}$. Here $P_L(k)$ is the linear power spectrum of mass and $D(k, \mu)$ describes the effect of non-linear redshift distortions. The first term in $D(k, \mu)$ describes non-linear growth, the second term pressure smoothing, and the third term describes the effect of non-linear peculiar velocities and thermal broadening. The first two terms describe isotropic effects, while the third term has a μ dependence since thermal broadening and peculiar velocities act only along the line of sight. Given this fitting formula we predict auto and cross spectra by numerical integration using equations (4.2) and (4.3). At our fiducial redshift of $\langle z \rangle = 2.82$ the cross and auto spectra are fit using the fitting parameters $b_\delta^2 = 0.04$, $\beta = 0.62$, $k_{NL} = 10.0 \text{ h Mpc}^{-1}$, $\alpha_{NL} = 0.550$, $k_p = 14.0 \text{ h Mpc}^{-1}$, $\alpha_p = 2.12$, $k_{v0} = 5.50 \text{ h Mpc}^{-1}$, $\alpha_v = 1.25$, $k'_v = 0.917 \text{ h Mpc}^{-1}$, and $\alpha'_v = 0.528$. These parameters are different than the ones

found by McDonald (2003), but he considers a lower redshift, $z = 2.25$, and uses a different linear power spectrum model. In figure (4.10) we show the fits to the auto and cross spectra from simulation measurements. The model fit to the auto spectrum is reasonable. The plot also shows fits at separations of $\Delta\theta = 33''$ and $\Delta\theta = 60''$ for both EDS and Lambda cosmologies, which are reasonable. We also checked that the fitting formula provides reasonable fits at $\Delta\theta = 90''$ in these cosmologies. With the fitting formula in hand we then make predictions of the cross spectrum at large separations using equation (4.3). We then calculate our expected ability to discriminate between cosmologies using equation (4.8).

In figure (4.11) we show the results of this calculation, in this case considering the difference between an $\Omega_m = 1.0$ (EDS) cosmology and a $\Omega_m = 0.3, \Omega_\Lambda = 0.7$ (Lambda) cosmology. For a single pair with $\Delta\theta = 30''$, at high observational resolution, one can already distinguish between the two models at $S/N \sim 1.6\sigma$. Still considering high observational resolution, we see that at larger separation, as the cross spectrum signal weakens, the S/N level goes down, reaching $S/N \sim 0.9\sigma$ at $\Delta\theta = 60''$ and $S/N \sim 0.35\sigma$ at $\Delta\theta = 180''$. At still larger separations, the discriminating power is quite weak, reaching $S/N \sim 0.2\sigma$ at $\Delta\theta = 300''$ and $S/N < 0.1$ at $\Delta\theta = 600''$.¹⁶

At lower observational resolution the advantage of measuring the cross spectrum for close separation pairs is lost. When the FWHM becomes slightly worse than ~ 150 km/s, the S/N level, at $S/N \sim 0.7\sigma$, is comparable for measuring the cross spectrum from a pair at separation $\Delta\theta = 30''$ and for using a pair at separation $\Delta\theta = 60''$. In order to obtain the increased discriminating power of small separation pairs, one must be able to resolve the high k modes. At increased angular separation, however, observational resolution makes very little difference. At these separations the cross spectrum (see eq. 4.3) turns over at relatively low k_{\parallel} , and so, regardless of resolution, the high k modes contribute insignificantly to the S/N level. This explains why the S/N curves at large angular separation in figure (4.11) are flat as a function of observational resolution. The conclusion is that *there is an advantage to hunting*

¹⁶For separations a bit smaller than $\Delta\theta = 30''$ the discriminating power drops off.

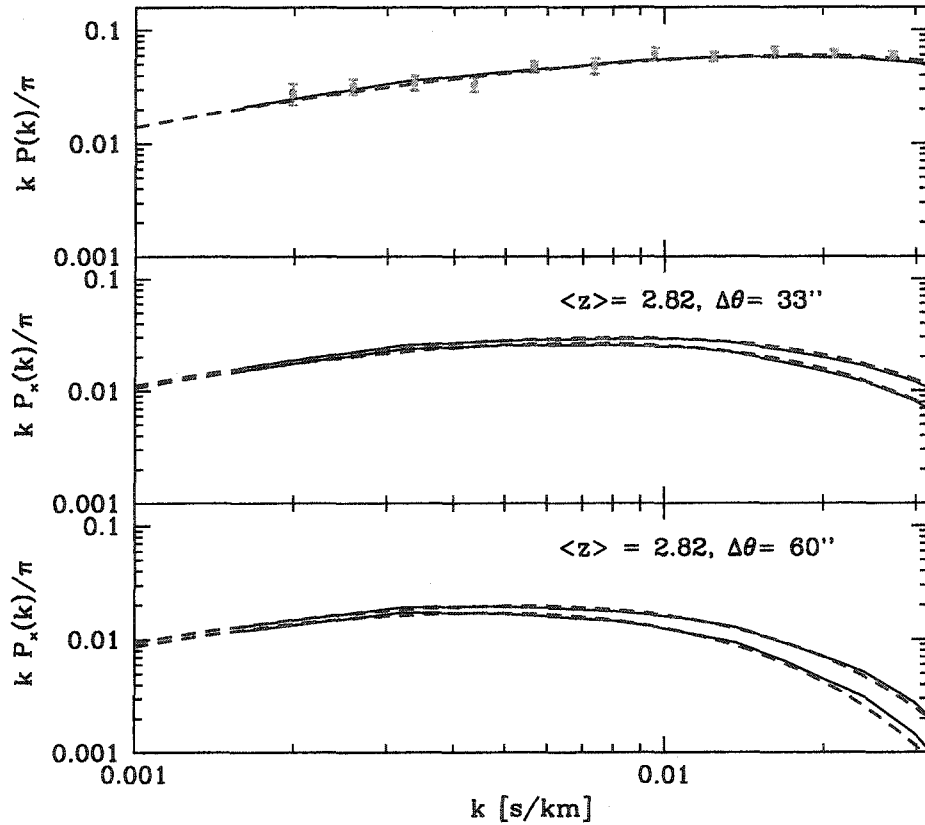


Figure 4.10 The top panel shows Croft's measured auto spectrum, interpolated to $\langle z \rangle = 2.82$ (points with error bars), a fit to this with the fitting formula of §4.6 (dashed line), and a measurement from simulations (solid line). The middle panel shows a fit to the cross spectrum at separation $\Delta\theta = 33''$ (dashed line), and the simulation measurement at the same separation (solid line). The top solid curve in the panel and its dashed fit are for a $\Omega_m = 0.3$, $\Omega_\lambda = 0.7$ (Lambda) cosmology, and the bottom curves for a $\Omega_m = 1.0$ flat (EDS) cosmology. The bottom panel is similar to the middle panel, but here we consider pairs separated by $\Delta\theta = 60''$.

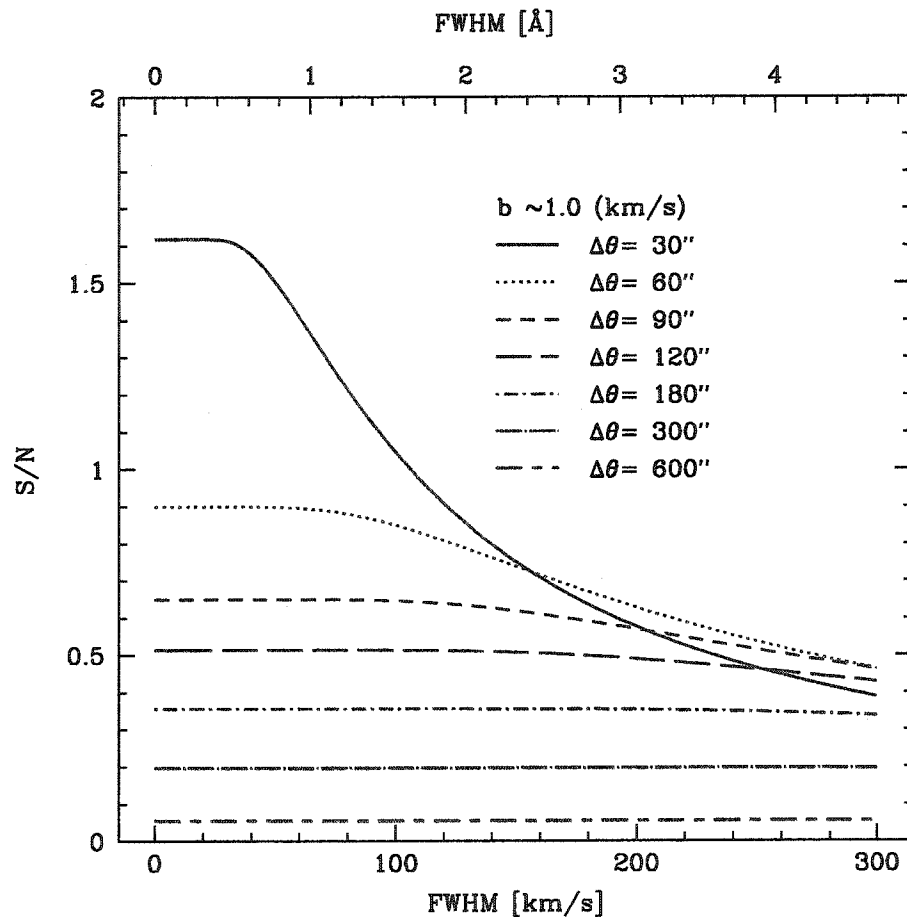


Figure 4.11 The expected signal to noise level (S/N) at which one can distinguish between an $\Omega_m = 0.3, \Omega_\Lambda = 0.7$ cosmology and a $\Omega_m = 1.0$ cosmology from a single quasar pair as a function of resolution (FWHM). The effect of shot noise is included, with shot noise at the level of $b \sim 1.0 \text{ km/s}$. We assume perfect knowledge of all of the other parameters involved in modeling the IGM.

out close separation pairs, but only if the observational resolution is sufficiently good. Below we give a rough formula to determine what spectral resolution is good for observing pairs of a given separation.

Figure (4.11) illustrates the possibilities of distinguishing between an EDS cosmology and a Lambda cosmology, but it is more interesting to consider the discriminating power between two more realistic cosmologies. In figure (4.12) we show the ability of the Ly α AP test to discriminate between a $\Omega_m = 0.3, \Omega_\Lambda = 0.7$ cosmology and a $\Omega_m = 0.2, \Omega_\Lambda = 0.8$ cosmology (left panel) as well as the ability to discriminate between two quintessence cosmologies (right panel). At high observational resolution, using a single pair with separation $\Delta\theta = 30''$, one can expect to distinguish between the two Lambda cosmologies at a level of $S/N \sim 0.7$. With a pair at $\Delta\theta = 60''$ the discriminating power falls off to $S/N \sim 0.4$ and then to $S/N \lesssim 0.2$ at $\Delta\theta = 180''$ and $S/N \lesssim 0.1$ at $\Delta\theta = 300''$. At the moderate resolution of $\text{FWHM} \sim 150 \text{ km/s}$, where the discriminating power is typically $S/N \sim 0.3$ for close separation pairs (with $\Delta\theta \sim 30 - 120''$), one needs ~ 200 pairs to distinguish between these models at the 4σ level. Alternatively, one could achieve the same discriminating power with only ~ 35 close separation ($\Delta\theta \sim 30''$), high resolution, pairs. We can provide a rough criterion for determining the spectral resolution that will be good for observing pairs at a given separation. We adopt the rule that the spectral resolution, FWHM, should be sufficiently good that the discriminating power drops off by no more than a factor of 0.7 from its value at optimal resolution. Adopting this criterion for the case of discriminating between the two Lambda cosmologies, *we find that the FWHM should be less than than $80(\Delta\theta/30'')^{1.1} \text{ km/s}$ for pairs with separations between $\Delta\theta = 30'' - 100''$ and that the spectral resolution is pretty irrelevant for larger separation pairs.* At separations between $\Delta\theta = 30'' - 600''$, we find that the following fitting formula describes the expected discriminating power for a pair with a given separation and

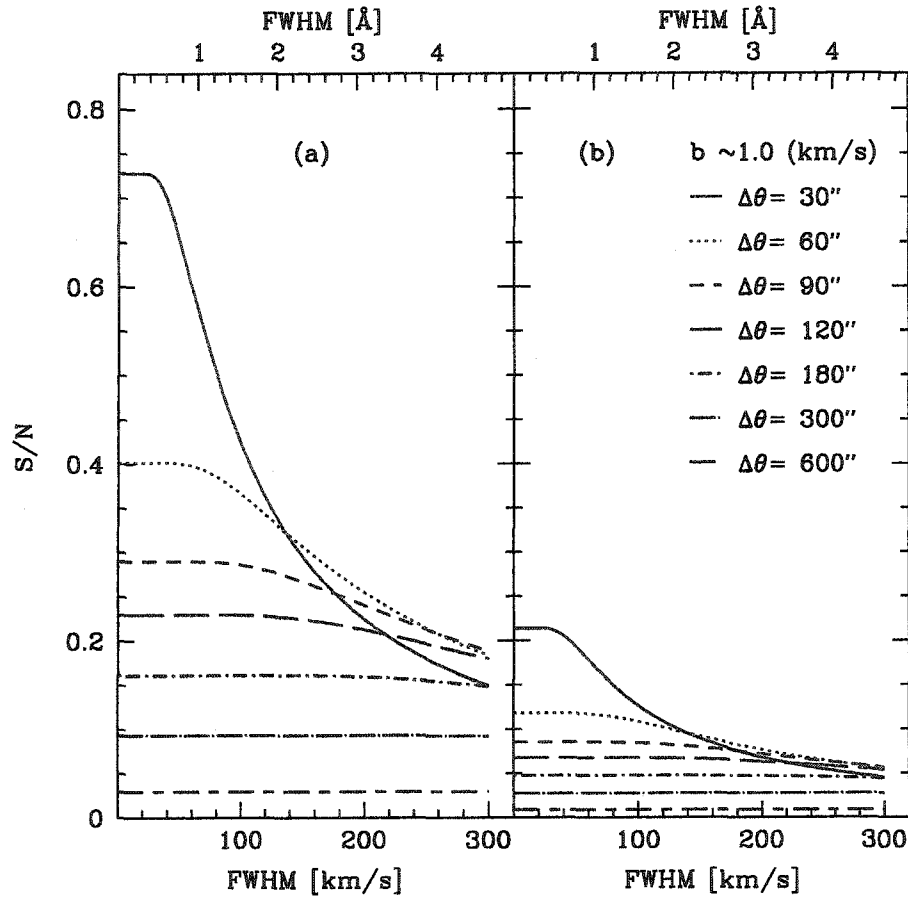


Figure 4.12 a) The same as figure (4.11) except this plot shows the S/N level at which one can distinguish between a $\Omega_m = 0.3, \Omega_\Lambda = 0.7$ cosmology and a $\Omega_m = 0.2, \Omega_\Lambda = 0.8$ cosmology from a single quasar pair. b) The S/N level at which one can distinguish between two quintessence cosmologies from a single quasar pair. Both cosmologies have $\Omega_m = 0.3$ and $\Omega_Q = 0.7$. The models have equations of state $w = -1$ and $w = -0.7$. The equation of state is assumed constant with redshift. In both a) and b), we assume perfect knowledge of all of the other parameters involved in modeling the IGM. It should be stressed that these comparisons are at $z \sim 3$. At sufficiently lower or higher redshifts, the AP test should have an increased sensitivity to w .

FWHM to better than 10%:

$$\frac{S}{N}(\theta, FWHM) \sim \frac{0.727 \left(\frac{30''}{\theta}\right)^{0.83} - 0.015 \left(\frac{300''}{\theta}\right)^{-1.1}}{1 - \left(0.7 \frac{30''}{\theta} \frac{FWHM}{300km/s}\right) + \left(3.0 \frac{30''}{\theta} \frac{FWHM}{300km/s}\right)^2 - \left(1.6 \frac{30''}{\theta} \frac{FWHM}{300km/s}\right)^3} \quad (4.9)$$

In the right hand panel of figure (4.11), we show the ability of the Ly α AP test to discriminate between a quintessence cosmology with equation of state $w = -1$ and a cosmology with $w = -0.7$. Here the pressure of the quintessence component is $p = w\rho_Q$, where ρ_Q is the energy density of the quintessence component, and we assume that the equation of state is constant with redshift so that $\rho_Q = \Omega_Q(1+z)^{3(1+w)}$. As mentioned in §4.2, and illustrated in figure (4.1), the Ly α forest AP test is barely sensitive to w , at $z \sim 3$. We will be making a small error here in the predicted signal for $w = -0.7$, because the redshift distortions in this cosmology should be slightly different than in the $w = -1$ cosmology. We find that, indeed, even with high observational resolution, the discriminating power is only $S/N \sim 0.2$ for a single pair separated by $\Delta\theta = 30''$. Discriminating between two quintessence models with the Ly α forest AP test would require an extremely large number of close separation pairs. The Ly α forest AP test may, however, be helpful for attempts to constrain quintessence models by helping to tighten constraints on Ω_m , as mentioned in §4.2, and emphasized by McDonald (2003). Alternatively, applying the forest AP test to lower or higher redshifts might be a more promising way of constraining w (see figure 4.1).

It is also instructive to consider the effect of shot-noise on our ability to discriminate between cosmologies. Since the noise fluctuations in each line of sight are independent, the noise has no cross-correlation and shot-noise does not directly contribute to our estimator for the cross spectrum. However, shot noise does contribute to the variance of our estimate for the cross spectrum. Here we estimate the shot noise level, at some typical signal to noise level per pixel, $(s/n)_{pix}$, using an approximate formula from Hui et al (2001). If the typical signal to noise level per pixel at the continuum is $(s/n)_{pix}$, the pixel separation Δu , and the mean transmission

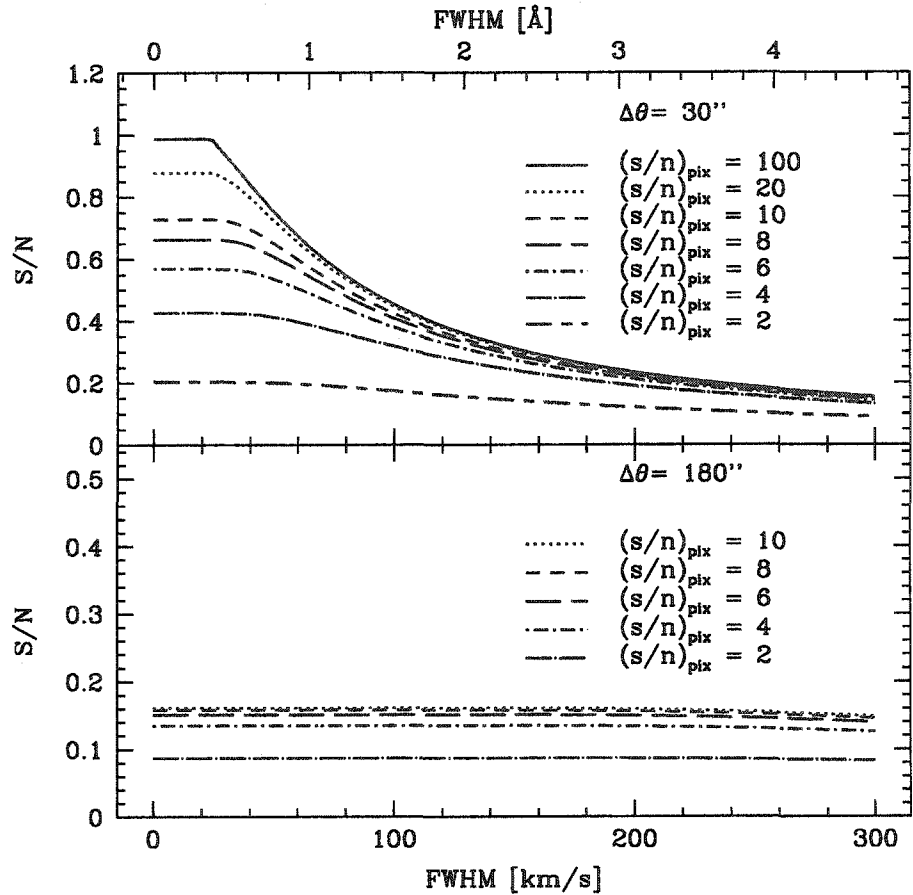


Figure 4.13 The plot shows the effects of shot noise on the S/N level at which one can distinguish between a flat $\Omega_\Lambda = 0.7$ cosmology and a flat $\Omega_\Lambda = 0.8$ cosmology. The top panel is for a single quasar pair separated by $\Delta\theta = 30.0''$ and the bottom panel for $\Delta\theta = 180.0''$. The different curves represent different assumptions about the typical signal to noise level per pixel, $(s/n)_{pix}$ in each quasar spectrum. In each case the signal to noise level refers to the level at the continuum for a pixel size of $\Delta u = 70$ km/s. The equivalent signal to noise level for a pixel of arbitrary size, Δu , is $(s/n)_{pix} \times \left(\frac{\Delta u}{70\text{km/s}}\right)^{1/2}$. We assume perfect knowledge of all of the other parameters involved in modeling the IGM.

$\langle f \rangle$, then the shot-noise bias is $b \sim \frac{\Delta u}{\langle f \rangle} ((s/n)_{\text{pix}})^{-2}$. For instance, in the above discussion we assumed $b \sim 1.0$ km/s, which for $\langle f \rangle = 0.684$, $\Delta u = 70$ km/s (~ 1 Å at $z \sim 2.82$), corresponds to a signal to noise per pixel of $(s/n)_{\text{pix}} \sim 10$. In figure (4.13) we show the expected discriminating power (between Lambda cosmologies with $\Omega_\Lambda = 0.7$ and 0.8) for $(s/n)_{\text{pix}} = 2, 4, 6, 8, 10, 20$ and 100, with $\Delta u = 70$ km/s, for a close separation pair separated by $\Delta\theta = 30''$. We also show the discriminating power for a moderate separation pair, with $\Delta\theta = 180''$, at shot noise levels corresponding to $(s/n)_{\text{pix}} = 2, 4, 6, 8, 10$. Given the plot we can ask how low a shot-noise level is required so that the expected discriminating power, from a pair with a given separation and spectral resolution, is degraded by no more than a factor of 0.7 from its optimal value. We will take this as a criterion for determining what $(s/n)_{\text{pix}}$ level is good for a pair at a given separation, observed with a given spectral resolution. For the pair separated by $\Delta\theta = 30''$, at high spectral resolution, the discriminating power is degraded by a factor of 0.7 when the signal to noise level reaches $(s/n)_{\text{pix}} \sim 10$. At lower spectral resolution, FWHM ~ 150 km/s, the discriminating power is reduced by the same factor only when the signal to noise level reaches $(s/n)_{\text{pix}} \sim 3 - 4$. For the pair separated by $\Delta\theta = 180''$, the spectral resolution is unimportant and the discriminating power is degraded by a factor of 0.7 when the signal to noise level reaches $(s/n)_{\text{pix}} \sim 3 - 4$. In general shot-noise is an issue only when its contribution to the cross spectrum error becomes comparable to the sample variance contribution. The two contributions to the variance become comparable roughly when $b \sim P_{1d}(k)$; if $b \sim 1$ km/s, (corresponding to $(s/n)_{\text{pix}} \sim 10$), the two are comparable near $k \sim 0.06$ s/km, at which scale the cross spectrum is very small unless the separation of the pair is also very small. With this level of shot-noise, the discriminating power will only be degraded for high-resolution, close separation pairs. If the shot-noise is sufficiently bad, however, the shot-noise contribution to the cross spectrum variance can become comparable to the sample variance contribution even on large scales. In this case, which occurs around $(s/n)_{\text{pix}} \sim 3 - 4$, the shot-noise will degrade the discriminating power even for large separation pairs, as illustrated in the lower panel of figure (4.13).

To summarize, for close separation pairs, with $\Delta\theta \sim 30''$, and high spectral resolution, given a pixel size of Δu , a signal to noise level of $(s/n)_{\text{pix}} \sim 10 \left(\frac{\Delta u}{70 \text{km/s}} \right)^{1/2}$ is recommended. In other cases, $(s/n)_{\text{pix}} \sim 4 \left(\frac{\Delta u}{70 \text{km/s}} \right)^{1/2}$ is generally adequate.

4.7 Conclusions

In this chapter we have described a concrete procedure for obtaining constraints on dark energy from a version of the Ly α AP test. We applied this procedure to a small sample of quasar pairs, and discussed the possibilities of future observations. Our main results are summarized as follows:

- While the Ly α AP test is a sensitive discriminator of a cosmological constant, it is not sensitive to the equation of state of a quintessence field unless $w(z \sim 3) \gtrsim -0.4$. (See also McDonald 2003.) The Ly α AP test is particularly sensitive to the presence of a large Ω_Λ .
- The effect of redshift distortions on the cross spectrum are important and must be taken into account in detail. At a redshift of $z = 2.82$ we measure the quadrupole to monopole ratio of the flux power spectrum and find that a linear theory prediction is close to correct on large scales. The ratio depends somewhat on $\langle f \rangle$. The lesson is that one needs simulations to account for redshift distortions accurately.
- We measured the cross spectrum from a sample of close quasar pairs. The cross spectrum measurements have large error bars due to the small number of pairs in the present sample. The measurements are generally consistent with the cross spectra from a grid of simulated models, if perhaps weakly favoring high Ω_Λ cosmologies, although one pair, Q2139-4504A/B, has somewhat excess small scale power. A comparison between models from the simulation grid and the cross spectra of Q2139-4433/34 and the KP triplet disfavors an EDS cosmology at a level of $\sim 1.5\sigma$. If we include the poorly fit pair, an EDS cosmology is

disfavored at $\gtrsim 2\sigma$. Future, more accurate measurements of the cross spectra will require comparison with a larger grid of simulated models.

- We consider the expected power of future observations to discriminate between different cosmological geometries. A sample of ~ 50 moderate resolution, FWHM ~ 150 km/s, close separation pairs (with $\Delta\theta \sim 30'' - 120''$) should be able to discriminate between an $\Omega_\Lambda = 0.7$ and an $\Omega_\Lambda = 0.8$ cosmology at the $\sim 2\sigma$ level, ignoring degeneracies with other IGM modeling parameters. We find that there is a sizeable advantage obtained by observing very close, $\Delta\theta \sim 30''$, separation pairs with high spectral resolution, provided simulation measurements are reliable at high k . Given ~ 10 high resolution, $\Delta\theta \sim 30''$ separation pairs, we should be able to distinguish between the two Lambda cosmologies at the 2σ level.

One should be able to obtain this type of sample with quasar pairs discovered by the Two Degree Field (2df) and SDSS surveys, provided one does some follow-up spectroscopy (Burles, private communication 2003). Two remarks may be helpful in this regard. First, due to the finite optical fiber size, SDSS selects against quasar pairs with separation less than $55''$. One can attempt to recover pairs with these separations by looking for objects with similar colors nearby existing quasars. Second, SDSS has a spectroscopic cut-off at 3800 \AA . One can recover many more pair spectra by going down to a lower cut-off of $\sim 3400 \text{ \AA}$. Since the auto spectrum has not yet been measured at the low redshifts corresponding to these wavelengths, one would also need to use the spectra in the sample to measure the auto spectrum at $z \sim 1.8$.

Finally, we mention a few words about future work. As the error bars on cross spectrum measurements get smaller in the future, it will be important to use higher resolution, larger volume simulations. It will also be important to test the accuracy of our N-body plus smoothing technique against full hydrodynamic simulations, especially if we aim to compare data and theory at high k where the hydrodynamic effects

should be most important. Measurements of the cross spectrum may also be useful in other pursuits such as recovering the linear mass power spectrum (Viel et al. 2002), reconstructing a three dimensional map of the density field in the IGM (Pichon et al. 2001), and constraining the effect of feedback on the IGM found by Adelbeger et al. (2003).

Appendix A

In this section we mention some details regarding the simulations that we run and show some convergence tests with respect to resolution and box size.

All of our simulations are run in an SCDM cosmology with the same linear transfer function. We use the Ma (1996) transfer function, which is a modified version of the BBKS transfer function (Bardeen et al. 1996). We assume a shape parameter of $\Gamma = \Omega_m h = 0.5$, and a normalization of $\sigma_8(z = 0) = 0.82$. We run all simulations assuming an $\Omega_m = 1$ cosmology so that the linear growth factor is just proportional to $1 + z$. In this case it is easy to use different simulation outputs to represent different power spectrum normalizations. The box units are converted into units of km/s assuming the EDS cosmology.¹⁷ Although this is a rather disfavored shape for the initial linear power spectrum, our purpose here is to span a range of power spectrum shapes and amplitudes near $z \sim 3$ *in units of km/s*, at scales around 1 h/Mpc, for which this initial power spectrum template is adequate. In a different cosmology the conversion between units of comoving *Mpc/h* and observed *km/s* units will require different initial linear power spectra to fit the observed flux auto spectra; however the differing initial power spectra must all lead to similar flux power spectra in units of *km/s* at $z \sim 3$. We do, however, then neglect the dependence of dynamics and redshift

¹⁷In converting the optical depth to redshift space we take $s_{\parallel} = H_{\text{box}}(z_{\text{sim}})x_{\parallel}/(1 + z_{\text{sim}}) + v_{\text{pec}}(x)$ and $s_{\perp} = H_{\text{box}}(z_{\text{sim}})x_{\perp}/(1 + z_{\text{sim}})$, where $v_{\text{pec}}(x)$ is the component of the peculiar velocity vector along the line of sight. In the event that we use a simulation output at z_{sim} to match the flux power spectrum at z_{obs} , the redshift space coordinates are rescaled by a factor $[H_{\text{box}}(z_{\text{obs}})/H_{\text{box}}(z_{\text{sim}})][(1 + z_{\text{sim}})/(1 + z_{\text{obs}})]$.

distortions on Ω_m . For flat models with a cosmological constant, we should only be making a small error since $\Omega_m(z \sim 3) \sim 1$. (For tests see Croft et al. 1998, Gnedin & Hamilton 2002). We examine a range of different power spectrum amplitudes and slopes. To investigate a range of power spectrum normalizations, we save the density and velocity fields from the simulations at a range of output times. Different power spectrum shapes are examined by considering a range of primordial spectral indices.

Simulations of the Ly α forest are challenging in that the requirements on box size and resolution are fairly stringent. On the smallest scales, one must resolve the pressure smoothing scale, which is typically $k_f \sim 35 \text{ h Mpc}^{-1}$ for an SCDM cosmology. One also needs to resolve the thermal broadening scale which smooths the optical depth on scales of $k_{\text{th}} \sim 0.1 \text{ s/km}$, for $T_0 = 10^4 \text{ K}$. On the largest scales one requires a boxsize large enough that fluctuations on the box scale are still in the linear regime, and such that the box has a sufficient volume to provide a representative sample of the universe. In figure (4.14) we show a test of the resolution of our simulation box. In this figure we show the flux auto and cross spectra from two simulations run in the same model, each with a box size of 20.0 Mpc/h , but one with 256^3 particles and the other with 512^3 particles.¹⁸ Right at the fundamental mode, probably due to the small number of modes available in the simulation box, the auto and cross spectra from the 512^3 simulation are substantially larger than those from the 256^3 simulation, otherwise the spectra from the low and high resolution simulations are consistent on large scales. In comparing the observed auto spectrum with simulation models we thus neglect scales with $k < 2 \times k_{\text{fun}}$, where k_{fun} is the fundamental mode of the simulation box. In comparing the cross spectrum with simulation models we include these modes, which should be adequate since the error bars on the cross spectrum are very large on such scales. On small scales the 256^3 simulation clearly misses small scale flux power in the auto spectrum, primarily at $k \gtrsim 0.03 \text{ s/km}$. Since we rely in this chapter on 256^3 simulations, we then only include data with $k \lesssim 0.03 \text{ s/km}$ in

¹⁸For the flux power spectrum, the relevant size for determining the resolution is that of the simulation box in units of km/s, rather than the size in co-moving Mpc/h. Our SCDM simulation should thus be roughly equivalent to a LCDM simulation with a box size of $20/\sqrt{3} \sim 37 \text{ Mpc/h}$.

comparing our models with observations, as mentioned in §4.3.1. The cross spectrum, at separation $\Delta\theta = 33''$, on the other hand, is actually slightly larger on small scales in the 256^3 simulation than in the 512^3 simulation. In this work, our data have poor resolution, (see Table 4.1 and the dotted lines in the figure), so we do not use the high k simulation points in comparing with data anyway. In figure (4.15) we show a box size test. The figure shows a comparison between cross and auto spectra measured in a 128^3 particle, 20.0 Mpc/h box size simulation and those measured in a 256^3 particle, 40.0 Mpc/h box size simulation. The two simulations thus have the same resolution, but one has twice the box size of the other. Additionally we show the auto and cross spectra in the smaller volume simulation using the same model, but averaged over 5 different realizations of the simulation box. On small scales the auto and cross spectra are quite similar. On large scales one can see the sample variance error from having only one realization of the smaller box. The figure also shows that this error is quite reduced by averaging over 5 different simulation realizations of the smaller volume box. In conclusion, it is less than ideal to obtain constraints from a single realization of a 256^3 , 20.0 Mpc/h simulation box. Especially as the error bars on the observed auto and cross spectra decrease, it will be necessary to simulate a larger volume at higher resolution.

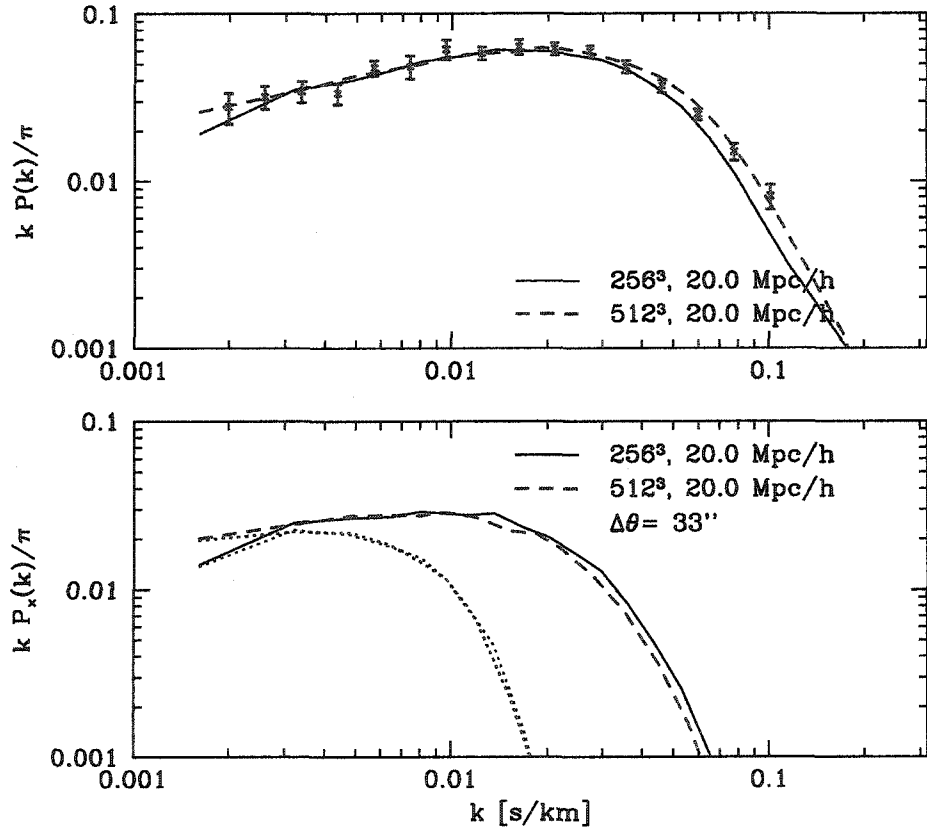


Figure 4.14 A resolution test, showing the flux auto and cross spectra for a 256^3 particle, $20.0 \text{ Mpc}/h$ boxsize simulation and those measured from a 512^3 particle, $20.0 \text{ Mpc}/h$ simulation in the same model. The assumed IGM model is $(a, n, k_f, T_0, \alpha, \langle f \rangle) = (0.19, 0.7, 35.0 \text{ h Mpc}^{-1}, 250 (\text{km/s})^2, 0.2, 0.684)$. The cross spectrum is computed assuming $\Omega_m = 0.3$. The comparison is shown for a single simulation realization at each resolution. The dotted curves show the cross spectra convolved with the instrumental resolution of the close separation pairs studied in §4.5.

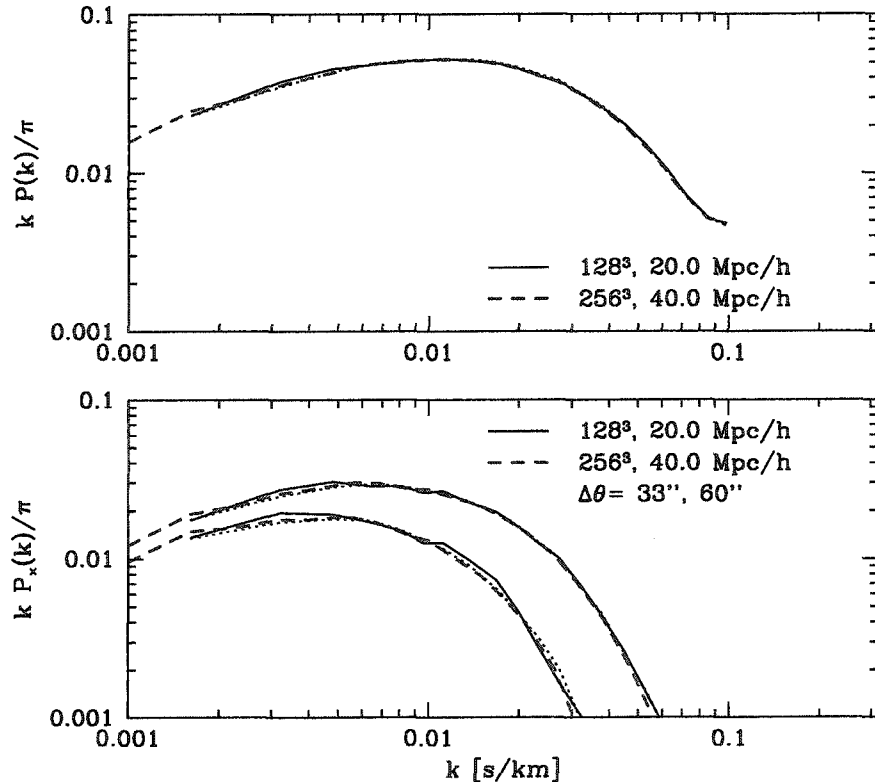


Figure 4.15 A boxsize test, showing the flux auto and cross spectra for a 128^3 particle, $20.0 \text{ Mpc}/h$ boxsize simulation and those measured from a 256^3 particle, $40.0 \text{ Mpc}/h$ simulation of the same model. The assumed IGM model is $(a, n, k_f, T_0, \alpha, \langle f \rangle) = (0.19, 0.7, 35.0 \text{ h Mpc}^{-1}, 250 (\text{km/s})^2, 0.2, 0.684)$. The cross spectrum is computed assuming $\Omega_m = 1.0$, and shown at separations of $\Delta\theta = 33''$ and $\Delta\theta = 60''$. The auto spectrum shown here comes from the average of 6,000 lines of sight taken along each of the simulation box axes. The cross spectra come from the average of 3,000 pairs of lines of sight along each of the simulation box axes. The dotted lines shows the result of averaging measurements of the auto and cross spectrum over 5 independent simulation realizations of the same model using the small volume simulations.

Conclusions

In this thesis, we presented cosmological constraints obtained by comparing Ly α forest absorption spectra with numerical simulations performed in the context of the gravitational stability model of the IGM. Here, we briefly recap some of our results in light of recent developments in the field, and mention future directions.

In the second chapter, we argued that spectroscopic observations of a $z = 6.28$ SDSS quasar imply a rapid evolution in the neutral hydrogen fraction near $z \sim 6$. This is suggestive of the end of the reionization epoch. How can this be accommodated with recent WMAP measurements of the temperature-polarization cross power spectrum (Kogut et al. 2003), which imply a large ionized fraction at $z \sim 15$? To be specific, the WMAP experiment finds a strong signal in the temperature-polarization cross power spectrum on large scales (multipole moments of $l \lesssim 10$) (Kogut et al. 2003). Such scales are much larger than the horizon size at decoupling: the implication is that a considerable amount of Thompson scattering must occur relatively recently, when the horizon size is much larger than at decoupling, in order to generate the large-scale polarization signal. In fact, the inferred optical depth to Thompson scattering is $\tau = 0.17 \pm 0.04$ (Kogut et al. 2003), where the error-bars are 1σ errors. Adopting a naive reionization model where the universe is completely neutral before some redshift, z_{reion} , while hydrogen is completely ionized (and helium completely doubly-ionized) thereafter, this measurement implies $z_{\text{reion}} = 15.3 \pm 2.7$ (from Hui & Haiman 2003, see also Spergel et al. 2003). For comparison, a similar model with $z_{\text{reion}} = 6$ produces a Thompson scattering optical depth of only $\tau = 0.04$, discrepant with the WMAP result at the 3σ level. Is there then a conflict between the WMAP results, and our

results based on the SDSS quasar?

Taken at face value, the two observations just imply that reionization does not occur in a single rapid step (see e.g., the review by Haiman 2003), but the WMAP results give us some pause and force us to re-examine the evidence for reionization activity at $z \lesssim 10$. Cautiously, we should keep in mind that our constraint on the evolution of the neutral fraction: 1) used only one $z \sim 6$ quasar, 2) the strongest constraint came from the Ly β trough,¹ 3) our simulations assumed a spatially homogeneous radiation field, neglecting radiative transfer effects, and 4) there are uncertainties related to estimating the quasar continuum in the Ly α forest. However, there is independent evidence for reionization activity at $z \lesssim 10$. One line of argument is based on measurements of the temperature in the IGM at $z \sim 3 - 4$ obtained from the Ly α forest. The argument is that if the IGM was reionized at high redshift, it would have subsequently cooled down too much to explain the temperature measurements at $z \sim 3 - 4$ (Theuns et al. 2002, Hui & Haiman 2003). Further evidence for reionization activity near $z \sim 6$ comes from the discovery of four additional SDSS quasars at $z \gtrsim 6$, each showing a Gunn-Peterson trough (White et al. 2003, Fan et al. 2004)². Finally, it has also been argued that one can infer the size of the HII region, or ‘proximity effect zone’, around the $z \sim 6$ quasars, and that the small size of such regions suggests a significantly neutral IGM at $z \sim 6$ (Wyithe & Loeb 2004, Mesinger & Haiman 2004).

Accepting both the WMAP measurement and our results from the SDSS quasar, as well as other evidence for reionization activity at $z \lesssim 10$, requires ionizing sources efficient enough to produce the high optical depth, while delaying the end of reionization (i.e., the epoch at which ionized regions ‘percolate’) until $z \sim 6$ (see e.g., Haiman & Holder 2003). One natural way of doing this is in ‘double reionization’

¹We believe that our modeling of the Ly β forest is accurate (see chapter 3), but it is not as extensively tested as that in the Ly α forest.

²One quasar spectrum, SDSS J1148+5251 at $z = 6.42$, shows a ‘transmission spike’ in the Ly α trough. Moreover there is a considerable amount of transmitted flux in the Ly β forest – the spectrum does *not* show a complete Ly β trough. White et al. (2003), however, argue that transmitted flux in the Ly β region of this spectrum is due to the presence of a ‘foreground’ $z = 4.9$ galaxy.

models where an early generation of metal-free, Pop III stars partially ionize the IGM at high redshift, turn off, and let ordinary Pop II stars finish off the ionization process near $z \sim 6$ (e.g. Cen 2003, Wyithe & Loeb 2003). Future observations and theoretical developments, however, will be necessary to detail reionization history and its implications for structure formation. While future Gunn-Peterson trough measurements from high redshift quasars will help solidify our knowledge at $z \sim 6$, an alternate probe will be necessary to discern the evolution of the neutral fraction at higher redshifts and to detail the topology of reionization. Some possible probes are 21 cm emission from neutral hydrogen (see e.g., Zaldarriaga, Furlanetto, & Hernquist 2004), the profiles of Ly α emission lines around high redshift quasars, galaxies or the absorption profile near a gamma ray burst afterglow (see e.g., Miralda-Escudé 1998, Barkana & Loeb 2004, Mesinger, Haiman, & Cen 2004), metal absorption lines (Oh 2002), future CMB polarization measurements (Kaplinghat et al. 2003, Holder et al. 2003), and future kinetic SZ surveys (Zhang, Pen, & Trac 2004), among others. Theoretical progress should advance in conjunction with the development of increasingly sophisticated radiative transfer simulations (Gnedin 2000, Gnedin & Abel 2001, Sokasian et al. 2001, Razoumov et al. 2002).

In the third chapter, we discussed the utility of extending Ly α forest analyses to include the Ly β region in quasar spectra. We detailed how Ly β absorption may provide a better probe of the slope of the temperature- density relation than Ly α absorption. Here we emphasize that this may be useful in constraining the reionization history of HI and HeII, and mention briefly the status of HeII reionization studies. There is some evidence that HeII may be reionized near $z \sim 3$, including an apparent increase in the temperature of the IGM near this redshift (Schaye et al. 2000), the evolution of the mean transmission in the HeII Ly α forest (see e.g. Zheng et al. 2004), and the possible presence of a feature in the evolution of the mean transmission in the HI Ly α forest (Bernardi et al. 2003, Theuns et al. 2003). However, this is still controversial: some constraints on the temperature of the IGM are consistent with no evolution (McDonald et al. 2001, Zaldarriaga, Hui, & Tegmark 2001), and the feature

in the evolution of the mean transmission in the HI Ly α forest is debated (McDonald, P., private communication, 2003). A more accurate measurement of the slope of the temperature-density relation near $z \sim 3$ could be helpful in this regard; the IGM is expected to be close to isothermal near the epoch of HeII reionization, and the slope of the temperature-density is expected to increase thereafter (Hui & Gnedin 1997, Schaye et al. 2000).

In the fourth chapter we discussed constraining dark energy using the cross-correlation between the absorption in the spectra of close quasar pairs. At least two groups are presently collecting larger samples of close quasar pairs (Tytler, Crotts, et al. 2004, and Burles et al. 2004), which will likely afford a stronger constraint on dark energy. Additionally, these measurements will provide an important consistency check on the gravitational instability model of the Ly α forest.

Another topic in which the Ly α forest may play an important role is in determining the linear matter power spectrum on small scales. This is particularly exciting given forthcoming measurements of the flux power spectrum from ~ 3000 SDSS Ly α forest spectra. This sample is ~ 60 times larger than previous data sets, and thereby represents a great increase in statistical precision (McDonald et al. 2004, Hui et al., in prep). Current measurements of the Ly α forest flux power spectrum imply constraints on the linear matter power spectrum at $z \sim 3$ and scales of $k \sim 0.1 - 5h \text{ Mpc}^{-1}$ (see e.g., Croft et al. 1998, McDonald et al. 2000, Croft et al. 2002, Zaldarriaga, Hui, & Tegmark 2001, Zaldarriaga, Scoccimarro, & Hui 2003). This is a particularly valuable probe since one can infer the *linear* power spectrum of density fluctuations on scales smaller than examined by current CMB experiments and galaxy surveys (Croft et al. 1998). The measurements of the Ly α forest flux power spectrum thus provide an important complement to other probes of large scale structure, when constraints on small scale clustering from the Ly α forest are combined with constraints on large scales from CMB experiments. The leverage from the large range of scales probed allows for constraints on neutrino mass (Croft, Hu & Davé 1999) and the possibility that the primordial power spectrum is not a pure power law (Spergel et al. 2003,

Seljak, McDonald, & Makarov 2003).

For the Ly α forest to be a valuable probe of the linear matter power spectrum, however, a range of sources of systematic error need to be addressed in more detail. One such source of error is that previous analyses relied on estimating the unabsorbed quasar continuum level, i.e., how much flux from the quasar there is in the absence of absorption from the Ly α forest. In particular, measurements of the mean transmitted flux through the Ly α forest were used to calibrate the amplitude of the photo-ionizing background, a crucial input parameter in the theoretical modeling of the Ly α forest.³ This amplitude can only be constrained from observations in an indirect manner, and it is not feasible to predict this quantity from first principles with anywhere close to the required accuracy. Furthermore, constraints on the linear matter power spectrum are very sensitive to the assumed mean transmitted flux (Croft et al. (2002), Zaldarriaga et al. (2001a), Zaldarriaga et al. (2003), Seljak, McDonald, & Makarov 2003). It is therefore desirable to have an alternative way of calibrating the amplitude of the photo-ionizing background that does not depend on fitting the quasar continuum. One possible calibrator is the one-point probability distribution (pdf) of the fluctuations in the flux about the mean, relative to the mean, i.e. the pdf of $\delta_f = (f - \langle f \rangle)/\langle f \rangle$ (Lidz et al., in prep.). This statistic, while sensitive to the amplitude of the ionizing background, has the virtue that its measurement does not require an estimate of the unabsorbed continuum level.⁴

It is also important to continually check the accuracy of the gravitational instability model of the Ly α forest, particularly as the statistical precision of measurements increases. Non-gravitational effects like shocks, galactic outflows, fluctuations in the

³This is, of course, the way we constrained the amplitude of the ionizing background at high z . Here we emphasize the sensitivity of constraints on the matter power spectrum to the measured mean transmitted flux.

⁴To determine this quantity observationally, one can directly measure the mean flux, $\langle f \rangle$ (Hui et al. 2001, Croft et al. 2002), without first rescaling to the unabsorbed continuum level. This statistic is sensitive to the *shape* of the continuum, since the continuum varies slowly across a quasar spectrum, but it is not sensitive to the *normalization* of the quasar continuum.

ionizing background, temperature fluctuations, and others may impact the statistics of the forest at some level. These effects, interesting in their own right, might also taint the determination of cosmological parameters from the forest. In fact, while there is good agreement between the simple, gravitational instability model of the Ly α forest and present data, there is also a great deal of observational evidence that suggests that feedback must impact the IGM at some level (for some examples, see e.g. Adelberger et al. 2003). One recent and interesting line of evidence comes from observations of Ly α absorption, seen in the spectra of background quasars, nearby foreground Lyman break galaxies (Adelberger et al. 2003). These spectra seem to show reduced absorption within $\sim 0.5h^{-1}$ Mpc of the galaxies. While the evidence is not statistically strong, it might indicate the impact of feedback on the IGM, and its effect on the Ly α forest.⁵ Clearly it is important to understand these feedback effects in more detail, and to develop ways of discerning their influence on the structure in the Ly α forest. One diagnostic for non-gravitational effects involves moving beyond the flux power spectrum, and looking at higher-order moments of the flux distribution in the Ly α forest (Zaldarriaga, Seljak & Hui 2001). Gravitational instability theory makes definite predictions for the relation between the density two-point correlation function and higher order density correlation functions. This scaling should imprint itself on the statistics of the Ly α forest if the structure in the forest is dominated by gravitational instability. Any departure in the relation between the two-point and higher order flux statistics might be the signature of non-gravitational processes (Zaldarriaga, Seljak, & Hui 2001, Fang & White 2004). We expect the measurement of higher order statistics, e.g., the bispectrum (Mandelbaum et al. 2003, Viel et al. 2003), and the insight these measurements provide concerning the influence of galactic feedback on the Ly α forest, to be an active area of research in the near future.

In conclusion, we expect the study of the Ly α forest to continue to impact our un-

⁵Several groups have tried to reproduce this result by incorporating simplified wind models, or an enhanced photoionizing background near the foreground galaxies, into simulations (Croft et al. 2002, Kollmeier et al. 2003, Maselli et al. 2004). They generally find it difficult to reproduce the observations, unless very extreme properties are assumed for the galactic outflows.

derstanding of cosmology in upcoming years. The measurement of cosmic microwave background anisotropies, notably recent precision measurements from the WMAP satellite, have helped to solidify our understanding of structure formation at early times and on large scales. On the relevant scales, density fluctuations are weak, and the corresponding physics is *linear*. An important ambition for future cosmological research is to push observations and theoretical understanding to progressively smaller scales, where the relevant physics is inevitably *non-linear* and complicated. In this respect, the study of the Ly α forest occupies an intermediate ground between the relatively simple, linear physics that describes the large scale CMB anisotropies and the complicated, nonlinear physics that operates on small scales. While challenging to extract, the resulting insights the Ly α forest provides on small-scale clustering, dark energy, and the physics of the IGM, are rewarding.

Bibliography

- Adelberger, K. L. A., Steidel, C. C., Shapley, A. E., & Pettini, M. 2003, ApJ, 584, 45
- Alcock, C. & Paczynski. B. 1979, Nature, 281, 358
- Anderson, S. F. et al. 2001, AJ, 122, 503
- Ballinger, W. E., Peacock, J. A., & Heavens, A. F. 1997, MNRAS, 282, 877
- Bajtlik, S., Duncan, R. C., & Ostriker, J. P. 1988, ApJ, 327, 570
- Bardeen, J. M., Bond, J. R., Kaiser, N., & Szalay, A. S. 1986, ApJ, 304, 15
- Barkana, R. 2002, NewA, 7, 337
- Barkana, R., & Loeb, A. 2004, ApJ, 601, 64
- Bechtold, J., Crotts, A. P. S., Duncan, R. C., & Fang, Y. 1994, ApJ, 437, L83
- Becker, R. H., Fan, X., White, R. L., Strauss, M. A., Narayanan, V. K., Lupton, R. H., Gunn, J. E. et al. 2001, AJ, 122, 2850
- Bernardi, M. et al. 2003, AJ, 32
- Bi, H., Borner, G., Chu. Y. 1992, A & A, 266, 1
- Bi, H. & Davidsen, A. F., 1997, *ApJ* 479, 523
- Bond, J. R. & Wadsley, J. W., 1997, *Proc. 12th Kingston Conf., Halifax*, (astro-ph 9703125)
- Bryan, G., Machacek, M., Anninos, P., & Norman, M. L. 1999, ApJ, 517, 13
- Bryan, G., & Machacek, M. 2000, ApJ, 534, 57
- Burles, S., Nollett, K. M., & Turner, M. S. 2001, ApJ, 552L
- Cen, R., Miralda-Escudé, J., Ostriker, J. P., Rauch, M. 1994, ApJ, 437, L9
- Cen, R. & McDonald, P. 2002, ApJ, 570, 457
- Cen, R. 2003, ApJ, 591, 12

- Choudhury, T. R., Srianand, R. & Padmanabhan, T. 2001, ApJ, 559, 29
- Cole, S., Fisher, K. B., & Weinberg, D. 1994, MNRAS, 267, 785
- Couchamn, H. M. P., Thomas, P. A., Pearce, F. P., 1995, ApJ, 452, 797
- Croft, R. A. C., Weinberg, D. H., Katz, N., & Hernquist, L., 1998a, *ApJ* **495**, 44
- Croft, R. A. C., Weinberg, D. H., Pettini, M., Hernquist, L., & Katz, N. 1999, ApJ, 520, 1
- Croft, R. A. C., Weinberg, D. H., Bolte, M., Burles, S., Hernquist, L., Katz, N., Kirkman, D., & Tytler, D. 2002, ApJ, 581, 20
- Croft, R. A. C., Hernquist, L., Springel, V., Westover, M., & White, M. 2002, ApJ, 580, 634
- Crotts, A. P. S., & Fang, Y. 1998, ApJ, 502, 16
- Dijkstra, M., Lidz, A., & Hui, L. 2004, ApJ 605, 7.
- Djorgovski, S. G., Castro. S. M., Stern, D. & Mahabal, A. 2001, ApJL, 560, 5
- Fan, X., et al. 2000, AJ, 120, 1167
- Fan, X., et al. 2001a, AJ, 122, 2833
- Fan, X., Narayanan, V. K., Strauss, M. A., White, R. L., Becker, R. H., Pentericci, L., & Rix, H.-W. 2002, AP, 123, 1247
- Fan, X. et al. 2004, AJ, in press, astro-ph/0405138
- Fang, T., & White, M. 2004, ApJL, 606, 9
- Fry, J. N. 1994, PRL, 73, 215
- Gaztanaga, E., & Croft, R. A. C. 1999, MNRAS, 309, 885
- Gnedin, N. Y, & Hui, L. 1998, MNRAS, 296, 44
- Gnedin, N. Y 2000, ApJ, 542, 535
- Gnedin, N. Y 2001, submitted to MNRAS (astr-ph 0110290)
- Gnedin, N. Y, & Abel, T. 2001, NewA, 6, 438
- Gnedin, N. Y, & Hamilton, A. J. S., 2002, MNRAS, 334, 107
- Gunn, J. E., & Peterson, B. A. 1965, ApJ, 142, 1633
- Haehnelt, M. G., Madau. P., Kudritzki, R. P., Haardt, F., 2001, ApJL, 549, 151
- Haiman, Z., & Holder, G. P. 2003, ApJ, 595, 1

- Haiman, Z. 2003, to appear in Carnegie Observatories Astrophysics Serier, Vol. 1: Coevolution of Black Holes and Galaxies, ed. L. C. Ho (Cambridge: Cambridge Univ. Press); astro-ph/0304131
- Hamilton, A. J. S., & Tegmark, M. 2002, MNRAS, 330, 506
- Hatton, S., & Cole, S. 1998, ApJ, 296, 10
- Hernquist, L., Katz, N., Weinberg, D. H., & Miralda-Escudé, J., 1996, *ApJ* 457, L51
- Holder, G. P., Haiman, Z., Kaplinghat, M., & Knox, L. 2003, ApJ, 595, 13
- Hoyle, F., Outram, P. J., Shanks, T., Boyle, B. J., Croom, S. M., Smith, R. J. 2002, MNRAS, 332, 311
- Hui, L., Gnedin, N. Y., & Zhang, Y., 1997, *ApJ* 486, 599
- Hui, L. & Gnedin, N. Y., 1997, *MNRAS* 292, 27
- Hui, L., Stebbins, A., & Burles, S. 1999, ApJ, 511, L5
- Hui, L. 1999, ApJ, 516, 519
- Hui, L., Burles, S., Seljak, U., Rutledge, R. E., Magnier, E., & Tytler, D. 2001, ApJ, 552, 15
- Hui, L., & Haiman, Z. 2003, ApJ, 596, 9
- Kaiser, N. 1987, MNRAS, 227, 1
- Kaiser, N. & Peacock, J. A. 1991, ApJ, 379, 482
- Kaplinghat, M. et al. 2003, ApJ, 583, 24
- Kendall, M. G., & Stuart, A. 1958, The Advanced Theory of Statistics, v. 1, (New York: Hafner)
- Kim, T.-S., Carswell, R. F., Cristiani, S., D'Odorico, S., & Giallongo, E. 2002, MNRAS, 335, 555
- Kim, T.-S., Hu, E. M., Cowie, L. L., & Songaila, A. 1997, AJ, 114, 1
- Kirkman, D., & Tytler, D. 1997, ApJ, 484, 672
- Kogut, A., et al. 2003, ApJS, 148, 175
- Kollmeier, J. A., Weinberg, D. H., Davé, R., & Katz, N. 2003, ApJ, 594, 75
- Kujat, J., Linn, A. M., Scherrer, R. J., & Weinberg, D. H. 2002, ApJ, 572, 1
- Lidz, A., Hui, L., Zaldarriaga, M., & Scoccimarro, R. 2002, ApJ, 579, 491

- Lidz, A., Hui, L., Crots, A., & Zaldarriaga, M. 2003, ApJ submitted, astro-ph/0309204
- Lin, W. & Norman, M. L., 2002, (astro-ph 0211177)
- Ma, C.-P., 1996, ApJ, 471, 13
- Mandelbaum, R., McDonald, P., Seljak, U., & Cen, R. 2003, MNRAS, 344, 776
- Maselli, A. et al. 2004, MNRAS, 350L, 21
- Matsubara, T. & Suto, Y. 1996, ApJ, 470, L1
- Matsubara, T. & Szalay, A. 2002, PRL, submitted (astro-ph 0208087)
- McDonald, P. & Miralda-Escudé, J. 1999, ApJ, 519, 486
- McDonald, P., Miralda-Escudé, J., Rauch, M., Sargent, W. L. W., Barlow, T. A., Cen, R., & Ostriker, J. P., 2000a, ApJ, 543, 1
- McDonald, P., Miralda-Escudé, J., Rauch, M., Sargent, W. L. W., Barlow, T. A., & Cen, R. 2001, ApJ, 562, 52
- McDonald, P. & Miralda-Escudé, J., 2001, ApJ, 549, L11
- McDonald, P. 2003, ApJ, 585, 34
- McDonald, P. et al. 2004, ApJ, submitted, astro-ph/0405013
- Meiksin, A., Bryan, G. & Machacek, M. 2001, MNRAS, 327, 296
- Meiksin, A. & White, M., 2001, MNRAS, 2001, 324, 141
- Meiksin, A., & White, M., 2004, MNRAS, 350, 1107
- Mesinger, A., Haiman, Z., & Cen, R., 2004, ApJ, submitted, astro-ph/0401130
- Mesinger, A., & Haiman, Z. 2004, ApJL, submitted, astro-ph/0406188
- Miralda-Escude, J., & Rees, M. J. 1994, MNRAS, 266, 343
- Miralda-Escudé, J., Cen, R., Ostriker, J. P., Rauch, M., 1996, ApJ, 471, 582
- Miralda-Escudé, J., 1998, ApJ, 501, 15
- Muecket, J. P., Petitjean, P., Kates, R. E., & Riediger, R., 1996, A&A 308, 17
- Netterfield, C. B., et al. 2002, ApJ, 571, 604
- Nusser, A., Haehnelt, M. 1999, MNRAS, 303, 179
- Nusser, A., & Haehnelt, M. 2000, MNRAS, 313, 364
- Oh, S. P. 2002, MNRAS, 336, 1021

- Outram, P. J., Hoyle, F., Shanks, T., Boyle, B. J., Croom, S. M., Loaring, N. S., Miller, L., & Smith, R. J., 2001, MNRAS, 328, 1740
- Perlmutter, et al. 1999, ApJ, 517, 565
- Phillips, S. 1994, MNRAS, 269, 1077
- Pichon, C., Vergely, J. L., Rollinde, E., Colombi, S., & Petitjean, P. 2001, MNRAS, 326, 597
- Popowski, P. A., Weinberg, D. H., Ryden, B. S., & Osmer, P. S. 1998, ApJ, 498, 11
- Press, W. H., Rybicki, G. B., & Schneider, D. P. 1993, ApJ, 414, 64
- Pryke, C., et al. 2002, ApJ, 568, 46
- Rauch, M. et al. 1997, ApJ, 489, 7
- Rauch, M., Sargent, W. L., Barlow, T. A., Carswell, R. F. 2001, ApJ, 562, 76
- Razoumov, A. O., Norman, M. L., Abel, T., & Scott, D. 2002, ApJ, 572, 695
- Reisenegger, A. & Miralda-Escudé, J., 1995, *ApJ* 449, 476
- Ricotti, M., Gnedin, N. Y., Shull, J. M., 2000, ApJ, 534, 41
- Riess, A. et al. 1998, AJ, 116, 1009
- Rollinde, E., Petitjean, P., Pichon, C., Colombi, S., Aracil, B., D'Odorico, V., & Haehnelt, M. G., 2003, MNRAS, 341, 1279
- Ryden, B. S. 1995, ApJ, 452, 25
- Ryden, B. S., & Melott, A. L., 1996, ApJ, 470, 160
- Schaye, J., Theuns, T., Leonard, A., & Efstathiou, G. 1999, MNRAS, 310, 57
- Schaye J., Theuns, T., Rauch, M., Efstathiou, G., Sargent, W. L. W., MNRAS, 318, 817
- Scherrer, R. J., & Weinberg, D. H., 1998, ApJ, 504, 67
- Schneider, D. P. et al. 2001, AJ, 121, 1232
- Scoccimarro, R., Couchman, H. M. P., & Frieman, J. A., 1999, ApJ, 517, 531
- Scoccimarro, R., Feldman, H. A., Fry, J. N., Frieman, J. A. 2001, ApJ, 546, 652
- Scoccimarro, R. & Sheth, R. 2002, MNRAS, 329, 629
- Seljak, U., McDonald, P., & Makarov, A. 2003, MNRAS, 342L, 79
- Seo, H.-J., Eisenstein, D. J. 2003, ApJ, 598, 720

- Simcoe, R. A., Sargent, W. L. W., Rauch, M. 2002, ApJ, 578, 737
- Sokasian, A., Abel, T., & Hernquist, L. 2001, NewA, 6, 359
- Songaila, A., Hu, E. M., Cowie, L. L., & McMahon, R. G. 1999, ApJ, 525, L5
- Spergel, D. et al. 2003, ApJS, 148, 175
- Tegmark, M. & Zaldarriaga, M. 2000, ApJ, 544, 30
- Theuns, T., Leonard, A., Schaye, J., & Efstathiou, G. 1999, MNRAS, 303L, 58
- Theuns, T., Schaye, J., Zaroubi, S., Kim, T. S., Tzanavaris, P., Carswell, B. 2002, ApJL, 567, 103
- Theuns, T. et al. 2002, ApJ, 574, L111
- Verde, L. et al. 2002, MNRAS, 335, 432
- Viel, M., Matarrese, S., Mo, H. J., Haehnelt, M. G., Theuns, T., 2002, MNRAS 329, 848
- Viel, M., Matarrese, S., Heavens, A., Haehnelt, M. G., Kim, T. S., Springel, V., & Hernquist, L. 2004, MNRAS, 347L, 26
- Weinberg, D. H., Miralda-Escude, J., Hernquist, L., & Katz, N. 1997, ApJ, 490, 564
- White, M. & Croft, R. A. C. 2000, ApJ, 539, 497
- White, R. L., Becker, R. H., Fan, X., & Strauss, M. A. 2003, AJ, 126, 1
- Wyithe, J. B., & Loeb, A. 2004, Nature, 427, 815
- Wyithe, J. B., & Loeb, A. 2003, ApJ, 586, 693
- Zaldarriaga, M., Hui, L., & Tegmark, M., 2001a, ApJ, 557, 519
- Zaldarriaga, M., Seljak, U., & Hui, L., 2001b, ApJ, 551, 48
- Zaldarriaga, M., 2002, ApJ, 564, 153
- Zaldarriaga, M., Scoccimarro, R., & Hui, L., 2003, ApJ, 590, 1
- Zaldarriaga, M., Furlanetto, S., & Hernquist, L., 2004, ApJ, submitted, astro-ph/0311514
- Zehavi, I. et al. 2003, submitted to ApJ, astro-ph 0301280
- Zhang, Y., Anninos, P., & Norman, M. L., 1995, ApJL, 453, L57
- Zhang, P., Pen, U., & Trac, H., 2004, MNRAS, 347, 1224
- Zheng, W. et al. 2004, ApJ, 605, 631